INVESTIGATION ON DUCTILE FRACTURE OF STRUCTURAL STEELS AND WELDS: NUMERICAL ANALYSIS AND EXPERIMENTAL ASSESSMENT

By

S. ATHIMOOLAKRISHNAN

Enrolment No: ENGG02201504008

Indira Gandhi Centre for Atomic Research

Kalpakkam - 603102, India

A thesis submitted to the

Board of Studies in Engineering Sciences

In partial fulfillment of requirements

for the Degree of

DOCTOR OF PHILOSOPHY

of

HOMI BHABHA NATIONAL INSTITUTE

October, 2019

Homi Bhabha National Institute

Recommendations of the Viva Voce Committee

As members of the Viva Voce Committee, we certify that we have read the dissertation prepared by **S. Athimoolakrishnan** entitled "**Investigation on Ductile Fracture of Structural Steels and Welds: Numerical Analysis and Experimental Assessment**" and recommend that it may be accepted as fulfilling the thesis requirement for the award of Degree of Doctor of Philosophy.

	Signature with date
Chairman - **Dr. K. Velusamy**	18/12/2020
Guide / Convener- **Dr. G. Sasikala**	18.12.2020
Co-guide - **Dr. C. Lakshmana Rao**	C. Lakshmana Rao
Examiner - **Dr. Kalyan Kumar Ray**	18.12.2020
Member 1- **Dr. B.P.C. Rao**	18/12/2020
Member 2- **Dr. V. S. Srinivasan**	V.S. Srinivasan 18/12/2020
Member 3- **Dr. A. Jasmin Sudha**	A. Jasmin Sudha 18/12/2020

Final approval and acceptance of this thesis is contingent upon the candidate's submission of the final copies of the thesis to HBNI.

We hereby certify that we have read this thesis prepared under our direction and recommend that it may be accepted as fulfilling the thesis requirement.

Date: 18-12-2020

Place: IGCAR-Kalpakkam

C. Lakshmana Rao

Co-guide

Guide

INVESTIGATION ON DUCTILE FRACTURE OF STRUCTURAL STEELS AND WELDS: NUMERICAL ANALYSIS AND EXPERIMENTAL ASSESSMENT

By

S. ATHIMOOLAKRISHNAN

Enrolment No: ENGG02201504008

Indira Gandhi Centre for Atomic Research

Kalpakkam - 603102, India

A thesis submitted to the

Board of Studies in Engineering Sciences

In partial fulfillment of requirements

for the Degree of

DOCTOR OF PHILOSOPHY

of

HOMI BHABHA NATIONAL INSTITUTE

October, 2019

CONTENTS

LIST OF FIGURES

LIST OF TABLES

Chapter 7: An Overview of the Contribution and Future Directions

7.1 General Outcome of the Research Work

The main research objectives of the present investigation as outlined in Chapter-1 have been met. The work towards prediction of fracture in 316LN SS and P91 base materials, 316LN SS weld and dissimilar metal weld joint between 316LN SS and P91 using a combination of experimental data, numerical methods and analytical procedure have been completed. The experimentally validated material fracture parameters and FEM predictive procedures developed in the present investigation have been demonstrated for fracture predictions under intermediate stress triaxiality in P91 steel and in small diameter 316LN SS straight pipes. An overview of the investigations on base material and welds are as follows:

7.2 An Overview of Fracture Studies on 316LN SS and Fracture Prediction

The investigation was to establish crack initiation and growth parameters for low strength, high hardening and high toughness 316LN stainless steel.

- Large deformation elastic-plastic FEM simulations along with experimental stretch zone width measurements are used to establish crack initiation parameters.
- The proposed local damage approach based on uniform strain and grain diameter is able to predict the crack initiation parameters viz., SZW_i, J_i and $CTOD_i$ under monotonic loading condition.
- The damage parameter and saturated *far field* J-integral for a growing crack have been evaluated and calibrated with experimental results.

- A close agreement between predicted load-displacement results with the experimental results implies that the damage initiation and evolution parameters established in the present study is validated for crack growth simulations in 316LN SS.

7.3 An Overview of Fracture Studies on P91 Steel and Fracture Prediction

The investigation was to evaluate the damage parameter for prediction of crack initiation in high strength and less hardening P91 steel under an intermediate range of stress triaxiality, which is the stress state usually experienced by the tubes of steam generators.

- The mechanism leading to ductile fracture in P91 steel is due to void formation at second phase particles due to cracking /de-bonding of these particles from the parent matrix under tensile stresses. The continuum parameters, plastic strain and hydrostatic stress were responsible for voids to grow and eventually coalesce. The Rice-Tracy model has been calibrated to represent the void coalescence process in P91 steel.
- The Rice-Tracy damage parameter evaluated from coupled experimental-numerical analysis for crack initiation in P91 steel was able to predict the crack initiation load for a range of stress triaxiality conditions.

7.4 An Overview of Fracture Studies on 316LN SS Weld and Fracture Prediction

The fracture behavior of 316LN SS weld considering weld interfaces perpendicular to a propagating crack in CT geometry have been studied based on coupled experimental data and FEM simulations.

- The experimental *J*-R curves with the initial crack tip in weld metal, near to interface and in base material have been evaluated. A modified elastic component, J_{el} based on instantaneous equivalent Young's modulus has been introduced to evaluate *J*-R curve.
- The elastic-plastic FE analysis has been carried out for CT specimens with various stationary crack lengths lying perpendicular to the weldment. The *J*-integral incorporating the interface effect has been compared with material *J*-R curve.
- The influence of elastic inhomogeneity on a propagating crack in 316LN SS weldment has been accounted through a proposed equivalent Young's modulus approach.
- The experimental *J*-R curves estimated as per the ASTM E1820 procedure are in agreement with the proposed *modified J*-integral values obtained from numerical simulations.

7.5 An Overview of Fracture Studies on DMW Joint (316LN SS-P91)

The tensile deformation, notch deformation and fracture behavior characterization for P91-HAZ, IN 182 butter layer and IN182 weld have been completed. There is a similarity in behavior trend among notch strength from notch tensile specimen and *J*-R curve from CT specimen. However, the fracture morphology and von-Mises stress fields obtained from FE analysis on CT specimen with stationary crack have shown that the crack front deviates from the principal crack plane due to adjacent material strength mismatch and interfaces. This is one of the potential issues to which the *modified J*-

integral approach demonstrated for a propagating crack across the weld interface could be adopted, and this is proposed as future work.

7.6 An Overview of Fracture Prediction for 316LN SS Straight Pipes

The predictive ability of fracture parameters validated at specimen level (CT) has been demonstrated for fracture prediction in 316LN SS straight pipe with circumferential through wall crack.

- The experimental *J*-R curve for 316LN SS base and weld pipes with through-wall crack has been established.
- The comparison of *J*-R curves between pipe and pipe welds with CT specimens indicate that the CT specimen data is insufficient for fracture assessment of the components.
- The X-FEM crack growth simulations results are in close agreement with the experimental result of base pipes.
- The limit load analyses reveal that the crack initiation and propagation are observed prior to attaining the maximum bending moment. The effect of initial crack angle on *J*-R curve is negligible in the case of weld pipe, especially in the initial regime of crack growth and the crack deviates into interface/base material region.

7.7 Future Directions

Based on the understanding developed in the present work, it is envisaged that there is a good scope for further investigations related to prediction of fracture in austenitic stainless steels and ferritic steels and its welds using large deformation elastic-plastic FEM analysis. The followings are suggested for further perusal.

- The applicability of the proposed local damage approach for 316LN SS and the FEM procedure has been found to bear potential, however, should be validated for different stainless steel materials with varying grain sizes. The estimated material damage parameters for 316LN SS can be used to carry out the fracture assessment of various components.
- The prediction of fracture in P91 steel components using the proposed damage index will further demonstrate the strength of the procedure and applicability of the damage parameters for real life component. The methodology evolved in the present study to evaluate the mesh size independent damage index for Mod. 9Cr-1Mo steel (P91) may be extended to other ferritic steels.
- The equivalent Young's modulus established for CT geometry may be extended to other geometries for which closed form linear elastic solutions are available for determining the elastic component of energy release rate.
- The *modified* *J*-integral approach proposed in the present study could be extendable to other geometries and a propagating crack approaching an inclined interface.
- The fracture morphology and preliminary finite element analysis on DMW joint (for CT specimen) studied in the thesis shows that the crack path deviates from normal crack plane to other regions of the weldment, hence by evaluating the *modified* *J*-integral for various stationery crack depths along the experimental crack plane will provide an appropriate *J*-R curve for DMW joint. Similarly for weld pipe, the crack path deviates into interface regions;

hence adopting *modified* J-integral approach could help to estimate crack initiation J-integral value for integrity assessment.

SUMMARY

The major challenge in fracture analysis is to predict fracture in structural components using material fracture data generated from standard test specimens. Austenitic stainless steel and ferritic steels and their welds are the major structural materials in nuclear and thermal power plants. In the present study, the fracture behavior of 316LN stainless steel and its weld, Modified 9Cr-1Mo ferritic steel (P91) and dissimilar metal weld joint between these have been studied. The ductile fracture prediction for a wide range of stress triaxiality has been carried out based on experimentally validated damage/fracture parameters. These parameters are estimated using combination of experimental data, damage mechanics approaches and FEM simulations. A linear damage model based on critical strain at a characteristic distance and damage potential in terms of continuum parameters have been established for crack initiation and growth analysis in 316LN SS. For a propagating crack across the interfaces of 316LN SS weld, a modification to elastic component of *J* based on equivalent Young's modulus in *J*-R curve evaluation procedure has been proposed. Further, a *modified* *J*-integral which accounts for weld interface effect has been introduced in *J*-integral determination using FEM. A mesh size independent Rice-Tracey model's damage parameter has been assessed for P91 steel. The predictive ability of damage/fracture parameter has been demonstrated for intermediate range of stress triaxiality. Similarly for 316LN SS, the specimen level validated fracture parameters are used to predict crack growth in small diameter straight pipes with initial circumferential through-wall crack. A close agreement between predicted and experimental data validates the damage/fracture parameters and methodologies developed in the present investigation for fracture analysis of structural components.

Chapter 1: Introduction

1.1 Background and Motivation

Austenitic stainless steels, such as AISI type 304L, 316L, 316LN etc., and chromium-molybdenum ferritic steels, such as 2.25Cr-1Mo, 9Cr-1Mo and Modified 9Cr-1Mo (popularly known as P91) steels are the major structural and piping materials used in thermal and nuclear power plants. Similar and dissimilar metal joints between these steels are employed in piping components and steam generators. Among these steels, AISI type 316LN SS and P91 steels are used as major structural and piping material for liquid sodium cooled Prototype Fast Breeder Reactor (PFBR) being commissioned at Kalpakkam. Welding is the major metal joining process employed for piping and reactor components of PFBR. Transition weld joints between 316LN SS and P91 steels are made with Nickel base alloy as an intermediate piece to minimize the steep gradient in the coefficient of thermal expansion. The weld joints are likely to contain flaws before being put into service. The weld experiences large plastic strain in each weld pass and temperature gradient in the solidified weld metal, and the adjacent base metal leading to the formation of heat affected zone [1]. The microstructural variation and various weld zone interfaces across the weld and base metal induce a complex stress state under structural loadings. For integrity assessment of components and design of components against ductile fracture, the fracture mechanics data of each zone of the weld and base materials are an essential input. The important challenge in transferring fracture mechanics data to industrial components is due to complex situations like heterogeneous materials and different states of stress triaxiality. Further, the fracture analysis becomes more complex for high ductility and high toughness materials due to geometric effects. These geometry effects on cracked specimens are observed for numerous materials for which the single parameter approach is not sufficient to characterize the fracture behavior. To overcome these difficulties, local approaches provide an alternative methodology to global approach for fracture analysis of a material in which microstructure damage mechanics are taken into account.

1.2 Some Pertinent Background

The predictive methods for fracture are important for integrity assessment of large size components operating in industries because it is impractical or cost-ineffective to carry out full-scale fracture experiments. Over the years, the mathematical framework for the description of localized phenomena of void nucleation, growth and coalescence leading to ductile fracture, i.e., continuum damage mechanics concepts have been used to predict fracture along with classical fracture mechanics concepts. Finite element methods (FEM) and Extended-finite element methods (X-FEM) simulations with appropriate damage criteria, i.e., crack initiation/growth criterion is able to predict the stress state, crack path, stability, etc. under various loading conditions. Several approaches including numerical, analytical and coupled numerical-experimental, are being adopted to achieve these objectives. Rice's J-integral approach [2] is used for the analysis of pre-existing crack. It cannot be directly applied for crack initiation and propagation from a notch due to large scale yielding. The two parameters J–Q approach proposed by O'Dowd and Shih [3, 4] for notches, however, cannot be applied to complex geometries such as welds due to plastic mismatch between base and weld materials. Similarly, the crack tip opening displacement (CTOD) or crack tip opening angle (CTOA) approach is also not suitable for welds [5]. These global approaches are implemented in commercial FE code, ABAQUS. These are best suitable for predefined known crack path and exhibit mesh size dependency [6].

The limitations of global approach have been overcome by more physically-based descriptions of fracture, which is referred to as "Local approach to fracture" [7]. The damage and rupture are represented in the volume (continuum damage mechanics). A non-predefined crack path could be modeled using advanced numerical techniques such as X-FEM [8] based on the partition of unity method. These methods are available in commercial FE code, ABAQUS.

In the recent past, a coupled form of experimental, analytical and continuum damage mechanics is being adopted to predict fracture in structural components. Tai [9] and McMeeking [10] have used elastic-plastic FE analysis to simulate crack blunting process. Saxena and Ramakrishnan [11] determined stretch zone width (*SZW*) using FEM simulations based on fracture energy density calculated from conventional tensile test data. This may not be a true representation of material's fracture energy unless the localization effects in the post necking regime are taken into account in the stress-strain curve. In the present study, the fracture initiation parameter for 316LN SS is calculated from FEM simulations using local damage approach, which is based on directly measurable quantity from tensile test, i.e., uniform strain and grain size as damage strain and characteristic distance parameters. For crack growth beyond crack initiation, the early work of de Koning [12] showed that CTOA was nearly constant from crack initiation to stable crack growth (SCG). However, later from coupled experimental and finite element analysis Maiti and Mahanty [13] have shown that initial variation of the CTOD/CTOA has a significant role in the prediction of SCG and use of constant CTOD/CTOA leads to an under-estimation of the fracture load. Newman et al. [14]

have presented a comprehensive review on CTOD/CTOA criterion for numerical analyses and its limitations. The proposed crack growth criterion in the present study did account for crack blunting through large deformation FE and X-FEM analyses. The details of the approach and implementation for fracture predictions are discussed in the Chapter-3. The criteria validated at specimen level have been further used to predict fracture in small diameter 316LN SS pipes (discussed in Chapter-6).

Dutta and Kushwaha [15] and Dutta et al. [16] used Rice-Tracey cavity growth model for crack initiation prediction in SA333Gr.6 material. They have overcome the mesh dependency due to cavity growth model by integrating the damage potential over a process zone surrounding the crack tip. They have predicted the fracture load under high triaxiality conditions for compact type (CT) specimens and large thickness pipes under four point bending. In the present study, the Rice-Tracey damage parameter for P91 steel has been evaluated using notch tensile tests, and fracture load predictions were carried out for a range of low stress triaxiality. The details of this approach and implementation for fracture prediction have been discussed in Chapter-4.

1.3 Fracture Mechanics

1.3.1 Ductile Fracture Mechanism

When a ductile material is subjected to monotonically increasing load, any prior existing crack with finite root radius undergoes blunting before further crack initiation and growth. In the plastic process zone ahead of notch or crack, the fracture follows a multi-step failure process involving several concurrent and mutually interactive mechanisms [17]. These are: (a) Nucleation of micro-voids: This can occur either by decohesion of the second-phase particles and inclusions or slip band intersections and impingements on grain boundary, (b) Growth of voids due to localized plastic deformation, (c) Localization of plastic flow in the ligament and instability due to necking between voids, (d) Final tearing or rupture of the ligaments between the enlarged voids.

Voids first initiated at material defects or pre-existing voids in a material grow due to large plastic deformation. The spatial and size distributions as well as the shape of these voids depend on the mechanism of void nucleation (viz., particle cracking/decohesion, slip bands intersections, or slip band impingements on grain boundary) and the stress state prevailing near the crack tip that controls the void growth. McMeeking [18] has done an elaborate study on crack blunting process in elastic-plastic hardening material and correlated it to crack tip opening displacement (CTOD). The gradient of stress existing at notch produces high, locally concentrated strain, and lead to the formation of voids that grow and coalesce and later link with the crack tip. The choice of the appropriate local damage parameter for modeling of crack initiation would be based on the underlying mechanism of void nucleation and growth [19].

Predictive numerical simulations of ductile fracture have become of great interest for fracture analysis at both specimens and components level. The experimental approach is either costly or even impractical for some full-scale components. The finite element method simulations should be able to predict the crack paths and stress states in large size components. Many times coupled experimental-numerical techniques are used to achieve these objectives. These techniques are widely used for fracture predictions in components using global and local fracture approaches and parameters.

1.3.2 Elastic-Plastic Fracture Parameters and Global Approach

Stress intensity factor (*K*), the linear elastic fracture mechanics (LEFM) parameter, which is based on singular crack tip stress-strain fields cannot be applied to cracked components made of low yield stress and high fracture toughness material due to the large plastic deformation present at the crack tip. Unlike high strength and low toughness materials for which failure occurs rapidly after the crack tip K reaches a critical value, the ductile failure typically exhibits three stages; crack initiation, stable crack growth and instability. Crack blunting causes severe strain damage at crack (notch) tip before further crack initiation and growth. Hence, the approaches based on elastic-plastic fracture parameters like Rice *J*-integral, crack tip opening displacement (CTOD) and crack tip opening angle (CTOA) have been widely used for fracture predictions in components.

A few classical fracture mechanics points are discussed here. For a linear elastic cracked body subjected to loading, the stress field in polar coordinate axis with the origin at crack tip is given by the first two terms of Williams[20] series;

$$\sigma_{ij} = \left(\frac{k}{\sqrt{r}}\right) g_{ij}(\theta) + T\delta_{ij}\delta_{ij} \tag{1.1}$$

where σ_{ij} is the stress tensor, r and θ are polar coordinate axes, k is a constant, g_{ij} is a dimensionless function of θ and T is uniform stress in crack propagating direction. The crack tip stress field for Mode-I loading (assuming higher-order terms are negligible) can be written as;

$$\sigma_{ij} = \left(\frac{K_I}{\sqrt{2\pi r}}\right) g_{ij}(\theta) \tag{1.2}$$

where K_I, the Mode-I stress intensity factor, defines the amplitude of the crack tip singularity. That is, stress level near crack tip increases in proportion to K_I and this alone completely defines the crack tip conditions. For Mode-I loading, the shear stress is zero on the crack plane (θ = 0), and it implies that the crack plane is a principal plane. Fig. 1.1 shows the distribution of stress σ_{yy} normal to the crack plane as a function of distance from the crack tip. In reality, materials with yield stress σ_0 will yield when σ_{yy}= $\sigma_0$and a plastic zone of size r_y will exist at the crack tip as it is illustrated.

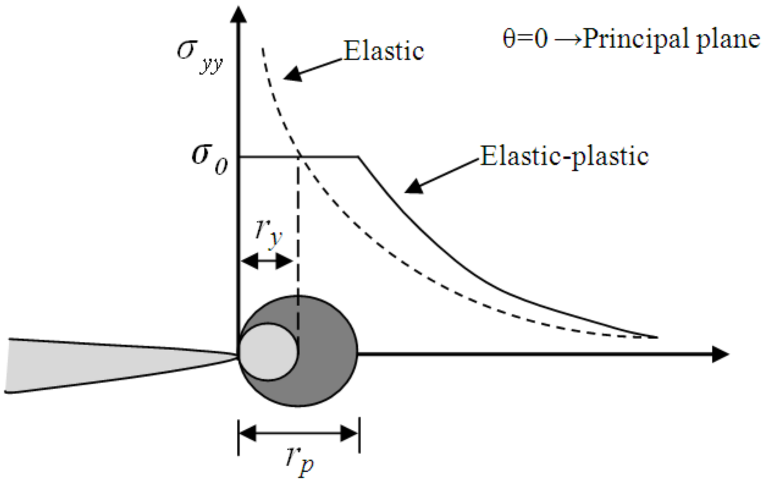

Fig. 1.1 Distribution of σ_{yy} and size of the plastic zone in a stationary crack

The second-order approximation (with Irwin's correction for virtual crack extension) to the plastic zone is given as r_p. Critical K_I has been used as a fracture parameter in LEFM (i.e., when the plastic deformation of crack tip is confined to a very small region around crack tip) to define failure of the structure. When the plastic deformation is significant, EPFM parameters like nonlinear energy release rate (*J*) and CTOD have been used as the appropriate fracture parameter. The (size-independent) critical values of these parameters are measures of the fracture toughness under small scale yielding condition. In such cases, unique relationships among *J*, CTOD and K_I exist. The stress beyond a short distance ahead of stationary sharp crack (i.e., beyond the large strain region) is proportional to $\frac{1}{\sqrt{r}}$and this region is referred to as *K*-

dominated region. This region surrounds the *J*-dominated region occurring under monotonic and quasi-static loading, as illustrated in Fig. 1.2. The stress field within the *J*-dominated zone is approximately described using HRR solution, where material flow properties conform to the idealization of Ramberg-Osgood (deformation plasticity) material model given by:

$$\frac{\varepsilon}{\varepsilon_0} = \frac{\sigma}{\sigma_0} + \alpha\left(\frac{\sigma}{\sigma_0}\right)^n \tag{1.3}$$

where $\varepsilon_0 = \sigma_0 / E$, σ_0 is a reference stress value that is usually equal to the yield strength, α is the dimensionless constant and *n* is the strain hardening exponent. HRR solution is given by:

$$\sigma_{ij} = \sigma_0 \left(\frac{EJ}{\alpha \sigma_0^2 I_n r}\right)^{\frac{1}{n+1}} \bar{\sigma}_{ij}(n, \theta) \tag{1.4}$$

σ_{ij} is the actual stress distribution, I_n is an integration constant that depends on *n,* σ_{ij} are the dimensionless functions of *n* and *θ*, and *J* is Rice's path-independent line integral given by:

$$J = \int_{\Gamma} \left(w dy - T_i \frac{\partial u_i}{\partial x} ds\right) \tag{1.5}$$

where $w = \int_0^{\varepsilon_{ij}} \sigma_{ij}\, d\varepsilon_{ij}$ is the strain energy density, $\sigma_{ij}, \varepsilon_{ij}$ are the stress and strain tensors, $T_i = \sigma_{ij} n_{ij}$ is the component of traction vector, traction is a stress vector normal to the contour Γ, n_{ij} is the component of the unit vector normal to Γ, *ds* is a length increment along the contour Γ, u_i is the displacement vector. The stress field varies within the HRR field as $1/_{r^{(1/n+1)}}$. The finite strain region occurs within a distance of approximately *2*×CTODfrom the crack tip [18]. The large scale yielding effects at the crack tip will result in loss of the HRR singularity because the size of the finite strain zone becomes significant relative to the geometrical dimensions of the cracked body. On loading, a prior existing sharp crack gets blunted and no longer will describe the stress-strain fields near the notch tip. For design purposes, the maximum stresses σ_{yy} that act at notch tips are usually calculated by using a geometry-dependent, stress concentration factor, K_t to multiply the nominal stress σ_n calculated considering no notch effect on the material body. In the above-mentioned cases, the region cannot be uniquely characterized by the single-parameter fracture mechanics especially for low yield stress and high toughness materials.

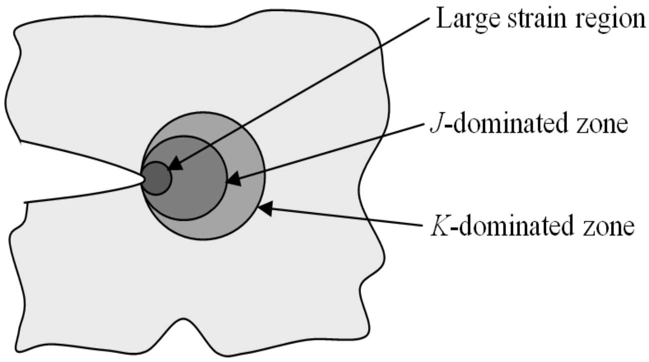

Fig. 1.2 Crack tip with small scale yielding condition

The J_i value exhibits a size and geometry dependence, and the J-integral becomes path dependent as soon as plasticity occurs and the contour 'Γ' passes through the plastic zone. Under small-scale yield condition, path independent J-integral value can be calculated by choosing a path, which completely surrounds the plastic zone. This is not possible in the case of gross plasticity due to extensive crack blunting in low yield stress materials and pronounced path-dependence will always occur. However "saturated" J-integral value reached in the "far-field" remote from the crack tip $J_{tip} \leq J_{(r)} \leq J_{far\ field}$ is related to the global energy release rate as [18]:

$$J = G = -(\partial U / \partial A) \quad (1.6)$$

The experimentally evaluated J as per ASTM E1820 for plane crack extension with straight crack front being a global energy parameter represents the saturated J-integral value.

1.3.3 Continuum Damage Parameter and Local Approach

There are two independent numerical modeling approaches, namely (i) coupled plasticity and damage and (ii) uncoupled plasticity and damage approaches are being adopted for ductile fracture analysis [19, 20]. The first approach incorporates parameters for void volume fraction at different stages of deformation/damage into the constitutive relationship between stress and strain in a material. This represents the softening effect due to the accumulation of voids in the material. Thus, a function, which describes the nucleation, growth and coalescence of voids, is defined and incorporated in the formulation. The Gurson-Tvergaard-Needleman [21] model and the Rousellier model [22] belong to this category. In principle, the identification of material parameters for these models requires intermittent strain level tests and metallurgical observations for void size and distribution. However, in most of the literature, the required parameters are assessed by fine-tuning a few critical parameters in order to reproduce force-displacement results of notch tensile test. Hence, the uniqueness and transferability of the material parameters is not justified. Further, the coupled models are mesh-size dependent and enormous computational time is required for analysis of a real-life component of the piping system and pressure vessel etc.

The uncoupled model approach is relatively a simple strategy for ductile fracture prediction. In this, damage and yielding behaviour are uncoupled. The material is assumed to follow the von-Mises yield criteria with the appropriate flow and strain-hardening rules. A damage potential symptomatic of void growth is calculated in post-processing manner at a large number of sampling points ahead of crack/notch tip against applied loads. A critical value of this parameter signifying crack initiation is obtained by comparing the computed value with the experimental result for a standard fracture specimen. The critical value of the potential validated at specimen level can then be used to ascertain crack initiation in other real life components. Rice and Tracey’s [23] cavity growth model belongs to this category.

1.3.3 (a) Critical Strain at a Characteristic Distance

Different criticality criteria namely, critical stress, stress modified critical strain, and ductility-based critical strain has been used in literature along with size and spacing of void-nucleating sites for defining the characteristic length and void growth models for prediction of crack initiation in metallic materials [23-26].

1.3.3 (b) Rice and Tracey’s Void Growth Model

Rice and Tracey [23] and McClintock [26] have independently introduced micromechanical models for ductile damage. McClintock described the damage by considering the growth of isolated cylindrical void and Rice and Tracey by growth of isolated spherical void in a rigid perfectly plastic material. Both studies outlined the combined role of stress triaxiality and plastic strain on void growth. A more realistic spherical shape void growth model (Rice-Tracey) has become popular. In this model, the damage potential is considered to be the equivalent cavity radius R. The growth of a single isolated spherical void in an infinite block of elastic-plastic strain-hardening material is given as [23]:

$$\frac{\dot{R}}{\dot{\varepsilon} R_0} = \alpha \exp(1.5\varphi) \tag{1.7}$$

where R_0 – initial void radius, $\dot{\varepsilon}$ - strain rate

Here α is a constant and its value has been derived as 0.283 for a high degree of stress triaxiality (φ)defined as;

$$\varphi = \frac{(\sigma_1+\sigma_2+\sigma_3)/3}{\sqrt{\frac{1}{2}[(\sigma_1-\sigma_2)^2+(\sigma_2-\sigma_3)^2+(\sigma_3-\sigma_1)^2]}} \qquad (1.8)$$

where $\sigma_1, \sigma_2, \sigma_3$ are principal stresses.

1.4 An Overview of Materials Used in the Present Study:

1.4.1 AISI Type 316 LN Stainless Steel

Austenitic stainless steels are used as the major structural materials for PFBR in view of their high temperature mechanical properties, compatibility with liquid sodium coolant, good weldability, good irradiation resistance and satisfactory experience in the use of these steels in sodium cooled reactors. For the structural components of the Fast Breeder Test Reactor which attained criticality in 1985 at Kalpakkam, austenitic stainless steel grade 316 is the principal grade used. For PFBR, low carbon (<0.03 wt%) austenitic stainless steel types 304 and 316, alloyed with 0.06-0.08 wt% nitrogen, designated as 304LN and 316LN SS respectively have been selected for the structural components. These low carbon grades have been chosen to ensure freedom from sensitization during welding of the components to avoid the risk of chloride stress corrosion cracking during storage in coastal site. Since low carbon grades have lower strength than normal grades, nitrogen is specified as an alloying element to improve the mechanical properties so that the strength is comparable to 304 and 316 SS. Although 304LN and 316LN are specified by ASME with nitrogen in the range of 0.10 to 0.16 wt%, for PFBR, nitrogen content is limited to 0.08 wt% for improved weldability. For components operating at temperatures below 700 K, type 304LN SS is used due to its lower cost while for high temperature components operating in creep range, 316LN SS has been adopted. Other major advantages of austenitic stainless steels 304LN and 316LN include the existence of vast database on mechanical properties and ease of fabrication [27].

Since316LN SS has been chosen as the material of construction for main vessel and hot sodium piping connecting between reactor assembly and steam generator, in the present study, this material has been investigated for fracture behavior assessment.

1.4.2 Modified 9Cr-1Mo Steel

Now-a-days the 9Cr-1Mo steel and associated variants are important steels in power generation industries. The choice of material for the PFBR steam generator is Modified 9Cr-1Mo steel. The selection is based on requirements of high temperature service requirements such as high temperature mechanical properties including creep and low cycle fatigue, resistance to loss of carbon to liquid sodium which leads to a reduction in strength, resistance to wastage in case of small leaks leading to sodium-water reaction and resistance to stress corrosion cracking in sodium and water media. The studies have shown that there is a loss of ambient temperature ductility as a result of ageing at 500-550°C due to segregation of phosphorous to carbide/matrix interfaces and after prolonged ageing, with the precipitation of the Laves phase Fe_2Mo at lath and grain boundaries [28].

1.5 Objectives and Outline of the Research Work

The focus of current research is to develop damage/fracture mechanics methodologies to predict fracture in 316LN SS and P91 base materials and similar weld of 316LN SS as well as dissimilar metal weld between 316LN SS and P91 based on coupled numerical-experimental-analytical methods. This includes (i) Evaluation of *far field* and *modified J*-integral for 316LN SS and its welds using a combination of FEM, X-FEM simulations and experimental data from CT specimen tests. The developed criteria were used to predict crack initiation and propagation from a notch in 316LN SS base and across its weldment. (ii) Evaluation of void growth model (Rice-Tracey) parameter for P91 steel using a combination of FEM simulations and experimental data from notch tensile tests and its use to predict crack initiation under a range of low stress triaxiality conditions. (iii) The damage criteria validated at specimen for 316LN SS material have been used to predict fracture in small size straight pipes.

Chapter 2: Materials, Experimental and Data Analysis Procedures

2.1 Introduction

The mechanical and fracture properties of any material depend on its microstructure, which is based on chemical composition and heat treatments. The properties like yield strength, ultimate tensile strength, strain hardening exponent, ductility etc. are dependent on microstructural features like grain size, dislocation density, size and shape of precipitates and their distribution. The fracture strength of materials is dependent on yield strength, strain hardening exponent and precipitate's size, shape, and its distribution around the crack or material discontinuities. Usually, the mechanical properties like yield strength, UTS and ductility parameters are obtained from conventional tensile tests. But for assessment of damage parameters to establish a fracture criterion or continuum damage model's parameters requires strain-displacement fields of deforming material region. Here, the strain distribution field during tensile deformation of notched specimens was assessed using digital image correlation (DIC) technique. The experimental assessment of material and components *J*-R curve depends on geometry, loading conditions, the accuracy of measurement devices/accessories etc. The testing machines, accessories and geometry of test specimens used in the present study is presented in this chapter. Also, the experimental details of the materials characterization carried out by optical microscopy and SEM are outlined.

2.2 Materials

2.2.1 AISI Type 316LN Stainless Steel

AISI type 316LN austenitic stainless steel (316LN SS) in solution annealed condition is the starting material. Its chemical composition, in weight percent, is given in Table 2.1. The optical micrograph of 316LN SS is shown in Fig. 2.1(a), which consists of fully equiaxed austenite grains with annealing twins. Based on the intercept method ASTM-E112-10 [29], the average grain size of 316LN SS has been estimated to be 82±9 μm. Further, the individual grain size has been measured using "imageJ" software by taking average length of three lines drawn at 120° apart within the grain. Both methods have shown a very close agreement. The grain size histogram is shown in Fig. 2.1(b). The mean value of grain size calculated from the histogram is 87μm.

Table 2.1 Chemical composition of 316LN SS (in wt %)

C	Si	Mn	Cr	Ni	N	Mo	P	S	Fe
0.027	0.22	1.7	17.5	12.22	0.07	2.49	0.01	0.01	Bal.

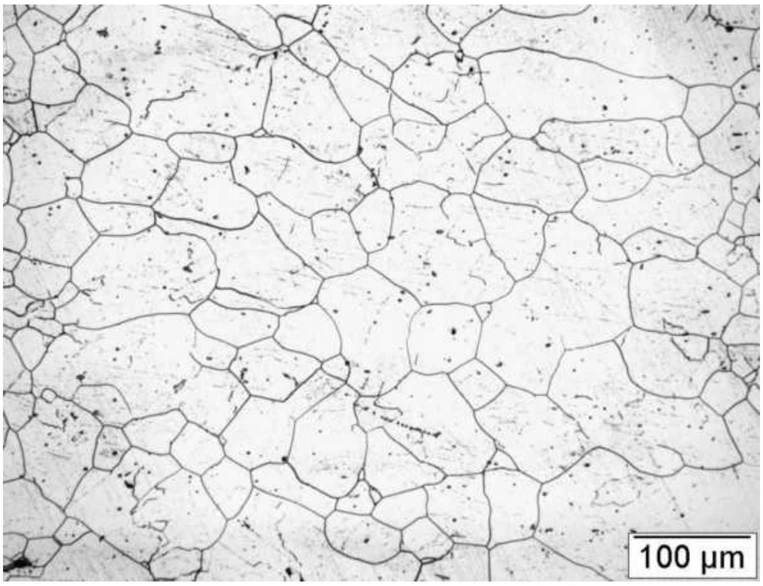

Fig. 2.1(a) Optical micrograph of 316LN SS

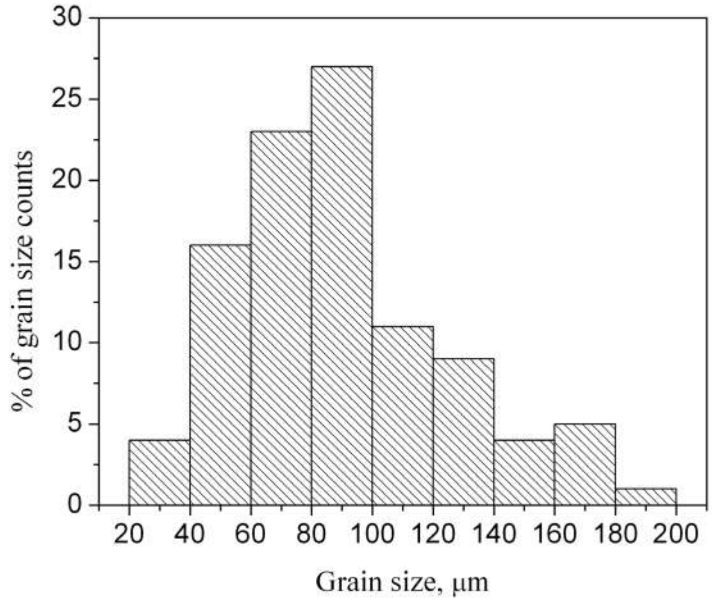

Fig. 2.1(b) Grain size histogram of 316LN SS

2.2.2 Mod. 9Cr-1Mo steel

Modified 9Cr- 1Mo ferritic steel (P91) in normalized and tempered (N&T) condition is the starting material. Its chemical composition, in weight percent, is given in Table 2.2.

Table 2.2 Chemical Composition of Mod.9Cr-1Mo steel (in wt %)

C	Mn	P	S	Si	Cr	Mo	Ni	Al	Nb	V	N	Fe
0.12	0.38	0.02	0.007	0.47	9.42	1	0.13	0.021	0.1	0.25	0.068	Bal.

The microstructure of the P91 base metal is shown in Fig. 2.2. It consists of tempered lath martensite structure with prior austenitic grain boundaries, and the precipitates are distributed at inter lath and intra lath regions. These precipitates are mainly $M_{23}C_6$ type carbides, and some of Nb and V rich (C, N) precipitates are also present.

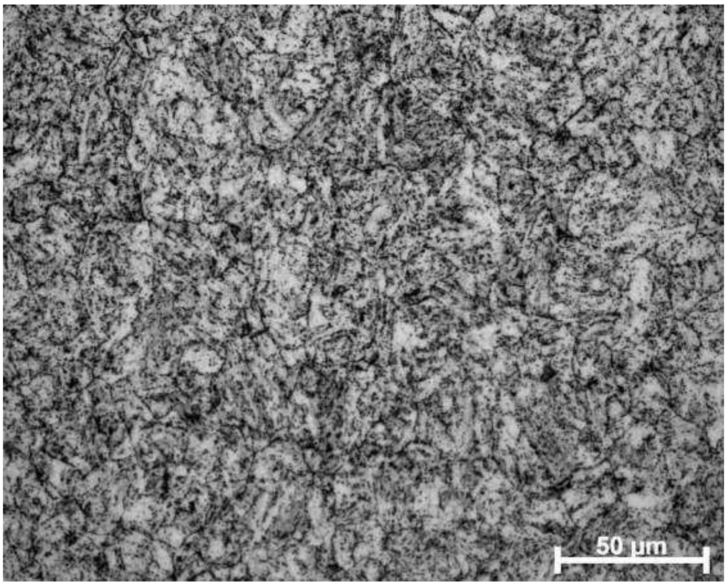

Fig. 2.2 Optical micrograph of P91 base material

2.3 Testing Machines and Accessories

2.3.1 Conventional Tensile Testing machine

Uniaxial tensile tests were carried out using 250kN screw driven, electromechanical computer servo-control testing machine (make: HUNG TA 2402). The tests were conducted at 1.3×10^{-4} /s strain rate at ambient temperature. The applied load was measured with a load cell accuracy of ±1% within the full scale. The tests were conducted in displacement control mode with real time fuzzy controller consists of 24 bit A/D and 16 D/A converters and a servo motor. The load and displacement data were acquired at 10 Hz. The testing system with camera arrangement for acquiring 2D images of the test specimen for DIC analysis is shown in Fig. 2.3(a).

2.3.2 Digital Image Correlation technique

Digital image correlation (DIC) is a widely accepted and commonly used full-field optical technique for displacement and strain measurements.

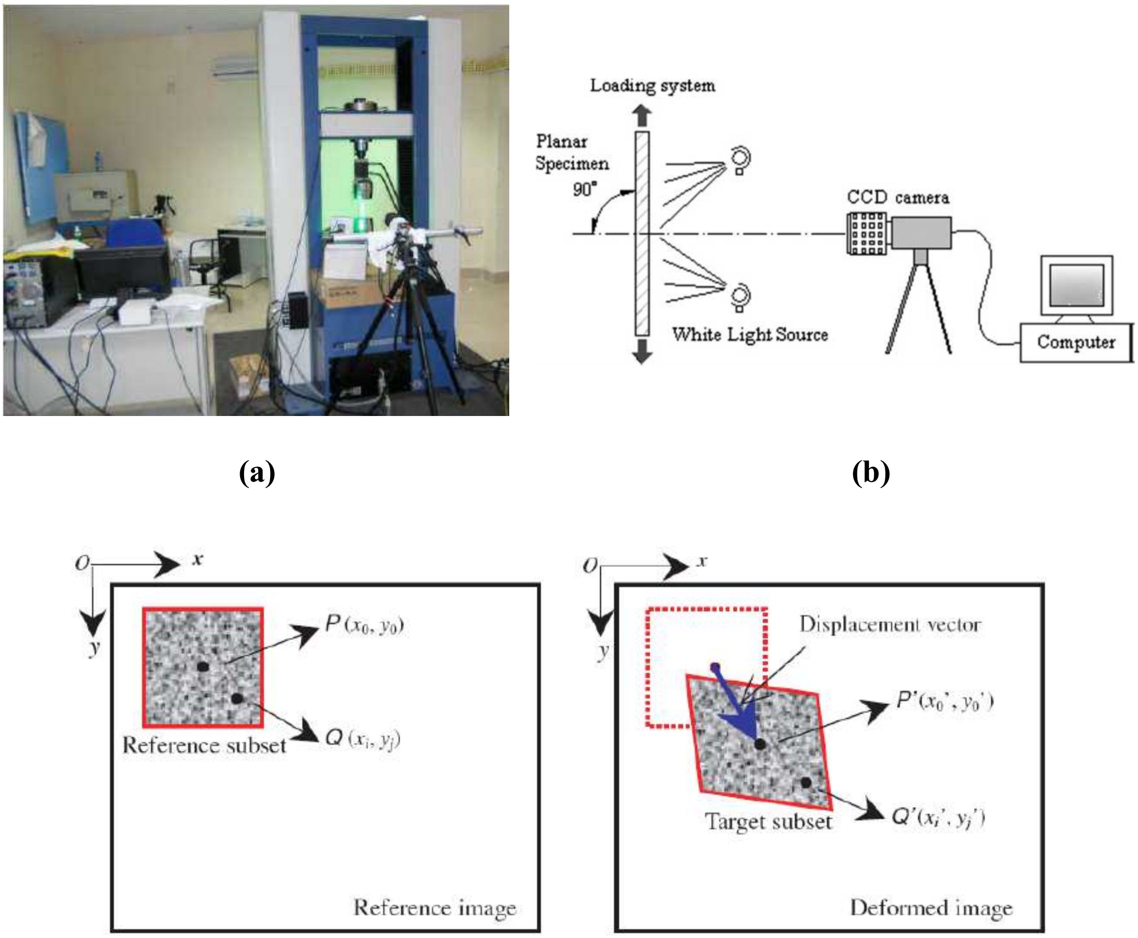

(c)

Fig. 2.3 (a) Tensile test set-up with CCD camera arrangement (b) Typical optical image acquisition system for the 2D DIC method (c) Schematic illustration of a reference square subset before deformation and a target (or deformed) subset after deformation [from Ref: 2]

The DIC technique is a non-contact measurement method based on mathematical comparison of grey intensity value of the region of interest in the images before and after the deformation of the test specimen. The two-dimensional (2D) DIC method with a single fixed CCD camera is used to obtain in-plane deformation measurements. Special attention must be given to the arrangement of specimen, light sources and camera because the accuracy and consistency of measurement depend heavily on the imaging system set-up. A typical 2D DIC measurement set up is shown in Fig. 2.3(b).

The implementation of the 2D DIC method comprises: (1) specimen and experimental preparations; (2) recording images of the planar specimen surface before and after loading and (3) processing the acquired images using a computer program to obtain the desired information on displacement and strain. The acquired images are divided into subsets containing a finite number of pixels. The spatial resolution and accuracy of displacement are limited by the number of pixels and subset size. The basic principle of 2D DIC is the tracking(or matching) the area of unique light intensity distribution inside the subset between the two images recorded before and after deformation as schematically illustrated in Fig. 2.3(c) [30]. The accuracy of the DIC technique depends on correlation algorithm and processing parameters such as subset size, shape function selection, methods of obtaining sub-pixel accuracy and the quality of the speckle pattern [31].

CMOS camera (Marlin-F131) is focused on the flat surface of the specimen. The camera was carefully setup so that the optic axis is perpendicular to the flat surface of the specimen. The specimens were coated with white paint on the surface. The surface of the specimen facing camera is sprayed with black paint using spray gun to form very small and random speckle pattern. The resolution of the CMOS camera used is 1380×1035 pixels leading to a field of view of 240×180 mm^2 and 0.17 mm pixel size for the combination of lenses and focal distance used in the present investigation. To eliminate reflections from surrounding light, green LED light source is employed to illuminate the sample, and a corresponding filter is used to let reflected light go through the camera lens. The captured 2-D images were used in Vic-2D commercial DIC software to get strain fields. To achieve sub-pixel accuracy, the correlation algorithms of Vic-2D use grey value interpolation, representing a field of discrete grey levels as continuous splines of order 4, 6, or 8 that may be selected here. Higher-order splines provide accurate displacement information, and lower-order splines provide faster correlation at the expense of some accuracy. The subset size of 29×29 pixels and 181 μm spatial resolutions is used with a frame rate of 10 Hz. The overall strain resolution of the system is 50 με.

2.4 Fracture Tests on CT specimens

The sharp pre-crack ahead of wire-cut notch in CT specimens (details of the CT specimens are discussed later) were introduced using a resonant type (RUMUL) fatigue machine shown in Fig. 2.4(a). The fatigue pre- cracking was done under load control

Fig. 2.4(a) Resonant type fatigue pre-cracking machine **(b)** Servo-hydraulic testing machine for fracture tests

mode with sinusoidal waveform at load ratio $R = 0.1$ ensuring that the loads did not exceed the limits prescribed by ASTM E1820 [32]. The initial value of fatigue force was kept 10 kN [K_I=24.15 MPa(m)$^{0.5}$] and gradually reduced to 5 kN [K_I=12.07 MPa(m)$^{0.5}$] on reaching a ~ 5 mm crack growth on either side of the sample. The fracture tests were carried out at a constant stroke rate of 0.01 mm/s using 250 kN servo-hydraulic machine (INSTRON 8033) which is fully automated for test control and data acquisition as shown in Fig. 2.4(b). The load-line displacement (LLD) was monitored using crack opening displacement (COD) gage (EPSILON). The gage is a clip-on type with metallic arms suitable for mounting on knife edges of the sample. The gage resolution is 0.001 mm with total opening travel of 8 mm. High resolution load (P), LLD and crack length (a) data were recorded using the data acquisition software integrated with the test application. The online crack length measurement was carried out using a calibrated direct current potential drop (DCPD) technique. It is based on the change in resistance of the material with an increase in crack length. As the crack grows, electrical resistance of the specimen increases, hence there is an increase in potential drop across the measurement points. The current (input) and voltage (output) leads are welded to the samples for DCPD measurement. The voltage/current leads were welded diagonally across the notch to average out the effects of irregularities of the crack front through the specimen thickness. In order to ensure close to plane strain condition ahead of crack front, the samples were side grooved with 10% reduction in thickness (25 mm) on each side of the sample. Also, the side grooves help to eliminate the surface shear lip formation and achieve straight crack front [33]. The voltage across the crack mouth has been measured before and after side grooving with a constant current input of 10 A. Crack length was estimated from calibration curves which are plots between V_i/V_o and a/W. Linear interpolation is used to infer the crack lengths. In order to distinguish the ductile growth regime, the tested specimens were subjected to fatigue post-cracking. The initial (a_o) and final (a_f) crack lengths were optically determined using the nine-point average method as prescribed in ASTM E1820 [32].

The crack length obtained from optical measurement is used to verify the DCPD based measurement.

2.5 Fracture Tests on Pipe Specimens

2.5.1 Fatigue Pre-cracking

Before carrying out fracture tests, fatigue pre-cracking of the pipe specimens with circumferential U-notch of root radius 1.5 mm was carried out in order to produce a sharp crack front. It was carried out under four-point bending, under load control, using a ±50 kN capacity servo-hydraulic actuator (Fig. 2.5) employing constant amplitude sinusoidal cyclic loading. The maximum load during pre-cracking was approximately 20% of the Theoretical Plastic Collapse Load (TPCL) of the pipe specimen. The TPCL was calculated using the following equation [34].

$$P_L = \frac{16t\sigma_f R_m^2}{Z-L}\left(\cos\frac{\theta}{4} - \frac{1}{2}\sin\frac{\theta}{2}\right) \tag{2.1}$$

where R_m is the mean radius of the pipe, t is the thickness of the pipe, σ_f is the flow stress of the material, which is defined as the mean of yield strength and ultimate tensile strength, Z and L are outer and inner spans respectively, and θ is the half crack angle. Figure 2.5 shows fatigue pre-cracking on a straight pipe. The specimens were fatigue pre-cracked till the crack growth in circumferential direction reached approximately 2 to 3 mm at both the notch tips.

Fig. 2.5 Fatigue pre-cracking on a straight pipe

2.5.2 Fracture Test Set-up

After fatigue pre-cracking, the pipe specimens were subjected to monotonic fracture under four-point bending, under displacement control, using a ±500 kN capacity Universal Testing Machine (UTM) with an in-built load cell for measuring the applied load. Linear variable displacement transducer (LVDT) is used for measuring load-line displacement. Fig. 2.6(a) shows the set-up for fracture test on a straight pipe. Fig. 2.6(b) shows a close-up view of the fracture test set-up and Fig. 2.6(c) shows a close-up view of instrumentation during fracture test. Quasi-static monotonic load was applied in displacement control at the rate of 0.04 mm/s. Initially, the specimen was loaded till a displacement of 4 to 5 mm was reached and then unloaded till the displacement value drops by 1.5 to 2.0 mm. The procedure was continued in this manner till the load drops below half of the maximum load. During the fracture tests, load, load-line displacement, crack opening displacement and deflection of the pipes (at three locations) were continuously monitored.

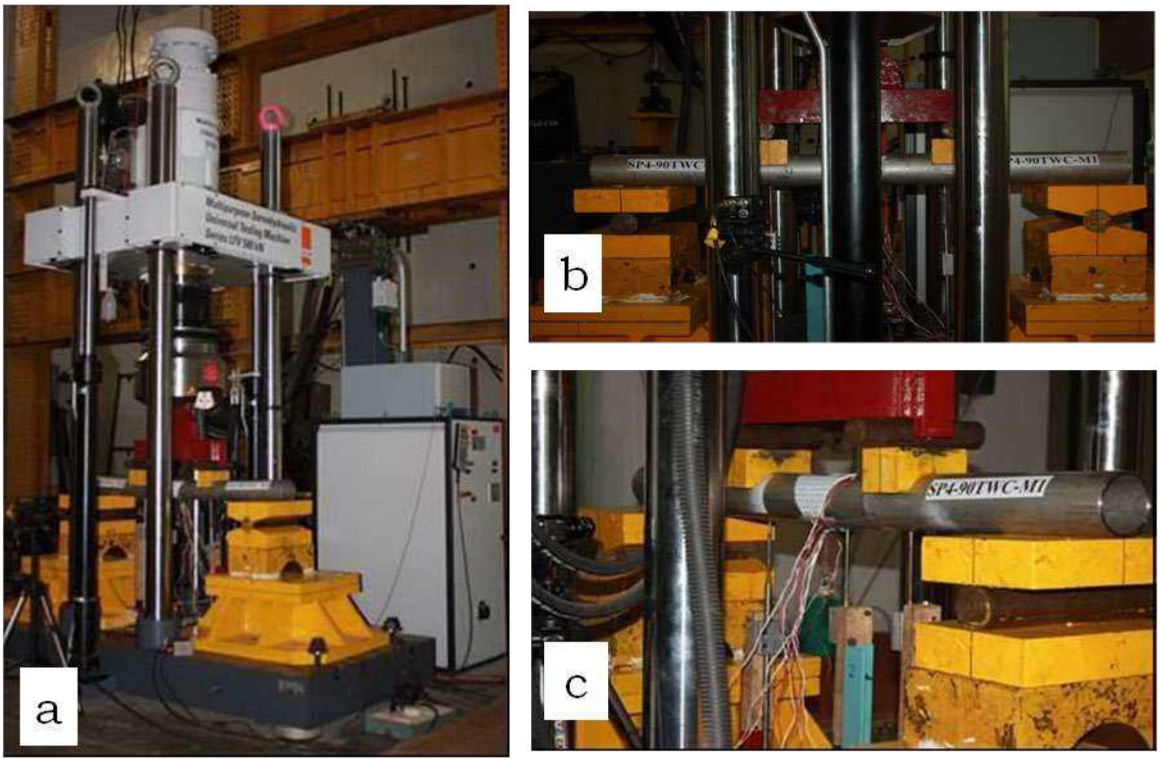

Fig. 2.6 Fracture test on a straight pipe (a) Experimental set-up (b) Close-up view of Loading frame (c) Close-up of instrumentation

Surface crack growth was monitored using Image Processing Technique (IPT). The load- line displacement was measured using in-built LVDT, crack mouth opening displacement was measured using specially fabricated clip gauges. Strain-gauge-based clip gauges with an opening of 5-30 mm and 15-60 mm were used, and these were calibrated prior to the tests for the required range of displacement. IPT was used to measure surface crack growth at both the crack tips. The IPT consisted of three CCD cameras interfaced to a computer system with image analysis software. Two CCD cameras were focused towards the crack tips. A grid of 5 mm spacing is made on the pipe near the crack tips to obtain the crack growth data. The third CCD camera was focused towards the control console of the actuator to record the images of load and displacement corresponding to the crack growth at various stages of loading. The images at the two crack tips give the surface crack growth. The deflection of the pipe was measured by means of ±100 mm range LVDTs kept along the span of the pipe. The LVDTs were connected to data logger interfaced to a computer. Fig.2.7 shows the details of LVDT locations for deflection measurements during the fracture tests.

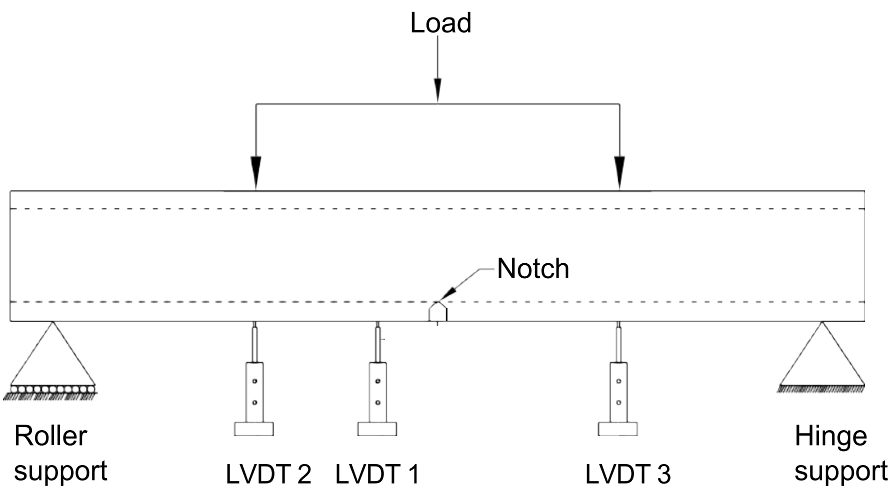

Fig. 2.7 Schematic view of four point bend test and location of LVDTs

2.6 Details of Test Specimens

2.6.1 Mod. 9Cr-1Mo Steel Specimens

To assess the Rice-Tracey model parameter for prediction of crack initiation in P91 steel, a set of tensile tests have been carried out. Since the wall thickness of P91 steel tubes used in steam generators is in the range of 2-2.5 mm. In the present study, thickness of the specimens is kept as 2.3mm, which is same as that of PFBR steam generator tubes. Dog-bone type flat tensile, round notched and central notched specimens as per drawing shown in Fig. 2.8 have been fabricated from N&T P91 steel plate. The details of the test matrix for these specimens are given in Table 2.3.

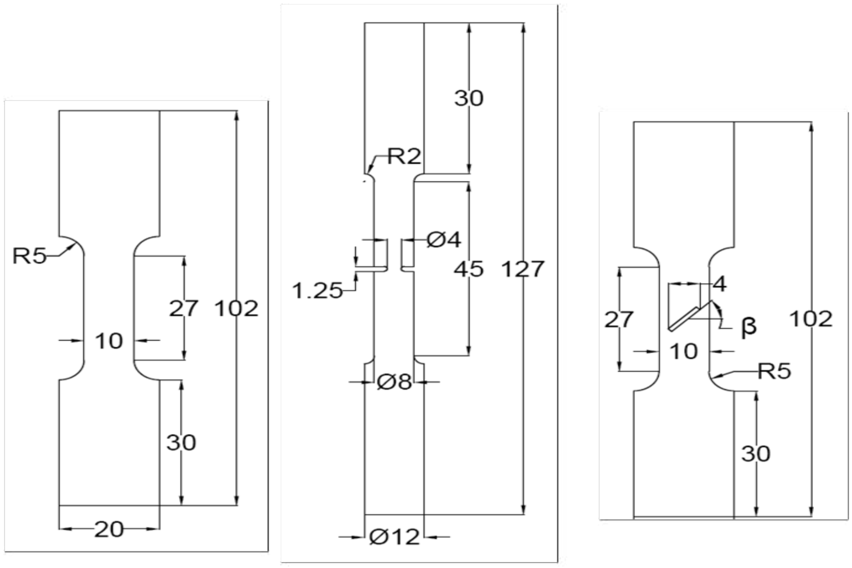

(a) (b) (c)

Fig. 2.8 Details of tensile specimens (a) dog-bone type flat (b) round-notched (c) central notched

Table 2.3 Details of P91 specimens

Fig. 2.8	Type	Nomenclature	Nos.
a	Flat	Dog-bone	3
b	Round-notched	Notch diameter	
		6 mm (C1)	3
		4 mm (C2)	3
c	Flat-central notched	Angle, β	
		F30	3
		F45	3
		F60	3
		F90	3

2.6.2 316LN Stainless Steel Specimens

2.6.2 (a) Preparation of Base CT specimens

CT specimens have been fabricated as per the dimensions specified in ASTM

E1820 [32] and the drawing shown in Fig. 2.9. The details of CT specimens used for validation of crack initiation and growth criteria are provided in Table 2.4.

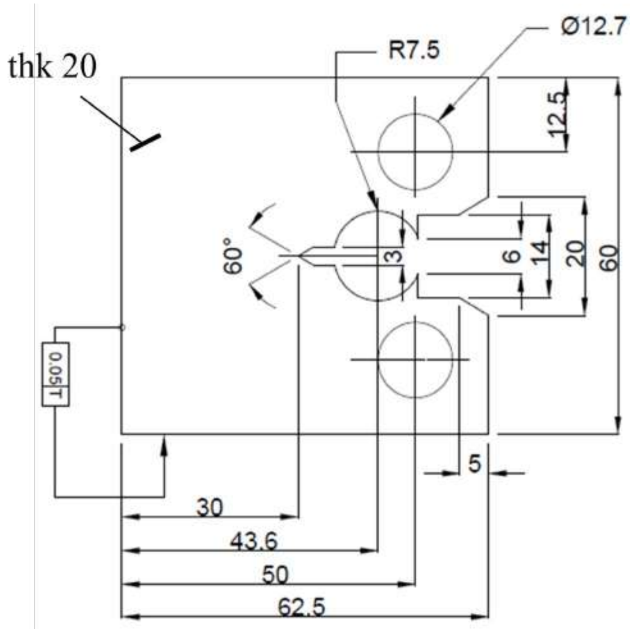

All dimensions are in mm

Fig. 2.9 CT specimen dimensions as per ASTM E1820

Table 2.4 Base material CT specimens

Notch type	*a*/W	Nos
EDM wire cut blunt notch with 0.15 mm root radius	0.4	1
	0.5	1
	0.6	1
	0.7	1
Fatigue pre-cracked sharp crack	0.39	1
	0.55	1
	0.64	1
	0.72	1

2.6.2 (b) Similar and Dissimilar Weld CT specimens

A 30 mm thick weld pad with butt weld groove of total 20° bevel angle and 14 mm root gap as shown in Fig. 2.10 was made by multi-pass shielded metal arc welding (SMAW) process using E316-15 electrode. X-ray radiography has been carried out to ensure the welds are free from detectable defects like cracks, inclusions etc. The CT specimens are fabricated as per sketch shown in Fig. 2.11(a-d). The crack growth behavior of weld is important because the initiating flaws are likely to exist in the weld. However, there are many possibilities that the crack initiated from outside the weldment could approach the weld and pass through weldment consisting of base, HAZ and weld interfaces. Towards this, one CT specimen with a crack plane parallel to weldment and other three numbers with the crack plane perpendicular to the weldment has been fabricated. The notch with root radius 0.15 mm was introduced by electric discharge machining process followed by fatigue pre-cracking. The details of similar and dissimilar weld CT specimens used in the present work are given in Table 2.5.

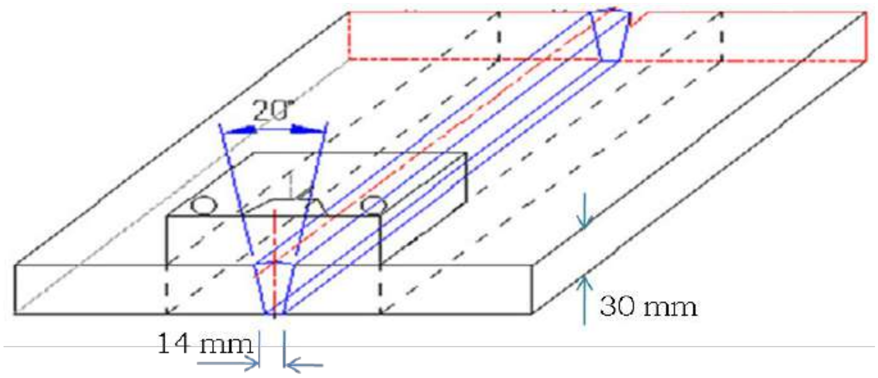

Fig. 2.10 Details of similar weld pad (316LN SS)

Table 2.5 Details of similar and dissimilar weld CT specimens

Notch in	Initial crack tip in	Nos.	As shown in figure
Similar weld with crack parallel to the weld	Weld (CT-PL)	1	Fig. 2.11(a)
Similar weld specimen with crack propagating across weldment	Weld (CT-W)	1	Fig. 2.11(b)
	Interface (CT-I)	1	Fig. 2.11(c)
	Base (CT-B)	1	Fig. 2.11(d)
Dissimilar weld specimen with crack propagating along HAZ, Butter layer, Weld	HAZ (CT-HAZ)	2	Fig. 2.13(a)
	Butter layer (CT-BL)	2	Fig. 2.13(b)
	Weld (CT-DMW)	2	Fig. 2.13(c)

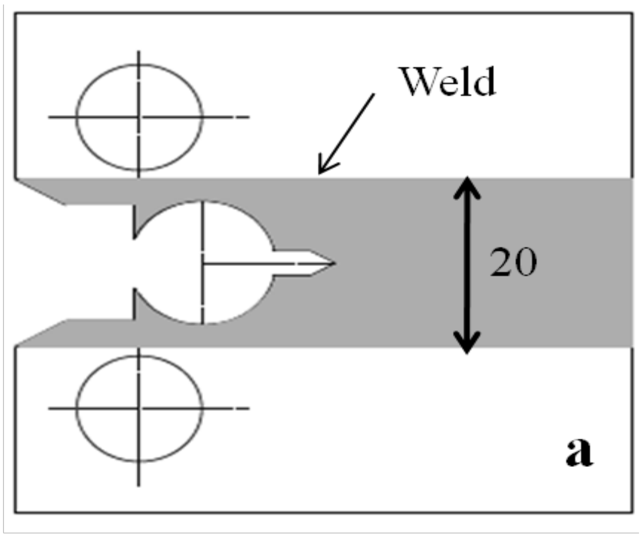

Fig. 2.11 Details of similar weld CT specimen (a) CT-PL

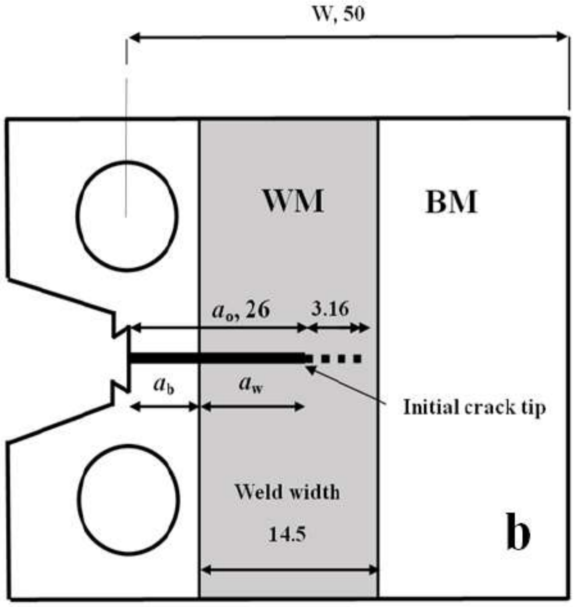

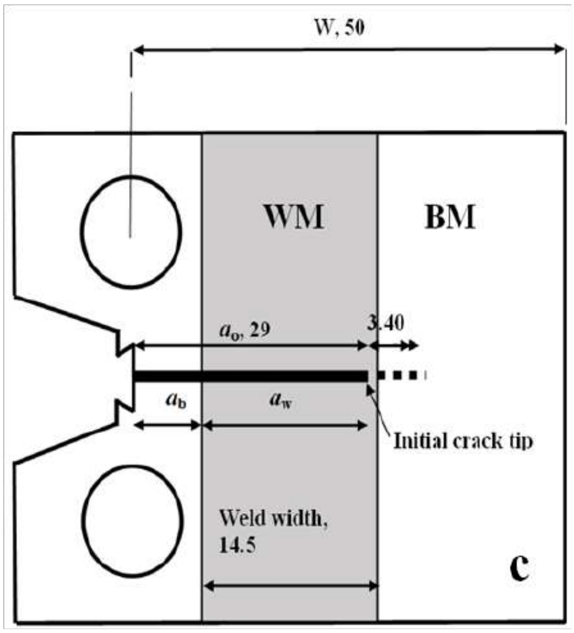

Fig. 2.11 Details of similar weld CT specimen (b) CT-W and (c) CT-I

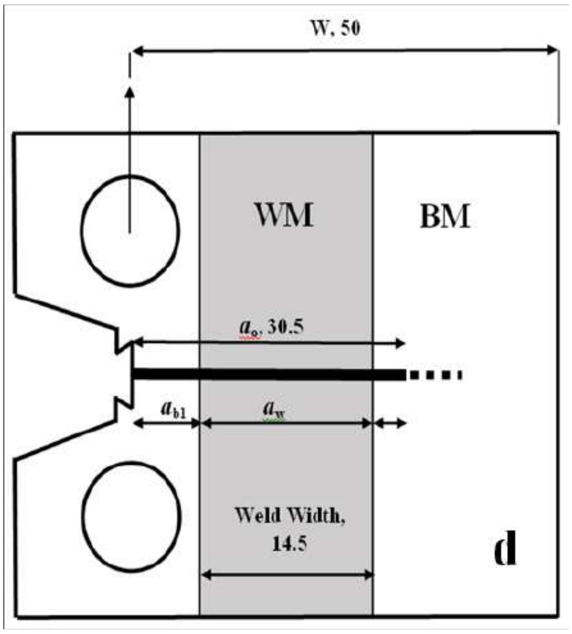

Fig. 2.11 Details of similar weld CT specimen (d) CT-B

Dissimilar metal (316LN SS - P91) weld joint using IN182 consumables (electrode dia. 3.12 mm) and shielded metal arc welding (SMAW) process has been prepared after IN 182 buttering. The root passes are carried out using IN 82 filler wire (wire dia. 1.2 mm AWS A5.14, ERNiCr-3) and gas tungsten arc welding (GTAW) process. After IN 182 buttering on P91 plate, it is subjected to post weld heat treatment at 760°C for 2hrs with a heating rate of 150°C/hr followed by furnace cooling. Weld pad of K-Joint configuration with root gap 2 mm as shown in Fig. 2.12 and using welding parameters as shown in Table 2.6 was prepared in 1G position.

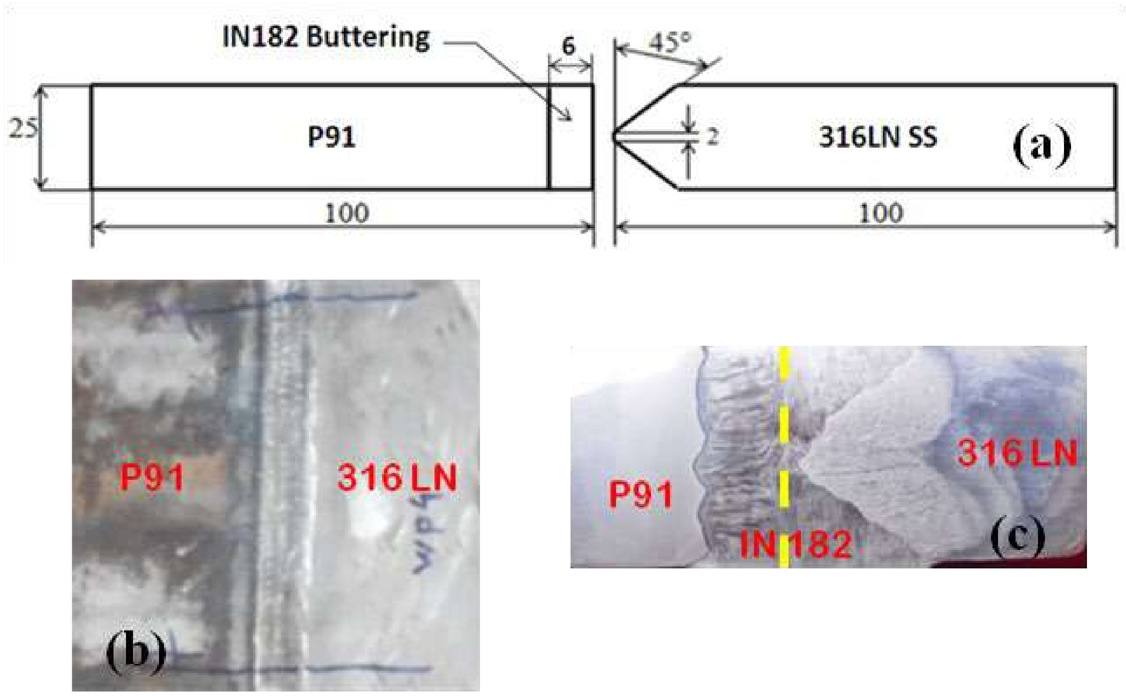

Fig. 2.12 DMW joint (a) K-Joint configuration (b) weld pad (c) Etched regions

Table 2.6 Details of weld parameters for DMW joint

Process	Pass	Current (A)	Voltage (V)	Travel Speed (mm/min)	Heat Input (kJ/mm)	Remark
IN 182 Butter	-	80	22	150	0.56	Pre-heat and inter pass temp. 250°C
GTAW	1-2	120	18	100	0.76	
SMAW	3-X	70-85	20-23	140-160	0.48-0.59	

X-ray radiography was carried out to ensure the welds are free from defects. The CT specimens are extracted with an initial crack in P91-HAZ, IN 182 buttering, IN 82/182 welding and as shown in Fig. 2.13(a-c). The notch was introduced by EDM wire cutting followed by fatigue pre-cracking.

Fig. 2.13 Location of the initial crack in DMW CT specimens (a) P91-HAZ (b) IN 182 buttering (c) IN 82/182 welding

2.6.2 (c) *Specimens for Mechanical Behavior Characterization of DMW Joint*

Small tensile specimens, as shown in Fig. 2.14(a) have been extracted from the base, HAZ, buttering and weld regions of the DMW joint to assess deformation behavior of each region. In order to assess the notch strength of HAZ, buttering and weld regions, notch tensile specimens as shown in Fig. 2.14(b) are extracted from weld pad such that the notch tips are placed in P91-HAZ, IN182 butter layer and IN182 weld.

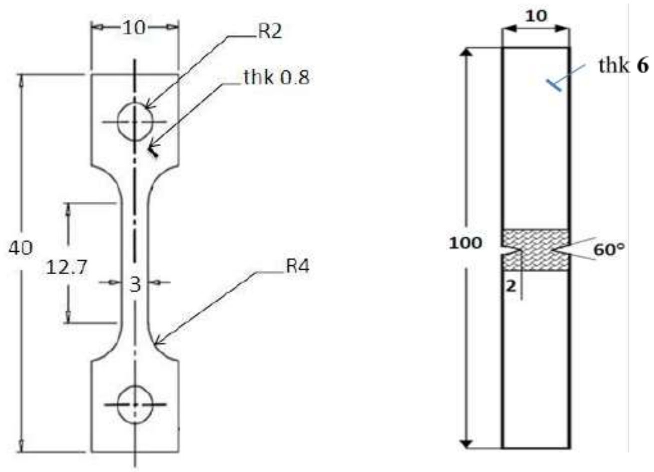

All dimensions are in mm

Fig. 2.14 Tensile test specimens(a)Small size tensile specimen (b) Notch tensile specimen

2.7 Preparation Base and Weld Pipe Specimens

The seamless pipe specimens were fabricated from 316LN pipe of 80 NB, Sch. 40 category (OD 88.9 mm x 5.49 mm thick). The circumferential through-wall notch was introduced at mid-span of length. The girth welded pipe specimens with weld configuration as shown in Fig.2.15 are prepared using 16-8-2 filler wire for root pass and modified E316-15 electrode for subsequent passes. The root passes are made by gas tungsten arc welding (GTAW) procedure and subsequent passes by shielded metal arc welding (SMAW) procedure. Circumferential U-notch of root radius 1.5 mm has been introduced in seamless and welded specimens. The details of the specimens are shown in Table 2.5.

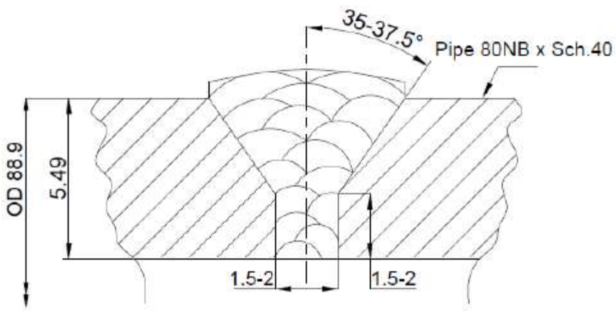

Fig. 2.15 Details of pipe weld configuration

Table 2.5 Details of pipe specimens

Specimen ID	Crack location	Inner Span (mm)	Outer Span (mm)	Fatigue pre-cracking Load(kN)		Frequency (Hz)	Number of cycles	Fatigue pre-crack Length (mm)		Notch angle (pre-cracked) ($2\theta^{\circ}$)
				Max. (Pmax)	Min. (Pmin)			Tip "A"	Tip "B"	
SP4-90TWC-M1	Base	400	1000	10	1	1.0-2.0	5,05,000	2.45	2.80	96.89
SP4-120TWC-M2	Base			7.5	0.75	1.0-2.0	5,12,880	1.75	2.20	124.83
SP4-150TWC-M3	Base			5	0.5	1.5-2.5	9,70,682	3.05	2.50	159.08
SP4-60TWC-M4	Base			12.5	1.25	2.5-5.0	9,66,652	2.65	2.80	68.82
SP4-60TWCW-M5	Weld	350	900	15	1.5	5.0-7.5	10,86,367	3.00	2.85	77.06
SP4-90TWCW-M6	Weld			15	1.5	5.0-10.0	17,03,671	3.65	2.30	108.09
SP4-150TWCW-M7	Weld			10	1	5.0-10.0	20,23,897	2.90	2.55	161.52
SP4-120TWCW-M8	Weld			14	1.4	10	6,44,846	3.10	2.95	126.24

2.8 Summary

A periodically calibrated apparatus for measurement of load, displacement and crack length have been used in the present study. The yield strength and ultimate tensile strength values are average for three tests. The notch tensile strength values are an average of two to three tests. The CT specimens are fabricated as per ASTM E1820, and the experiment *J*-R curve results are from a single specimen test. However, for some weld specimens, the tests were repeated, and both test results have been presented. Base and weld pipe with various sizes of circumferential through wall crack has been tested for generating pipe *J*-R curves as per the test procedures established in the literature.

Chapter 3: Fracture Behavior of 316LN Stainless Steel

3.1 Introduction

Type 316LN stainless steel is low strength, high hardening and high toughness material used in thermal and nuclear power plants. Elastic-plastic crack initiation parameters, like initiation toughness (J_i) and crack tip opening displacement (CTOD), are the essential inputs for elastic-plastic analysis of components and to predict the onset of crack initiation in stress raisers due to gross and local structural discontinuities. The geometrical or material structural discontinuities affect the stress or strain distribution across the entire wall thickness over a region of significant size. Often, the constraint levels seen by the cracks in components are lower than those in the laboratory specimens tested as per standards. Also, the tests are conducted on specimens with sharp cracks. But in the actual components, the stress concentrations may be less severe compared to sharp crack, for example, blunt notches, nozzle to cylinder junction, shell to head junction, fillets, T-joints, etc. The point of local instability leading to critical event of crack initiation cannot be directly detected from experimental load-displacement data. However, the corresponding CTOD can be calculated by measurement of stretch zone width (SZW), which develops owing to crack blunting process. The determination of crack J_i in terms of SZW is considered to give the most accurate value of initiation fracture toughness [34, 35]. Further, the SZW based J_i values are found to be not influenced by constraint level over a range of stress triaxiality [36, 37]. Hence, the fracture parameters corresponding to the critical value of SZW are transferable to components. This chapter includes the attempts made towards the prediction of crack initiation fracture parameters based on critical strain at a characteristic distance and energy based crack growth parameter for 316LN SS based on the coupled experimental-numerical analysis.

3.2 Crack Initiation Criterion

3.2.1 Critical Strain and Characteristic Distance

The most popular approach adopted for prediction of ductile crack initiation is based on a critical strain (ε_c) which should be exceeded over a characteristic distance (l_c) from the crack tip. The choice of the appropriate ε_c and l_c are important. For example, Ritchie and Thompson [38] used a ε_c based on fracture strain and mean spacing of the void-nucleating particles for l_c in hardening ductile alloys. The 316LN SS used in the present study is nuclear grade steel with low inclusion content. The material is tested in the solution annealed condition and is practically free of precipitates. In this, planar slip is predominant, especially at ambient to intermediate temperatures. Therefore, the mechanism considered here is the linking up of grain boundary voids (that form due to slip band impingement) through the void sheets (formed by slip band intersection). Therefore, for the FEM analysis, it is appropriate to consider l_c= 2 x grain size (d_g). It is analogous to the postulation of Ritchie et al. [39] for cleavage cracking associated with grain boundary particles, where l_c= 2$d_g$which has been further validated experimentally from microstructural and fractographic observations. It needs to be appreciated that d_g does not possess a unique value due to inherent heterogeneity. Generally, this shows a statistical distribution. The grain size measurement has been discussed in Chapter-2, and the average grain size is 82 μm. The standard deviation for grain size measurement is 9 microns. Hence, the corresponding maximum grain size is 91 μm and the minimum grain size is 73 μm. Based on average grain size, the characteristic distance l_c is taken as 164 μm in the present investigation. A typical true stress-strain curve up to fracture shows a large area under the curve from necking to fracture, indicating a high energy density. However, since the volume of material associated with that necked region is very small, only a small amount of global energy is absorbed in this region, compared to the energy absorbed through uniform straining in the entire gage length. This is also evident from the fact that typical force-displacement plots show a sudden drop after necking. Therefore, the true uniform strain (i.e., the strain at the onset of necking) is taken as the critical strain (ε_c) in the present study.

3.2.2 Equivalent Plastic Strain as Damage Accumulation Parameter

The equivalent plastic strain (ε_{pe}) is a cumulative scalar strain quantity available in FEM software such as ABAQUS, ANSYS etc. that takes into account the entire deformation history. The driving mechanism for plastic distortion at the crack tip is the transformation of remotely applied displacement loading into plastic work; ε_{pe} is intrinsically a better indicator of the material condition than any instantaneous stress measure. Accumulated ε_{pe} defined as:

$$\varepsilon_{pe} = \sum_{i=1}^{n} \Delta\, \varepsilon_{pe,i} \tag{3.1}$$

where n is the number of strain increments, $\Delta\varepsilon_{pe,i}$ is the i^{th} increment of equivalent plastic strain that depends on the chosen material model. For classical metal (Mises) plasticity

$$\Delta\varepsilon_{pe,i} = \sqrt{\frac{2}{3}\varepsilon^{pl}\colon \varepsilon^{pl}} \tag{3.2}$$

where ε^{pl} is plastic strain increment. Since the von-Mises stress satisfies the property that two stress states with equal distortion energy have equal von-Mises stress under any loading conditions, the ε_{pe} cumulatively combines the strain state/history into a meaningful value for comparative purposes. Hence, the equivalent plastic strain (ε_{pe}) has been chosen as the strain measure of damage.

3.3 FE Analysis

The component thickness and type of loading in practical applications rarely meet the plane strain condition and mode-I type of loading. However, it can be considered that plane strain (PE) and plane stress (PS) analysis of components for a postulated crack gives lower and upper limits of the component behaviour. 2D FE analysis of components geometry with PE and PS elements require less effort and computational time compared to 3D FE analysis, which is tedious, especially for component level analysis. Considering these common practical issues, 2D FE analysis was carried out in ABAQUS. A rate-independent, J_2 (isotropic hardening) incremental plasticity theory based constitutive model is assumed. Although for monotonic loading conditions, deformation and incremental plasticity theories coincide; Kim et al. [40] have observed J estimates based on incremental plasticity approach are in close agreement with experimental values compared to deformation plasticity approach. Hence, the incremental plasticity approach using true stress-strain data for 316LN SS shown in Fig. 3.1 is adopted.

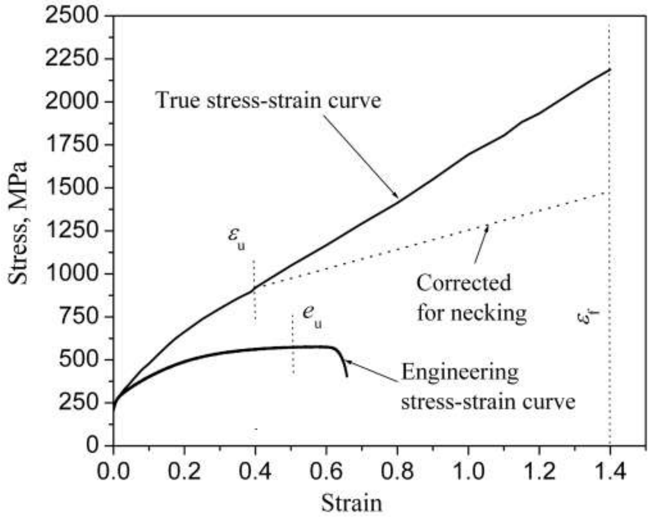

Fig. 3.1 Stress vs strain curve for 316LN SS

3.3.1 FE Mesh Model and Boundary Conditions

Although sharp cracks resulting from fatigue or stress corrosion cracking pose greater danger for component fracture, more and more engineering problems require the evaluation of failure loads and deformation for structures containing only blunt stress concentrators. In the present study, a blunt notch is considered and analysis is limited to CT specimen with blunt notch root radius of 0.15 mm, and varying crack depths (*a/W*= 0.4, 0.5, 0.6 and 0.7) subjected to mode I loading. A full size 2D FE mesh using CPE8/CPS8 elements was constructed, as shown in Fig. 3.2(a) to extract contour *J*-integral values. The crack tip is meshed using eight-noded quadratic elements of size ~8 microns along the crack surface and 20 microns in the radial direction. A typical focused mesh (schematic) is shown in Fig. 3.2(b) with l_c highlighted. In the FEM model, the loading pins are modeled as rigid bodies. The specimen loading is simulated by applying displacement to the pins with all other motions of the pins restrained. *J*-integral is defined in terms of the energy release rate associated with fictitious small crack advance, Δa. To get the large deformation *J*-contour integral, the crack details like crack front node set, singularity and virtual crack extension direction are specified. The blunt notch root surface is chosen as the crack front region. The virtual crack extension direction is defined along the crack. It implies that the stress and strain fields at crack tip do not change.

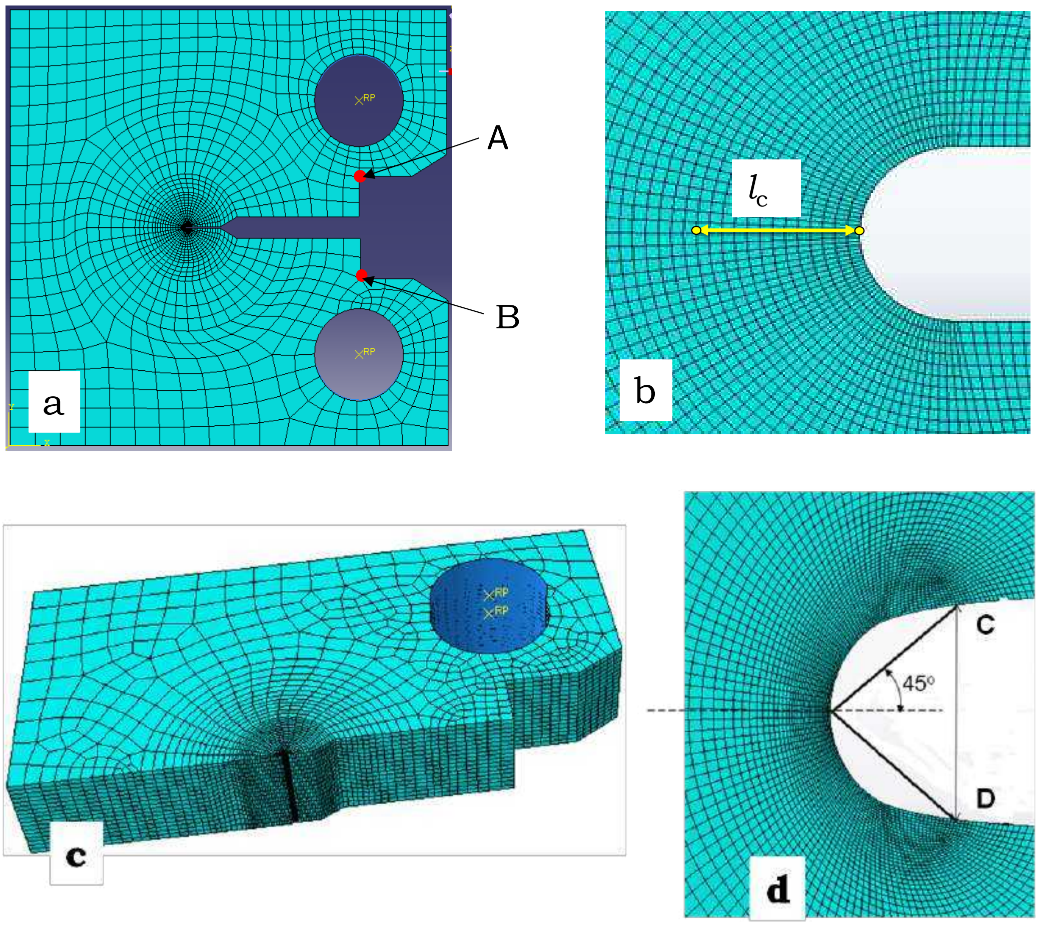

Fig. 3.2 Details of FEM mesh (a) CT mesh pattern for extraction of contour *J*-integral (b) Focused mesh at notch tip (c) 3D model and (d) CTOD measurement

3.3.2 FEM Simulations

A number of PE and PS simulations are carried out in ABAQUS for a blunt notch of varying crack depths (*a/W* =0.4, 0.5, 0.6 and 0.7) up to a rigid body pin displacement of 3 mm on each side. In general, the conditions ahead of crack tip are neither plane stress nor plane strain but are 3D. Therefore, a representative 3D FE analysis on quarter model of CT specimen shown in Fig. 3.2(c) with a/W=0.5 and thickness of 20 mm was carried out. The load-displacement results of 3D FEM analysis closely match with the average of PE and PS analysis results for 20 mm thick CT specimen. Also, it has been reported that averaging the results of the PE and PS conditions match with experimental results for steels with 20-25 mm thick CT specimen with reasonable accuracy [41, 42]. All the results reported in this chapter are average of PE and PS conditions unless otherwise specified.

3.3.3 Crack Initiation Parameters

The equivalent plastic strain (ε_{pe}) is considered as critical strain, and its critical value is taken as 0.44, which is the uniform strain (ε_u) in a uniaxial tensile test. The ε_{pe} at a node closest to l_c= 164 microns (Fig. 3.2(b)) is monitored as a function of increasing load line displacement (LLD), which is nothing but increase in the distance measured between two nodes A, B as highlighted in Fig. 3.2(a). The LLD corresponding to ε_{pe} reaching ε_c is taken as the LLD_i, and the values for different a/W values are presented in Table 3.1. The LLD_i increases with increasing a/W ratios for both PE and PS conditions. However, the LLD_i for a/W=0.5 in PE stress state drops.

Table 3.1 Estimated LLD_i and SZW_i under PE and PS conditions and their average values

a/W	PE		PS		Average of PE and PS	
	LLD_i (mm)	SZW_i (μm)	LLD_i (mm)	SZW_i (μm)	LLD_i (mm)	SZW_i (μm)
0.4	2.09	258	1.97	303	2.03	281
0.5	1.83	243	2.32	317	2.08	280
0.6	2.33	243	2.96	342	2.64	293
0.7	3.38	251	4.06	311	3.72	281

This could be due to equal in size of crack depth and ligament depth which leads to high triaxiality state of stress at the notch tip. Further at a distance l_c from notch tip, there is a compressive stress field arising due to ligament yielding and the interaction between tensile and compressive stress field causes the equivalent plastic strain to reach 0.44 for a smaller LLD. The variation on SZW obtained under PE and PS conditions for various *a/W* ratios is attributed to mesh size and identification of node close to l_c distance from notch tip. Considering a semicircular crack blunting in the present study, the stretch zone width, SZW_i, is taken as half of $CTOD_i$ corresponding to LLD_i. The schematic representation of SZW measurement is shown in Fig. 3.2(d). The predicted SZW_i values are shown in Table 3.1. Now, two estimates of J_i may be made; (i) using the SZW_i in the blunting equation and (ii) *J*-contour integral values corresponding to LLD_i. These are discussed in the following sections.

3.3.3 (a) J_i based on Predicted SZW_i (J_{SZWi})

The apparent crack extension associated with stretch zone width formation is considered equivalent to half of the CTOD; hence it can be related to J by the following equation [43, 44].

$$J_{SZWi} = m \,.\sigma_{yt} \,. (2SZW_i) \tag{3.3}$$

where m is the constraint factor which depends on the work hardening exponent (n), σ_{yt} is the average of yield strength and ultimate tensile strength (412 MPa for 316LN SS). The applicability of this method depends on the choice of m and the stress measure. Mills [43] has studied the effect of 'm' in the estimation of fracture toughness from *J*-R curve for low strength, high strain hardening materials ($0.26<n<0.39$) and found that choosing theoretical value (m=1) leads to an overestimation of fracture toughness. He observed that $1<m<1.7$ lead to conservative estimation of fracture toughness. The value

m differs widely, and particularly for high strain-hardening material, the dispersion is very significant. However, ASTM prescribes a blunting line slope based on an m value of 1.0 for stress measure, σ_{yt} and for highly work hardening materials. It is recommended that a higher value may be used, provided it is justified by the experimental data [32]. In a rigorous estimation for different engineering materials, Suresh et al. [45] have shown that the actual values of m lie in between 1.1 to 1.4 for material with $0<n<0.5$. Hence, the m has been chosen to be 1.25 for high hardening materials like 316LN SS having $n\approx0.4$. The J_i values calculated based on Eq. [3.2] designated as J_{SZWi} for different a/W ratios are given in Table 3.2.

3.3.3 (b) J_i based on Domain Integral at Critical LLD

The J-contour integral values are obtained for the FE domain contours around the crack tip as typically shown in Fig. 3.2(a). It is observed that the J values saturate, i.e., become path independent beyond a certain number of contours. Saturated J-contour values reached in far field remote from crack tip have been chosen as the valid J for a given LLD.

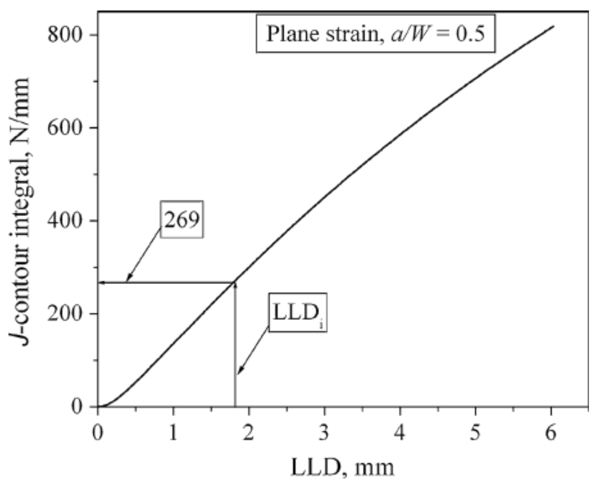

Fig. 3.3 Typical plot showing the variation of elastic-plastic J-contour integral with LLD

J-contour integral values vs LLD for *a/W*= 0.5 is shown in Fig. 3.3. The J_i values are determined as the *J*-domain integral values corresponding to the LLD_i designated as J_{LLDi}, which is a remotely measured displacement (loading-pin); this value is compared with analytically calculated J_{SZWi} where SZW value is from FEM simulation. Hence J_{LLDi} value is fully from FEM simulations, and J_{SZWi} is based on FEM simulated SZW and crack tip constraint parameter "m". A close agreement between these values validates the FEM procedures adopted for initiation toughness estimates in the present study. The results for different *a/W* ratios are given in Table 3.2.

Table 3.2 FEM predicted and experimental J_i for 316LNSS material

a/W	FEM predicted		Experimental	
	J_{SZWi} (N/mm)	J_{LLDi} (N/mm)	J_{SZexp} (N/mm)	$J_{Ic(0.2)}$ (N/mm)
0.4	289	295	~270	~640
0.5	288	275		
0.6	301	286		
0.7	289	292		

3.4 Crack Growth Criterion

3.4.1 Continuum Parameters for Crack Growth

Using conventional J_2 plasticity theory, damage growth law has been proposed as a function of two continuum parameters (i) equivalent plastic strain, ε_{pe} and (ii) stress triaxiality, φ, i.e., (σ_m/σ_{eq}) [46]:

$$\varphi = \frac{\frac{(\sigma_1 + \sigma_2 + \sigma_3)}{3}}{\sqrt{\frac{1}{2}[(\sigma_1 - \sigma_2)^2 + (\sigma_2 - \sigma_3)^2 + (\sigma_3 - \sigma_1)^2}} \tag{3.4}$$

where σ_1, σ_2 and σ_3 are principal stresses.

The equivalent plastic strain in von-Mises yield surface, ε_{pe} is related to uni-axial tensile plastic strain ε^{pl}as:

$$\varepsilon_{pe} = \int_{t=o}^{t} \dot{\varepsilon}_{pe}\, dt = \varepsilon^{pl} \text{ (at failure, it is } \varepsilon_c) \tag{3.5}$$

However, the material experience damage under plastic deformation, which is accelerated when conditions of multi-axial stress state exist. The ε_{pe} to fracture under a wide range of triaxiality for ductile material has been studied by Baoet al. [47] and from fracture locus curve, the fracture strain for a given state of stress is related to fracture strain in uni-axial tension ($\sigma_1 = \sigma_2 = 0$) by

General failure strain (ε_f)= uni-axial tensile failure strain (ε_c)$/\varphi$

Therefore, a material point is considered to be fully damaged when the equivalent plastic strain at that point reaches a critical plastic strain (ε_c).

3.4.2 Far Field J-contour Integral for Large Plastic Deformation

Beyond crack initiation, considering a sharp crack as a limiting case of the notch (root radius, ρ–> 0) and the crack growth to be *J*-controlled, the elastic unloading and non-proportional plastic loading regions must be embedded within the zone of *J*-dominance. The elastic unloading behind the tip of growing crack and non-proportional plastic loading beyond the region of *J* dominance violate the assumptions of deformation plasticity material model (eqn.1.3) and single parameter description. When there is extensive plasticity, the measured material resistance is no longer uniquely characterized by *J*; the single-parameter fracture mechanics formulation breaks down as discussed in Chapter-1. The stress state analysis ahead of a crack in Hutchinson [48] shows that as the strain hardening parameter (*n*) increases, there is very rapid rise ofφ which can elevate the flow stress with increasing strain. In the case of low yield stress and high strain hardening material like 316LN SS, the rise in φ due to material hardening effect is more severe than the geometrical effect on the near-tip fields [49]. Thus, a single-parameter fracture mechanics formulation may be approximately valid even in the presence of significant plasticity.

3.4.3 Development of Damage Function for Crack Growth

Based on CTOD for crack initiation and CTOD crack growth criteria available in ABAQUS, crack growth simulation has been carried out to trace load vs displacement response of 316LN SS CT specimen with *a/W*= 0.55. The variation of ε_{pe} and φ ahead of a growing crack which closely traces the load vs displacement response is shown in Fig. 3.4. From the plot, it is inferred that a 20% increase on ε_u as plastic strain to fracture (ε_{pe}= ε_c) is able to provide a close prediction of load vs displacement response. The increase on ε_u equal to ε_c is consistent with the difference between the global (engineering) uniform and fracture strain values of the uniaxial tensile test, as shown in Fig. 3.1. Hence the damage function for crack growth beyond crack initiation in 316LN SS is defined as:

$$D = (\varepsilon_{pe}/\ 1.2\ \varepsilon_u)\ \mathrm{x}\varphi \qquad (3.6)$$

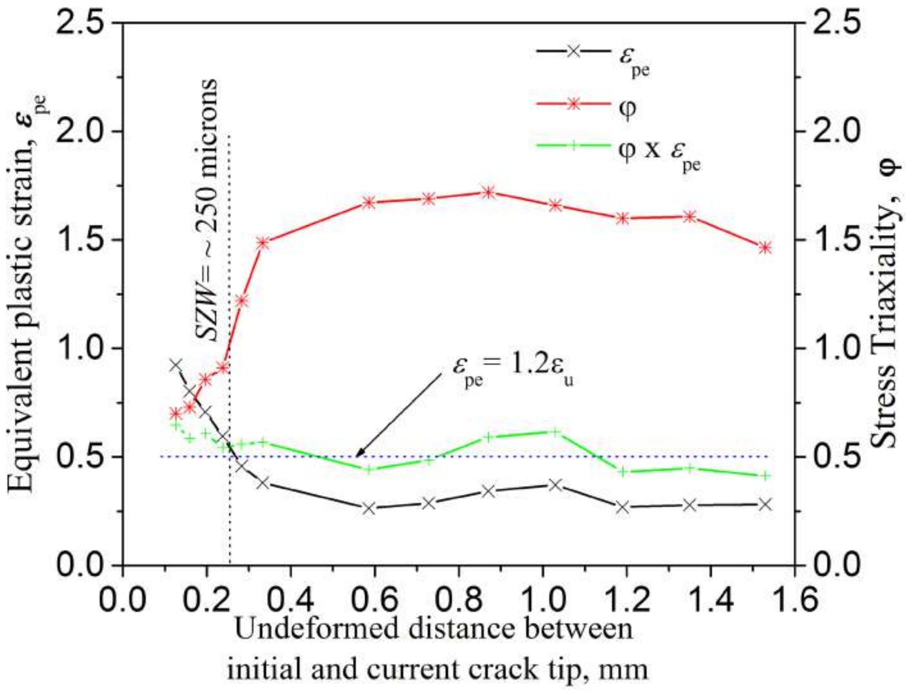

Fig. 3.4 Variation of ε_{pe} and φ ahead of a growing crack

It is observed that ε_{pe} decreases and φ increases till near the critical SZW for crack initiation, beyond this, the values are nearly constant, and the average φ is 1.5. The estimated φ level closely agree with higher (maximum) φ level of a notched tensile bar and lower (minimum) φ level of CT geometry loaded under plane strain condition [50]. This indicates that a growing crack tip in CT geometry undergoes a large deformation in the case of low yield stress material like 316LN SS. Further, in stable crack growth regime, a damage variable as a linear function of ε and φ adequately describes the crack growth. The *far field* J-integral values for a growing crack vs incremental crack extension (δa) including SZW (~250 μm) is shown in Fig. 3.5 along with the experimental J-δa curve. The difference between the estimated and experimental J-integral values is ~ 14% in the initial regime. It drops gradually with further crack extension. The variation could be due to (i) uneven crack extension through the thickness of the specimen as a result of crack blunting and subsequent variation in φ (ii) Simplification of the crack front as a straight one, (iii) Error in crack growth measurement by DCPD technique.

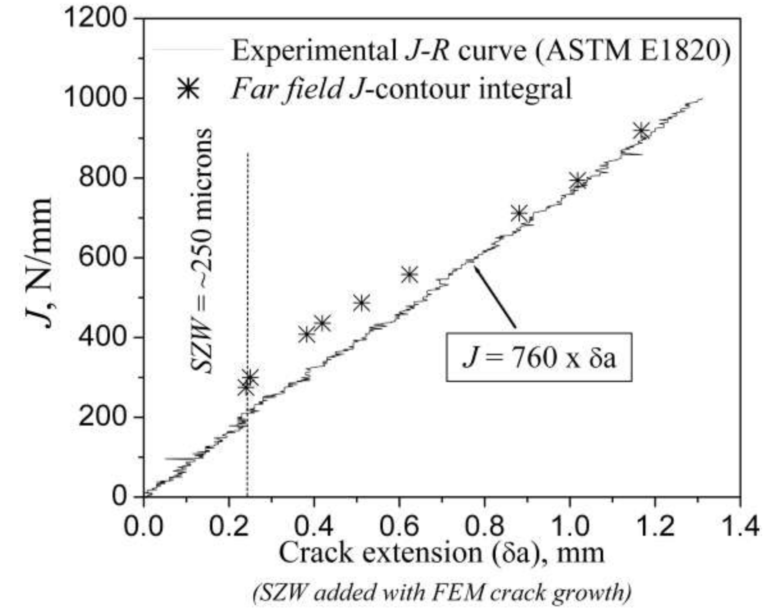

Fig. 3.5 *Far field* *J*-integral and experimental *J-R*-curve (*a/W* = 0.55)

3.5 X-FEM Crack Growth Simulations

In the previous sections, it has been established that a single fracture parameter, i.e. *far field* *J*-integral is able to represent the crack growth resistance of 316LN SS material. This is supported by continuum damage parameters evaluated using standard FEM analysis. Further crack growth simulations for CT specimens with various *a*/W ratios are carried out using X-FEM due to the difficulties with FEM. The difficulties in FEM for crack growth analysis and merits of X-FEM over FEM are discussed in Chapter-1. The stress or strain based crack initiation and energy based crack evolution parameters are the inputs to material model for X-FEM simulations with ABAQUS. In this study, stress (maximum principal) based crack initiation and energy based growth have been adopted. The estimated φlevel using FEM for *a*/W = 0.55 closely agrees with those for notched tensile bar and the CT geometry loaded under plane strain condition [50]. Hence the stress estimate corresponding to the fracture load from a conventional tensile test with Bridgman correction for necking induced triaxiality for 316LN SS is 1500 MPa (shown in Fig. 3.1). This value has been taken as maximum principal stress to fracture. The crack evolution energy of a material is independent of φ level [51]. Therefore, the crack driving force or energy release rate estimate beyond crack blunting, i.e. in the stable crack extension regime of the material *J*-R has been taken as the damage evolution parameter (J_{mat} = 760 N/mm)as shown in Fig. 3.5.

A typical 2D mesh for CT geometry discretized using 2339 numbers of CPE4 type elements, and boundary conditions are shown in Fig. 3.6. Time taken to complete the solution for Intel core 2GB RAM computer is 616 seconds. In a similar way, the mesh models have been created for various *a/W* ratios. A geometric line is inserted to define initial crack. The crack growth analysis was carried out for specimens with *a/W* = 0.39, 0.55, 0.64 and 0.72 using the above criteria.

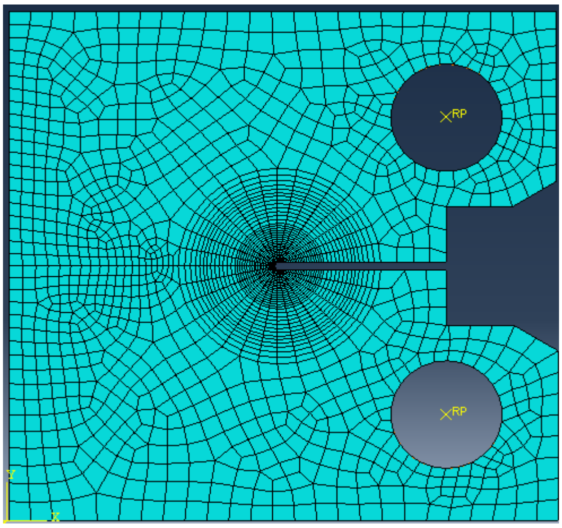

Fig. 3.6 XFEM mesh model for crack growth simulation

3.6 Verification of FEM/X-FEM Prediction with Experiments

3.6.1 Crack Blunting Analysis

In order to verify the validity of the proposed local damage approach with ε_u as ε_{pe} and two grain diameter as l_c, the FEM results have been compared with the experimental results. The Load vs.LLD plots obtained from the tests for a/W= 0.5 and 0.6 are presented in Fig. 3.7 as solid lines. The dashed lines correspond to the predicted values (average of PE and PS stress state results) from FEM simulations.

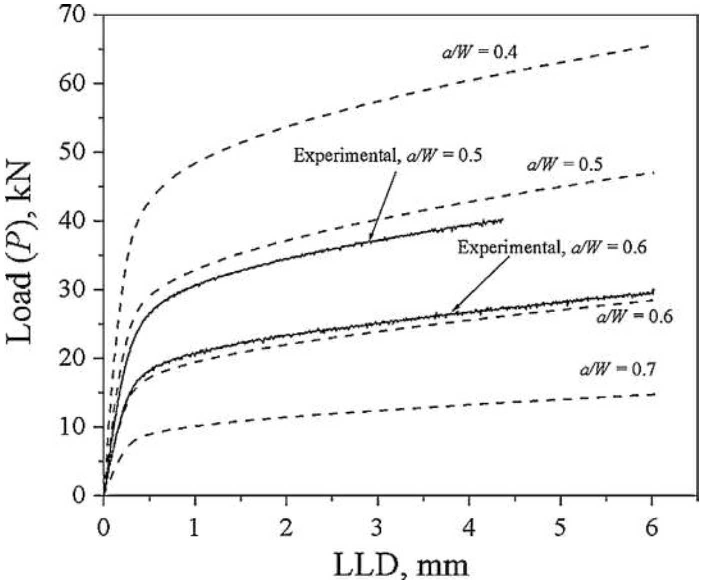

Fig. 3.7 FEM predicted and experimental load vs LLD plots

The simulated load-LLD plots are in good agreement with the experimental results. However, there is a marginal overestimation for a/W= 0.5 and underestimation for a/W= 0.6; this could be due averaging of PE and PS stress state results. Hence, it may be concluded that FEM simulation using conventional tensile test data reasonably represents the flow behavior of 316LN SS in mode-I loading for CT specimens and predicts the stretch zone formation.

3.6.2 Crack Growth Analysis

The load-displacement data extracted from X-FEM simulations using the proposed fracture criteria are compared with experimental results of CT specimens with a/W= 0.39, 0.55, 0.64 and 0.72 (shown in Fig. 3.8). It is observed that the deviations in the predicted load values from the experimental data are within 6% for specimens with a/W= 0.39, 0.55, 0.64, while for a/W= 0.72, it is 17%. The high deviation from experimental for *a/W*= 0.72 could be due to averaging of PE and PS stress state results and severe influence of compressive stresses on growing crack. Hence it may be concluded that a linear damage function and a *far field J*-integral are able to describe the crack growth in 316LN SS material beyond crack initiation.

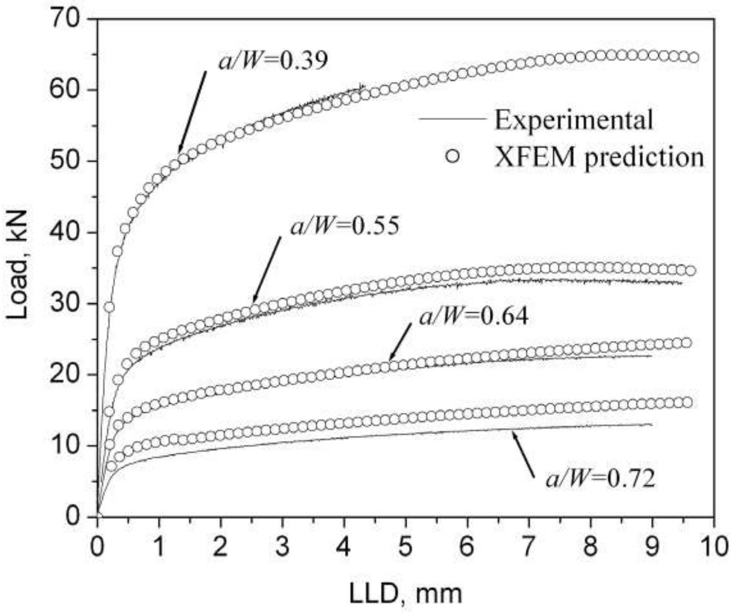

Fig. 3.8 Experimental and XFEM predicted load-displacement responses

3.7 Stretch Zone Width Measurements and J_i

Scheme of SZW measurements and SEM study are described in Fig. 3.9(a)-(c). The SZW values were obtained using a travelling type optical microscope and averaged based on 9-point average method proposed for crack length measurement in ASTM-E1820. The estimated average SZW was 280 μm. For local assessment of SZW and to present the featureless zone of the fracture surface, SEM study has been carried out on fracture surface. The fracture surface was oriented perpendicular to the electron beam in SEM, and the stretch zone width measurements were made over a specimen width of ~15 mm in the mid-region ignoring ~0.5 mm on edges. The average SZW for blunt notch was measured as 420 (Fig. 3.9(b)). Based on the correction method proposed by Srinivas et al. [52] and as per the scheme of measurement shown in Fig. 3.9(a), the estimated SZW_i was 270 μm. The SEM images shown in Fig. 3.9 are relatively from mid-regions of the specimen. Further, SZW measurement has been carried out on the CT specimen with sharp crack (after fatigue pre-cracking). It was measured as 280 μm (shown in Fig. 3.9(c)) and in agreement with the corrected value from blunt notched specimens. The J_i calculated as per Eq. 3.3 for SZW_i (= 280 μm) is 288.4 N/mm.

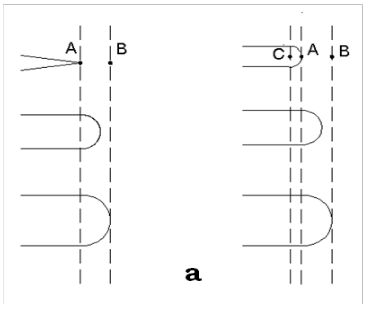

Sharp notch Blunt notch

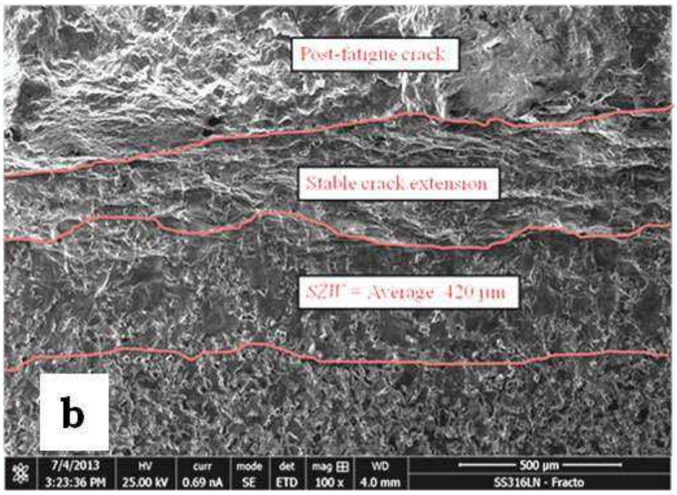

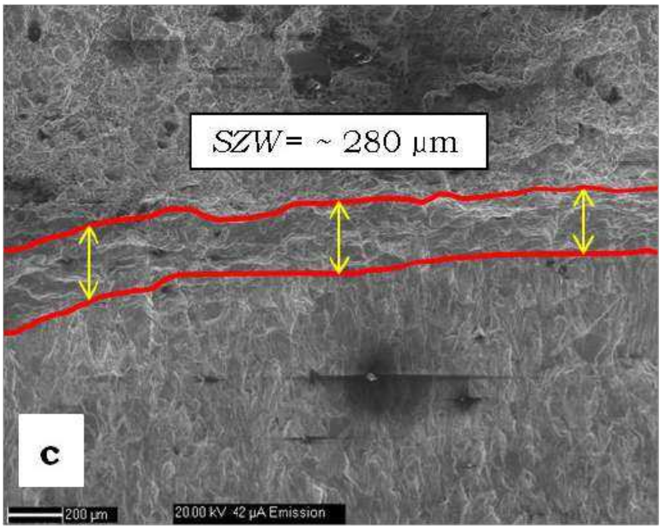

Fig. 3.9 Scheme of SZW measurement and SEM study on fracture morphology
(a) Scheme of SZW measurement for tested CT specimen
[SZW_i (AB) = Measured SZW (CB) Initial notch radius(CA)]
(b) SZW in a specimen with blunt notch of 0.15 mm root radius
(c) SZW in fatigue pre-cracked specimen

The *J*-R curve obtained from experiments on pre-cracked CT specimen (a/W= 0.55) with side groove is shown in Fig. 3.10. The apparent crack extension for blunt crack (a/W= 0.5) specimen is 0.8 mm. The stable crack extension on fatigue pre-cracked (a/W= 0.55) specimen is 2.55 mm. The J_i based on the experimentally determined SZW_i from the same *J*-R curve (270 N/mm) is very close to those reported here. The ductile fracture toughness, $J_{Ic(0.2)}$ estimated by taking m = 1.25 is 640 N/mm. The initiation toughness, i.e. J_{Ic} obtained as per ASTM E1820 is significantly higher than J_i.

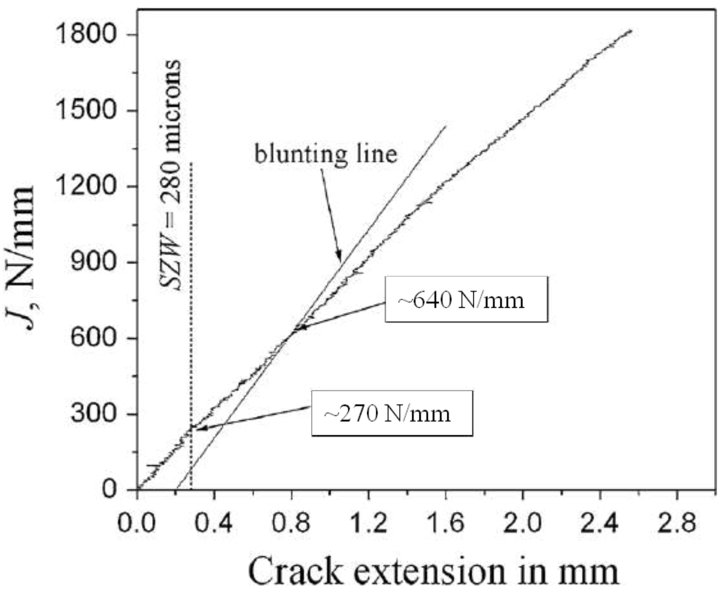

Fig. 3.10 *J*-R curve obtained from a pre-cracked CT specimen

3.8 Discussion

Based on coupled finite element analysis and experimental fracture studies using CT specimens, crack initiation criterion for 316LN SS has been established. This is validated through fracture parameters like SZW, CTOD, *J*, and LLD. The justification for the damage criterion in the first assumption, viz. crack initiation event corresponds to a critical value (ε_c) of ε_{pe} at l_c, which can be set as ε_u, has already been discussed in section 3.2. However, the choice of l_c= 2 x d_g needs further clarification.

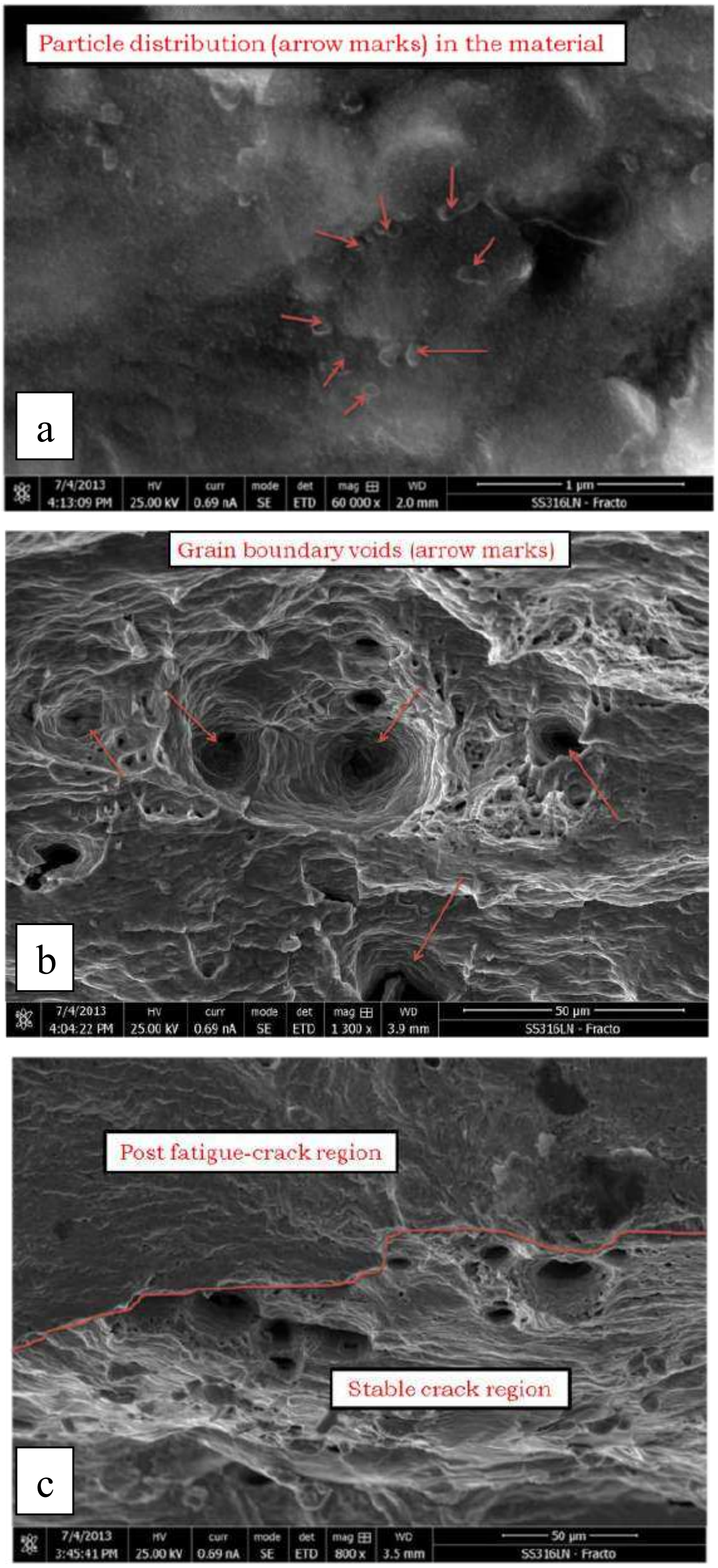

Fig. 3.11(a-c) SEM study on blunt notch fracture surface (a) Particles size and its distribution (b) Demarcation between crack extension and post-fatigue crack regions (c)Dimples on the fracture surface.

In the case of materials containing particles such as inclusions or precipitates, the voids nucleate ahead of the crack tip and grow further till they coalesce with each other and/or with the crack tip. A detailed SEM study on blunt notch fracture surface has been carried out to assess the particles distribution and dimple formation as described in Fig. 3.11(a-c). The size of the particles is less than 0.2 μm, as seen in Fig. 3.11(a). The nucleation of void occurs either due to decohesion of second-phase particles and inclusions or slip band intersections and impingements on grain boundary. A large area of final fracture surface has been examined; it shows that the majority of the dimples are free from particles, large size voids and also very small voids. The material used in the present study is a clean nuclear grade 316LN SS. In this type of steel, planar slip is predominant, especially at room temperatures. The slip bands blocked at the grain boundaries makes the voids to grow along grain boundaries. It is clear from the fractographs that large voids (on the grain boundaries) link through fine intragranular dimples (associated with slip band intersections) as seen in Fig. 3.11(c). Hence it is postulated that the crack initiation could be due to void nucleation at the intersection of shear bands and impingements on grain boundary. The subsequent growth of this void and fracture could be (i) by the process of alternating slips along these shear bands with inter-void necking and intervoid shearing, (ii) nucleation and coalescence of new voids in the sheared ligament between pre-existing voids leading to the coalescence of the pre-existing large voids *i.e.* void sheeting. The dimples, as seen in representative SEM images (Fig. 3.11(b) and (c)) do not show any particles associated with them. Thus, the crack initiation due to the presence of particles can be considered insignificant. In view of these, it is appropriate to assume a characteristic length l_c, which is linked with the grain size. The micro-mechanism of ductile fracture invoked in the study is verified with SEM study on SZW formation and fracture surface, the choice of $l_c = 2 \times d_{g\ appears}$ metallurgically meaningful and practically appropriate. As the void nucleation and growth is predominately along the grain boundary, it is necessary to have at least one grain boundary ahead of crack tip to cause necking instability between grains. The second assumption is semicircular blunting and 45° construction line from the plane of crack to determine the critical CTOD, as elaborated in Fig. 3.2(b). From slip line field theory, blunting with a smooth profile or with one or more vertices is possible as shown by Rice and Johnson [53] and also experimentally observed by McClintock et al. [54]. The most widely used definition of critical CTOD is that corresponding to 45°angle. Table 3.2 gives the comparison of J_i for the 316LN SS by FEM simulation and experiments. It may be observed that the FEM predicted J_i values are in close agreement with the experimentally obtained J_i value. Also, it is found that the $J_{Ic(0.2)}$ is higher than the J_i, which is consistent with the expected trend for a ductile material like 316LN SS. Thus, the local damage model based ε_{pe} at a characteristic distance l_c with the choice of critical values of these parameters adopted here is able to predict the crack initiation in 316LN SS.

3.9 Summary

- The ductile fracture in 316LN SS was found to be largely due to shear band intersection and impingement on grain boundaries rather than void nucleation at second phase particles in the material.
- The proposed local damage approach based on uniform strain, ε_u, and grain diameter of the 316LN SS material is able to predict the crack initiation

parameters under monotonic loading condition. The SZW formation being a deformation process, and in a practical sense, any sharp crack has a finite root radius, the approach proposed in the present study does work well.

- The crack blunting analysis further emphasizes that it is imperative to account for initial crack blunting for the correct prediction of crack growth behavior in the beginning part of stable crack growth through 316LN SS.
- The damage parameter and saturated *far field J*-integral for a growing crack have been obtained and validated with experimental results. A linear damage parameter in terms of stress triaxiality, equivalent plastic strain and uniform strain has been established. It has been shown that a single-parameter fracture mechanics approach considering saturated *far field J*-integral is able to describe crack growth through low strength and high hardening material, 316LN SS.
- A close agreement between predicted load-displacement results from X-FEM analysis with the experimental results implies that the damage initiation and evolution material parameters estimated for 316LN SS from conventional tensile test and fracture test are sufficient for X-FEM crack growth simulations.

Chapter 4: Fracture Behavior of Modified 9Cr-1Mo Steel

4.1 Introduction

It is well known that the deformation and fracture properties of ferritic steels are sensitive to temperature, strain rate, and stress triaxiality. The presence of a notch or stress raiser exhibits an increase in yield stress, a decrease in strain hardening exponent and change of fracture mode from ductile to brittle depending on temperature. Presently, Modified 9Cr–1Mo steel (P91) is widely used ferritic steel in a normalized and tempered condition for steam generator application in conventional and nuclear power plants. Transferable elastic-plastic fracture parameter is an essential input for integrity assessment, including leak-before-break (LBB) analysis of the steam generator. Physical metallurgy studies on Cr-Mo steel shows the presence of MX and $M_{23}C_6$ precipitates at all thermo-mechanical conditions [55]. Different microstructural parameters such as effective grain diameter, grain orientation, size, shape, and distribution of second phase particles play key roles in determining the deformation and fracture behavior of the material. The morphology, size and distribution of precipitates or particles also influence the fracture toughness [56, 57]. Ductile fracture in this material is due to coalescence of microscopic voids; generally, appear first at second phase particles due to cracking of the particles from the parent matrix under tensile stress [58]. The plastic strain and hydrostatic stress can cause the voids to grow and eventually coalesce. Crack initiation occurs at a critical value of the void fraction. The state of stress near particle is an important factor in determining crack initiation. As discussed in previous chapters, the growth of voids depends on the combined form of continuum parameters, i.e. stress triaxiality and incremental plastic strain at the void nucleating site. In this chapter, a damage potential symptomatic of void growth was estimated in a post-processing manner by incorporating Rice-Tracey model for crack initiation in P91 steel. Further, this damage potential (parameter) has been used to predict the crack initiation under a range of stress triaxiality conditions.

4.2 Crack Initiation Criterion

Extending the eqn. 1.7 for growth of initial void of radius R_0 to a critical void size in an elastic-plastic strain hardening material over a loading history and to trigger necking instabilities between the voids for coalescence has been defined as damage index (*DI*) in the present study, and it is given as:

$$DI = \int_0^{\varepsilon} \exp(1.5\varphi)\, d\varepsilon \qquad (4.1)$$

The crack initiation is said to occur when the value of *DI* reaches a critical value, and this is a material parameter. Dutta and Kushwaha [58] adopted Rice-Tracey cavity growth model to predict crack initiation in a compact tension specimen. They observed that the void growth is sensitive to mesh size and therefore proposed a modified approach by the integration of a cavity growth factor related to *J*-integral and yield stress of the material, and over a plastic zone. For P91 material, the *DI* is obtained by integrating over a characteristic length scale, which is evaluated from scanning electron microscopy (SEM) study on fracture surface and will be discussed later. The *DI* increases with an increase in material toughness and indicates a more ductile material. As described later, the critical value of damage index (DI_c) for P91 steel is determined by calibration of data from tests on notched bar specimen.

The coefficient 1.5 used in the Rice-Tracey expression (eqn. 4.1) represents the void coalescence process, and it is based on dilatational amplification of spherical void vs stress triaxiality for viscous plastic flow of the material. Other researchers have proposed different coefficients instead of 1.5 that might represent the coalescence process for different materials more accurately. For example, Johnson and Cook [59] have shown that a coefficient 2.12 works better than 1.5 to model fracture in 4340 low alloy steel. Hancock and Brown [60] reported a coefficient in the range of 1.1–2.3 for British steel (50D and 50D N.N). Dutta and Kushwaha [58] used coefficient 1.5 for ferritic steel SA338. Since the fracture mechanism and mechanical properties of SA 338 are similar to P91 steel, a coefficient of 1.5 is adopted in *DI* calibration.

4.3 Calibration of Rice-Tracey Model Parameters

4.3.1 Notch Specimen Analysis

The critical damage index for P91 material is obtained through coupled experiment and FE analysis of circumferentially U-notched tensile specimens, as shown in Fig. 2.8. The U-notched specimens having minimum cross-section diameter of 4mm (C1) and 6mm (C2) with 8mm smooth cylindrical diameter have been chosen for damage assessment at an intermediate range of stress triaxiality under tensile loading [61]. Digital image correlation technique is used for measurement of gauge displacement and strain-displacement fields. A single camera system, as shown in Fig. 2.2, is used to acquire the images of the specimen undergoing deformation in a synchronized way with load, time and stroke displacements. The images were analysed using commercial Vic-2D DIC software. The load vs time plot for C1 and C2 specimens are shown in Fig. 4.1. A nearly constant slope region followed by a sudden load drop is observed.

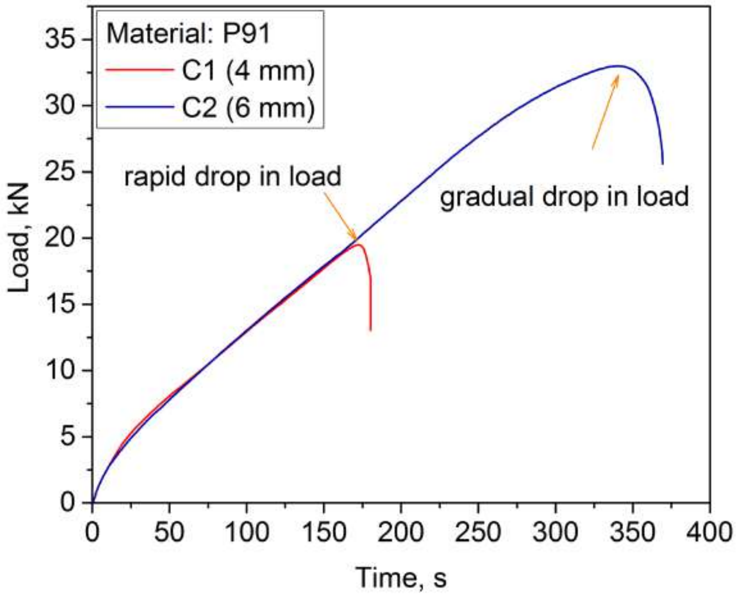

Fig. 4.1 Load vs time response for C1 & C2 specimens

In both C1 and C2 specimens, there was a sudden fall in load bearing capacity, and it is very sharp in the case of C1 specimen compared to C2 specimen. The response of C1 specimen indicates that the entire notched section is undergoing fracture process, and the micro-cracks initiated in the notch portion of the specimen lead to fracture and sudden drop in load.

4.3.2. SEM study

The fracture surface of the C1 specimens was examined by scanning electron microscopy (SEM) to identify the location of ductile fracture initiation and later to correlate with the stress triaxiality in the notch region of the specimen. A chain of SEM images obtained from middle to periphery of the fracture surface is shown in Fig 4.2. Ductile fracture initiates at a material point where the micro-void coalescence occurs; there are two distinct zones observed on the fracture surface: (1) micro-void coalescence (MVC) zone comprising of cup and cone portion of the fracture surface (centre portion, images C to H) and (2) shear lip zone (peripheral region, images A and

B). Though MVC is the dominant mechanism, a sharp shear lip is produced because of the 45° inclination of void coalescence that begins at the specimen centre.

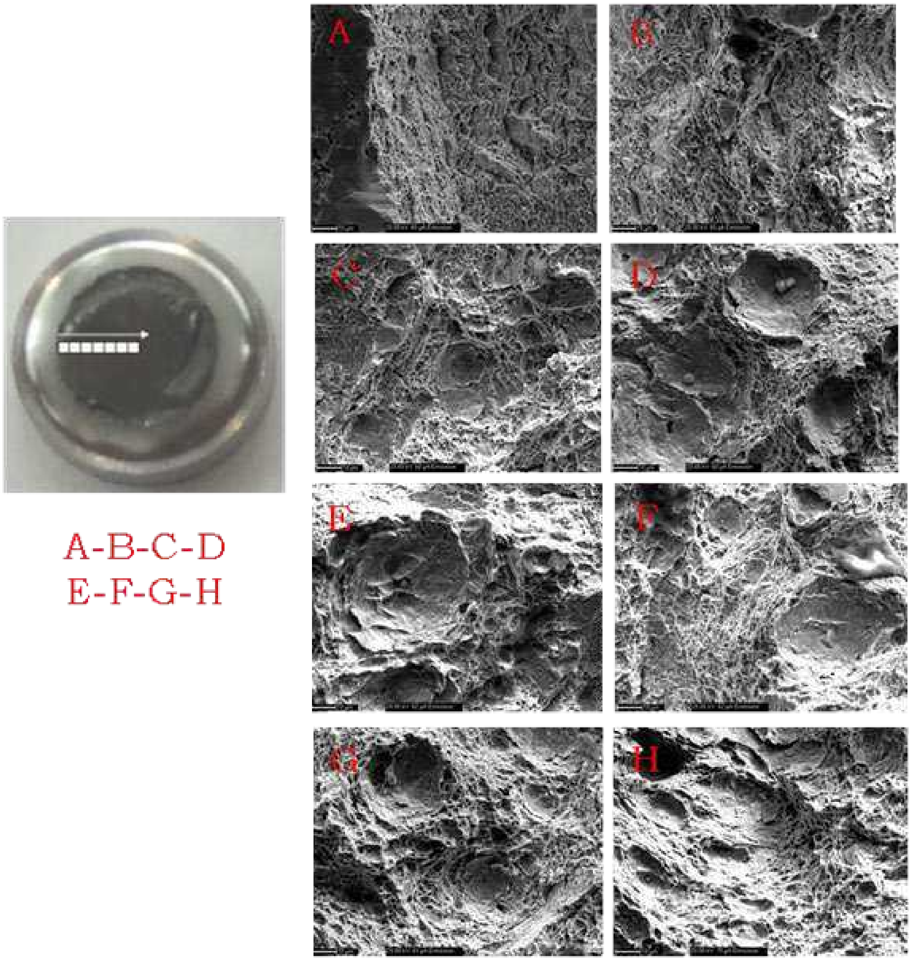

Fig. 4.2 SEM images of C1 specimen fracture morphology

From cup and cone fracture surface, it is observed that MVC zone spread to the entire notch volume, which led to symptomatic flat fracture as inferred from load vs time response (Fig. 4.1) with nearly constant slope followed by a sudden drop in global load. The SEM micrograph of C1 specimen shows that MVC zone exists over a large region and a small shear lip region all around. Therefore, the entire notch volume of C1 specimen could be considered as fracture process zone. The SEM study on C2 fracture surface reveals very small size dimples with concurrent shear lips. Further, a gradual deviation from the constant slope is observed in the load-time response, and there is a smooth transition in load response at fracture. These observations indicate a crack initiation followed by crack growth before complete fracture. Hence for Rice-Tracey model parameter calibration, C1 specimen alone considered.

4.3.3 FE simulations

Geometric and material non-linear FEM simulations have been carried out for tensile specimens. The cylindrical notched specimens are modeled using eight noded C3D8 brick elements. The true stress vs true plastic strain data for P91 material

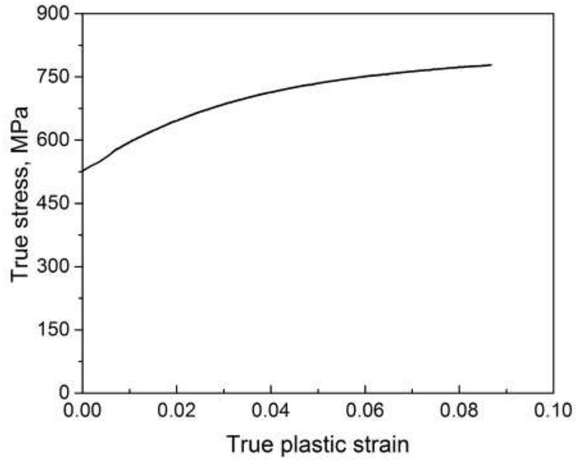

Fig. 4.3 True stress and true plastic strain data for P91 steel

obtained from uniaxial tensile test was used, and it is shown in Fig. 4.3. The stress triaxiality and equivalent plastic strain vs displacement for different nodes located in the notch region of C1 specimen are shown in Fig. 4.4(a) and (b). The specimen being cylindrical and symmetric on two mutually perpendicular planes, nodes on one-quarter portion of planar notch region (as highlighted in Fig. 4.5) have been considered for Rice-Tracey damage parameter assessment. Due to elastic deformation, there is an initial steep rise in stress triaxiality followed by drop due to the transition from elastic to plastic deformation. Again there is a rise due to hardening behavior of the material, and further gradual reduction is due to the spreading of the plastic zone to a large area.

The peak stress triaxiality at different nodes has varied from 0.77 to 1.6. In elastic regime at low strains, the stress triaxiality reaches a maximum near the notch root because of discontinuity in stress flow lines caused by the notch, the shape of the notch changes with an increase in strain, thereby changing the stress concentration.

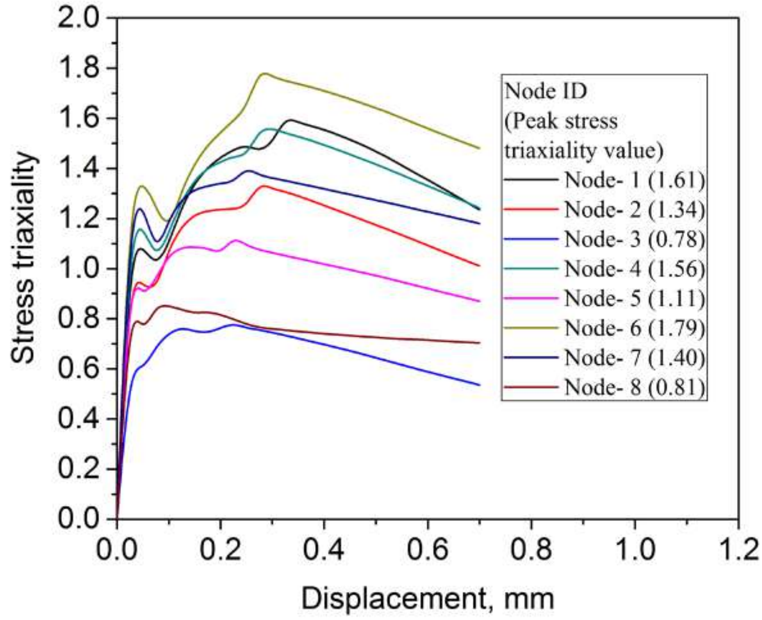

Fig. 4.4(a) Stress triaxiality vs displacement

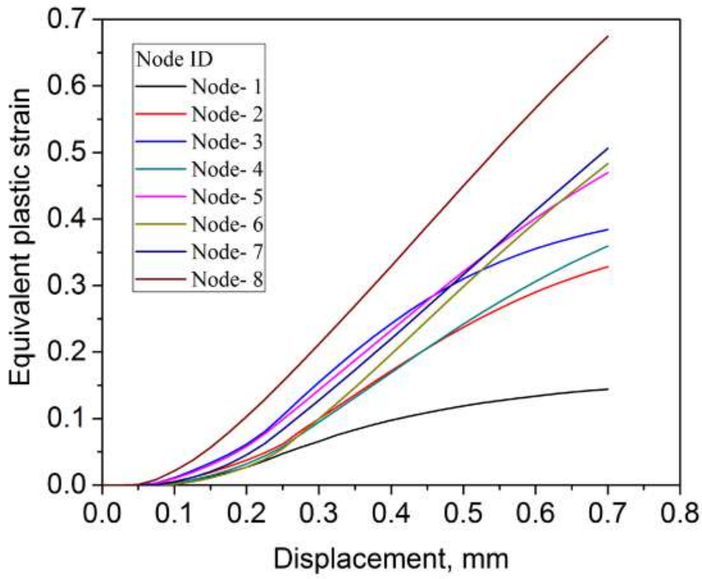

Fig. 4.4(b) Equivalent plastic strain vs displacement

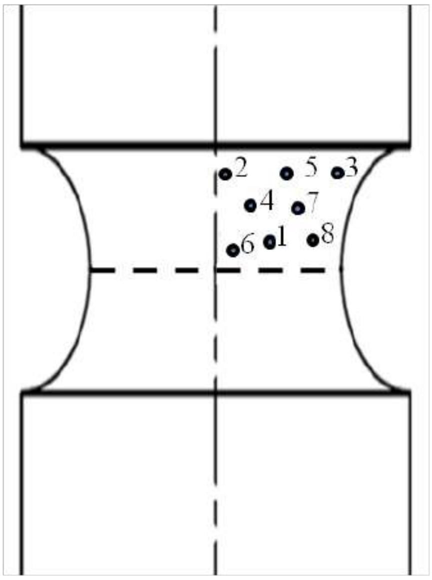

Fig. 4.5 Location of nodes considered for damage assessment in the notch region (highlighted)

Hence the triaxiality profile of the notch evolves with strains and geometry. In the notch region, there is high stress triaxiality towards periphery at low strain level and towards the centre of the specimen at high strain level. SEM study on fracture surface as shown in Fig. 4.2 has revealed that the size of voids close to the centre of the specimen is large and sizes decrease towards the outer. This agrees well with the stress triaxiality distribution, as discussed earlier with FE analysis. Since the sizes of the micro-voids are different from the centre of the specimen to periphery, the characteristic length based on inter-void distance may not be an appropriate parameter for fracture prediction in P91 steel.

4.4 Rice-Tracey Model Calibration

The Rice-Tracey model is calibrated to obtain material specific damage parameter for P91 steel. The fracture criterion needs to be satisfied over a characteristic volume often represented by the characteristic length of the material for crack initiation. In literature [5-7], the material specific fracture parameter has been assessed from coupled FE analysis and experimental results such as tensile tests and SEM study on the fracture surface. The characteristic length has been estimated by measuring (1) size of microvoid clusters [62, 63]; (2) average size of a single microvoid [64]; and (3) distance between nonmetallic inclusions in the metal [11]. The characteristic length needs to be known to calibrate the R-T parameter. Panontin and Sheppard [65] evaluated the characteristic length by FE analysis using the stress and strain distribution corresponding to a certain value of applied displacement at which the ductile fracture initiation was observed in the experiment. In the present study, the entire notch volume of the C1 specimen is considered as a characteristic volume. From the tested specimen, it is observed that the parallel (cylindrical) region of the specimen has not undergone any plastic deformation; the total work done on the specimen is limited to the notch region alone. Hence, the total experimental energy to fracture is equated to the area under the load-displacement curve of FEM simulation, as shown in Fig. 4.6.

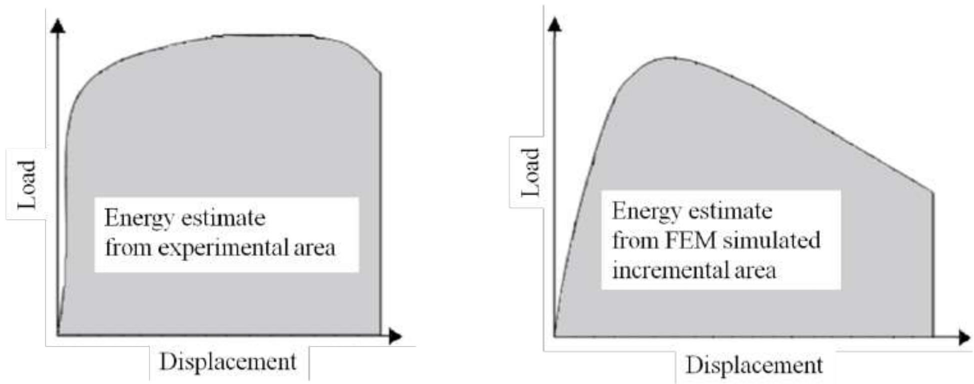

Fig. 4.6 Schematic representation of equivalent energy between experiment and elastic-plastic FEM simulation

The corresponding FE analysis displacement is taken as critical value for fracture initiation. The continuum parameters and resulting Rice-Tracey parameter for critical displacement are taken as critical damage parameters. As discussed in the earlier sections, MVC occurred in the entire notch volume; hence the notch volume is considered as the characteristic volume (undergoing fracture process) for fracture prediction. In order to make the Rice-Tracey parameter mesh independent, the Damage Index defined earlier has been integrated over characteristic volume and the critical Damage Index (DI_c) for P91 steel has been estimated as 0.32.

4.5 Validation of Rice-Tracey Model Damage Parameter

The damage index evaluated based on C1 specimen is applicable for a core volume ahead of the notch, which is undergoing plastic deformation. It is required to validate the applicability of the proposed characteristic volume. Sih et al. [66] proposed the concept of "core region" surrounding the crack tip. The continuum mechanics concept holds well up to a certain distance from crack tip leading to core region periphery. Further, Sih et al. suggested a local fracture criterion based on strain energy density (SED) factor; *S* is defined as the product of the SED by a characteristic distance from the point of singularity. Hence, the characteristic distance over which the fracture process takes place has been accounted. In the present study, the core region defined in the SED approach is adopted, and the stress state within the core region is obtained from FE simulations. The damage index is calculated over the core region, and when it reaches the critical value, the crack is considered to be initiated.

The flat tensile dog-bone specimens with central U-notch of radius 0.5 mm at a different angle (30° [F30], 45°[F45], 60°[F60] and 90°[F90]) to loading axis are tested. The initial ligament distance 3 mm from notch tip is kept the same on both edges for all the specimens. Typical specimen geometry is shown in (Fig. 2.8). To ensure a range of stress triaxiality at the notch tip, the notch axis of the specimens is oriented to loading direction at different angles to cause a mixed mode (Mode-I and Mode-II) loading conditions.

The experimental load-displacement of F30, F45, F60 and F90 specimens and predicted crack initiation location is shown in Fig. 4.7. Berto et al. [67] proposed the SED method for sharp and blunt notches; it condenses together the advantages of energy based criterion with material-dependent structural volume as defined through the characteristic length. Further, Berto et al. proposed various control volumes based on the type of stress raisers like sharp crack, sharp V-notch, blunt V-notch etc. under Mode-I or mixed mode (I+II) loading. In planar problems, the critical control volume becomes a circular sector or crescent shape with radial thickness w_0. The expressions for w_0 surrounding the crack tip under plane strain and plane stress conditions are given as;

$$w_0 = \frac{(1+\nu)(5-8\nu)}{4\pi}\left(\frac{K_{IC}}{\sigma_t}\right)^2 \text{plane strain}$$

$$w_0 = \frac{(5-3\nu)}{4\pi}\left(\frac{K_{IC}}{\sigma_t}\right)^2 \text{plane stress}$$

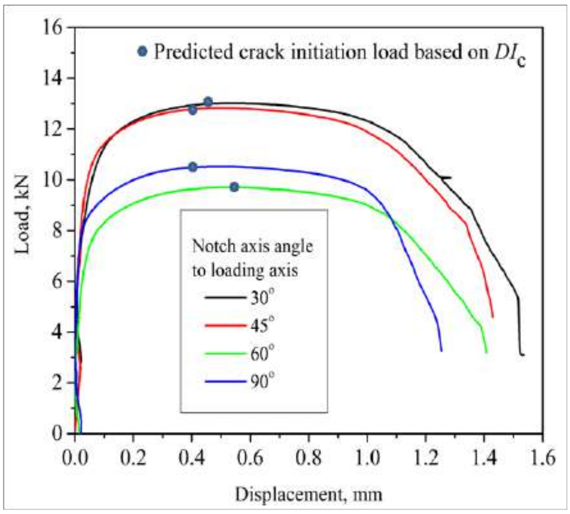

Fig. 4.7 Predicted apparent initiation load for various specimen

For 2D blunt notches, the crescent shape control area with w_0 being its maximum width as measured along the notch bisector line has been considered (Fig. 4.8). For mixed-mode loading, the control area is rigidly rotated with respect to the notch bisector and centered on the point where the principal stress reaches its maximum value. The control area for a U-shaped notch both under mode-I loading and mixed-mode loading are reproduced in Fig. 4.8(a) and Fig. 4.8(b) respectively.

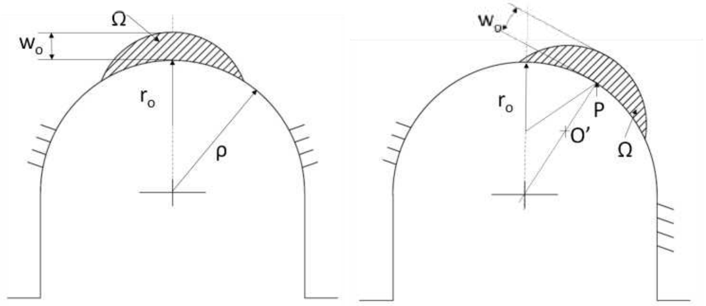

Fig. 4.8 Critical volume for U-notch (a) under mode-I and (b) under mixed mode [figure from ref:9]

In the present study, the control area of elliptical shape with the aspect ratio of 2 is considered, the length of the semi-minor axis is the distance between notch edge along specimen thickness (on undeformed mesh) and the point of maximum principal stress along notch bi-sector at mid of specimen thickness. The damage index is calculated by integrating Rice-Tracey parameters for nodes over an elliptical planar area where the maximum principal stresses are acting. From FE simulations for specimens F30, F45, F60 and F90, the damage index values are estimated over the area, as highlighted in Fig. 4.9. As this value reaches the critical value (DI_c) of 0.32, the crack is considered to be initiated. The damage index calculated for increasing applied displacement for all specimens are shown in Fig. 4.10 and the critical applied displacement value corresponding to DI_c for F30, F45, F60 & F90 specimens are shown in Fig. 4.10.

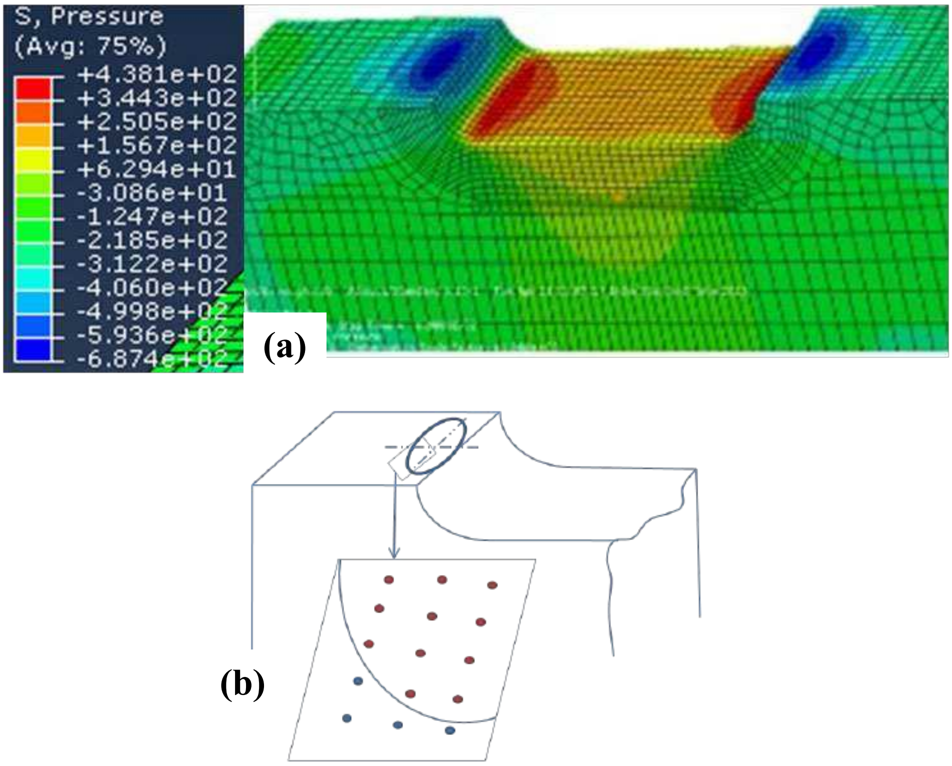

Fig. 4.9 Damage index estimation (a) FEM mesh model(b) Evaluation *DI* over an elliptical area as highlighted (red color)

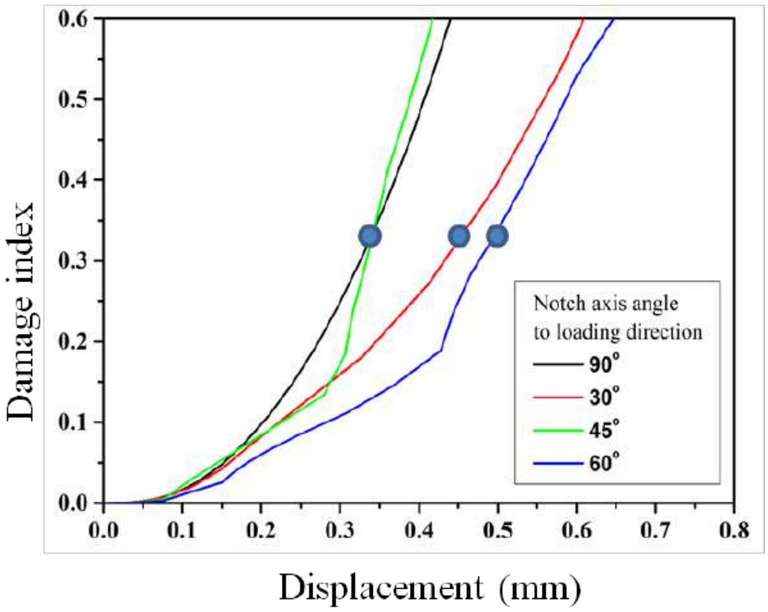

Fig. 4.10 Critical Damage Index and corresponding displacement

4.6 Summary

Considering a sharp fall in the load-time response of C1 specimen and based on SEM study on the fracture surface, the C1 specimen's notch geometry has been found to be an appropriate one for evaluating Rice-Tracey damage parameter. The mesh dependency of the Rice-Tracey damage parameter was overcome by integrating over the damage process zone (notch cross-section of the specimen). The validation of critical damage index for a range of stress triaxiality (using notched flat tensile specimens) shows the predictive strength of Rice-Tracey model for P91 steel.

The scanning electron microscopy study on the fracture surface of all central notched specimens F30, F45, F60 and F90 have been carried out. From fractography shown in Fig. 4.11, it could be observed that the shape of the voids for F30, F45, F60 and F90 are nearly circular. The coalescence of voids could be due to the combined effect of hydrostatic and shear stresses. On increasing the applied load and onset of plastic deformation causes the voids to grow due to the hydrostatic component of the stress state. While the deviatoric component of stress state causes the evolution of void shape and the rupture of unstable ligament formed between the voids, this leads to a decrease in load. Hence the final void shape and size seen on fracture surface could be related to load and dominant component of stress acted during deformation. From the load-displacement plot, it is observed that the maximum load for F60 is the lowest among all other specimens. This could be due to predominant shear stresses on the fracture plane. An example DIC colour contour frame belongs to F90 specimen is shown in Fig. 4.12. The load values corresponding to the apparent crack initiation identified from DIC frames for all the specimens are in agreement with those from FEM prediction.

	Middle	Edge
F30	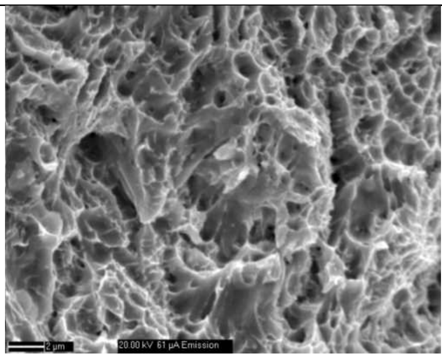	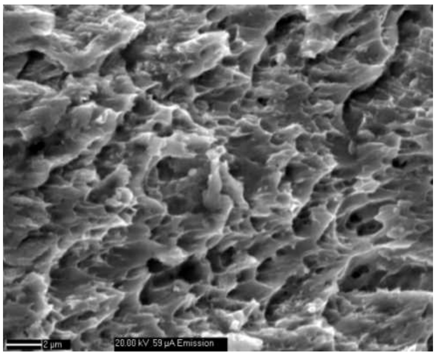
F45	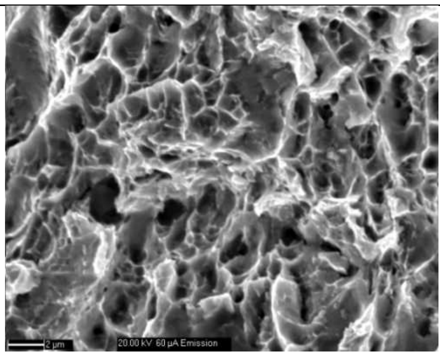	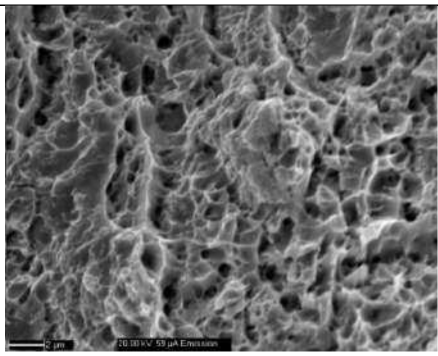
F60	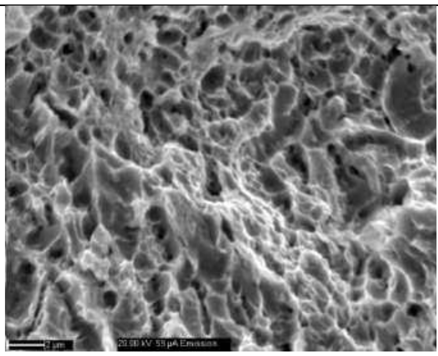	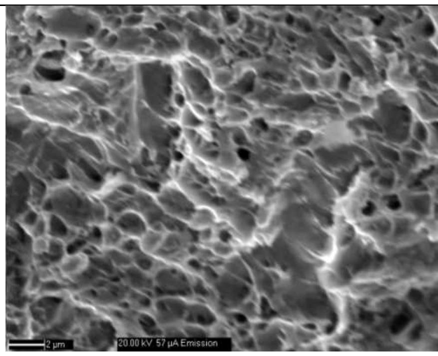
F90	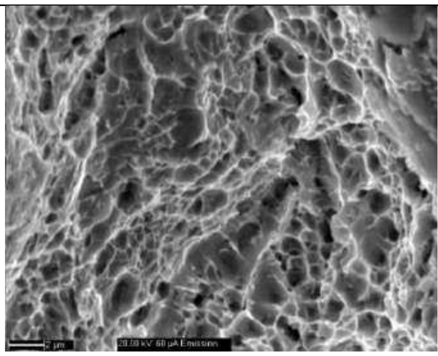	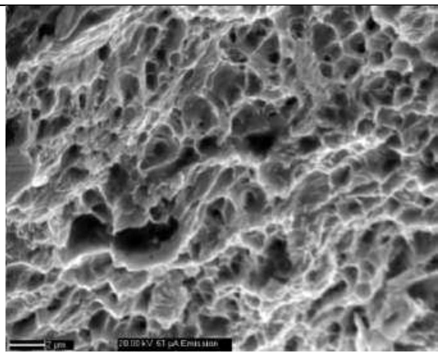

Fig. 4.11 SEM Fractography of F30, F45, F60 and F90 specimens

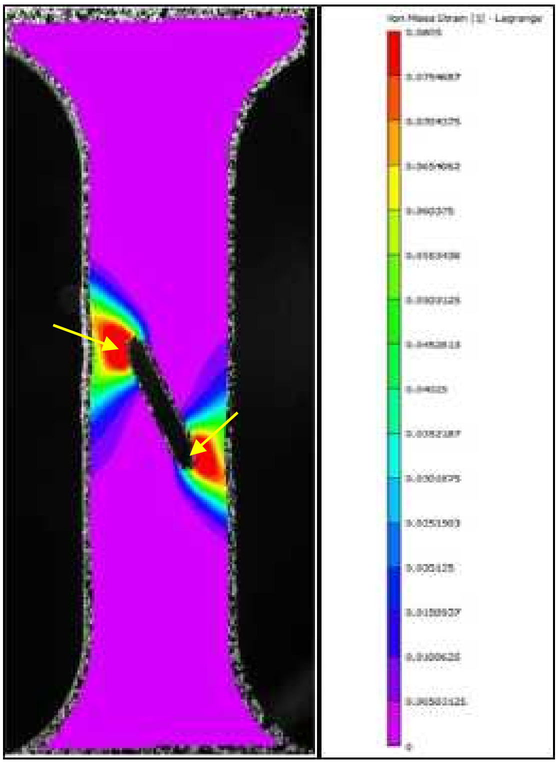

Fig. 4.12 Apparent crack initiation location highlighted in DIC image (F90 specimen)

4.7 Conclusion

The following important conclusions may be drawn based on the experimental and FE analysis presented in this chapter.

1) The Rice-Tracy damage parameter for crack initiation in P91 steel has been evaluated from a notched specimen, which has fractured by crack initiation without any crack propagation.

(2) From SEM analysis, a qualitative correlation between void size and stress triaxiality was observed. The stress triaxiality is large at centre of fracture process zone and decreases towards the periphery.

(3) The critical damage parameter obtained by integrating the continuum parameters over the fracture process zone was able to overcome FEM mesh size dependence for fracture prediction.

(4) The damage parameter evaluated from the coupled experimental-numerical analysis was able to provide crack initiation load prediction for a range of stress triaxiality.

Chapter 5: Fracture Behavior of Similar and Dissimilar Welds

5.1 Introduction

Weldments generally contain flaws or crack-like defects due to large plastic strains in each weld pass induced by weld thermal cycles under restraints. The steep temperature gradient experienced in the weld metal and adjacent base metal lead to the formation of heat affected zone (HAZ). The micro-structural variation and various interfaces across the weld and base will induce complex stress fields under structural loadings. For structural integrity assessment, the fracture behaviour of the welds in terms of *J*-R curve or crack tip opening displacement (CTOD) is an essential input. The well-known ductile fracture parameter, i.e., elastic plastic fracture toughness (J_{Ic}) for weld metal, is generally assessed as per ASTM E1820 [32] by ensuring a propagating crack in the weld metal. The weld width is chosen such that the plastic deformation (plastic zone) does not cut across the interfaces. The material property does not vary in the direction of crack propagation; the effective crack driving force, *G* (for linear or non-linear solids) is measured in terms of near-tip *J*-integral. For a two-dimensional crack, in the *x-z* plane with crack front parallel to the *z*-axis, the *J*-integral is given by

$$J = \int_{\Gamma} wdy - T_i \frac{\partial u_i}{\partial x} ds \tag{5.1}$$

where *w*- loading work per unit volume for elastic bodies or strain energy density, *ds* - length increment along the contour Γ that encloses the crack tip with small plastic zone, T_i – outward traction vector components of traction vector on *ds*, u_i- displacement vector at *ds*. The *J*-integral is divided into two components; linear elastic (J_{el}) and non-linear elastic (J_{pl}) representing the plastic deformation at the crack tip. In order to account for the plastic deformation at the crack tip and relate it to energy release obtained from experimental load-displacement data, a geometry dependent plastic multiplier (η) is used.

$$J = J_{el} + J_{pl} \tag{5.2}$$

$$J_{el} = \frac{K^2(1-\upsilon^2)}{E}, \quad J_{pl} = \frac{\eta A_{pl}}{B_N b} \tag{5.3}$$

B_N – minimum thickness at root of the side grooves, K - Stress intensity factor, ν- Poisson's ratio, E - Young's modulus, η - geometry parameter for a material, derived based on limit load analysis using linear elastic material model, A_{pl} - area under the load-displacement curve obtained from the experiment, b-uncracked ligament length. The analytical solutions and the experimental procedure of ASTM E1820 [32] are further extended to the weld specimens provided (i) the plastic zone is small and well confined in the weld, (ii) the strength mismatch ratio, M<1.2 ($M = \sigma_w/\sigma_b$, where, σ_w and σ_b are yield strengths of the weld and base metals respectively). However, in the realistic scenario, the crack propagates seldom in weld metal alone. The growing crack is influenced by neighbouring material interfaces and heat affected zone (HAZ) and interact with interfaces and propagates across various regions of the weldment. The objective of the study presented in this chapter is to assess the fracture resistance of a propagating crack across the weld, base and their interfaces of similar and dissimilar weld joints.

5.2 Crack Propagation across 316LN SS Similar Welds

Historically, the interaction between crack and bi-material interfaces has been reported by Williams [68] and Rice [69]. Cracks parallel to the interface have been examined by Hutchinson and Suo [70]. The crack approaching the interface perpendicular or inclined has great significance in the integrity assessment of welded structures. The earliest work on perpendicular cracks has been analyzed by Zak and Williams [71]. It has been shown that the stress singularity at the tip of a crack perpendicular to an interface depends on the elastic properties mismatch. Later studies [72, 73] on elastic materials reveal that stress intensity decreases and reaches zero at the interface when a crack from weaker material approaches a stronger material through the bi-material interface. Similarly, when a crack in stronger material approaches a weaker material through the interface, the stress intensity factor reaches infinity due to singularity stress fields induced by the presence of a soft interface. Sugimura et al. [74] have studied the interaction between crack tip plastic zone with a bi-material interface and its effect on crack driving force. Wen-Hwa et al. [75] have studied the applicability of the J-integral for the crack in bi-materials. It is well known that J-integral for a crack in a body with a gradient in material properties is path-dependent. For a bi-material elastic body with a finite size, interlayer and elastic property mismatch, Kim et al. [76] have shown that there is a variation between crack tip J-integral, J_{tip} and remotely applied J-integral, J_{far} based on FE analysis. Further, they have used elastic-plastic FE analysis to quantify the plasticity mismatch on the crack driving force. They quantified the J_{tip} and compared it with imposed J_{far} for both the cases of stationary crack lying in plastically stronger and weaker material. They used finite size model with homogeneous as well as graded interfaces.

Here, the study on 316LN SS similar weld consists of coupled experimental work and FE simulations. In part (1), experiments have been conducted on three CT specimens of 316LN SS weld with the initial crack tip located in weld metal (CT-W), near to interface (CT-I) and in the base material (CT-B). The material *J*-R curves have been obtained with a modified elastic component, J_{el} based on instantaneous equivalent Young's modulus. In part (2), elastic-plastic FE analysis has been carried out for CT specimens with various stationary crack lengths lying perpendicular to the weldment. The *J*-integral incorporating the interface effect is estimated from FE simulations, and this is compared with material *J-R* curve.

5.3 Experimental Work

The CT specimens as per sketch in Fig.2.11 are extracted such that the crack planes are perpendicular to the interface. The notch was introduced by the electric discharge machining process. The specimens are fatigue cracked and fracture tested; Fig. 5.1 shows the photo images of tested CT specimens.

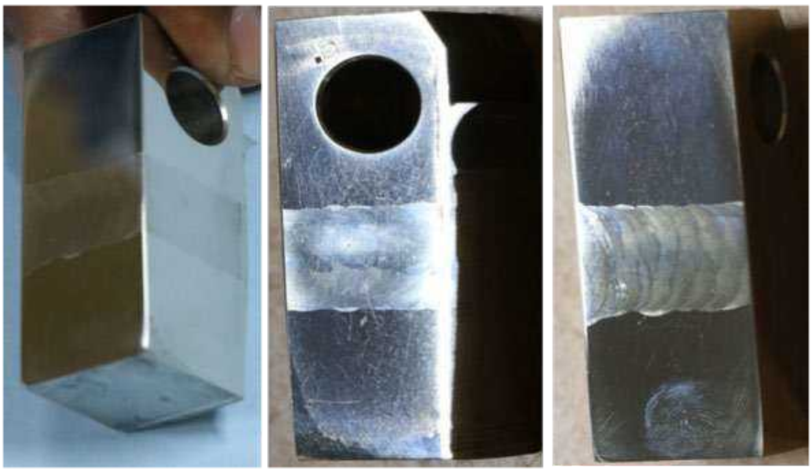

Fig. 5.1 Photo images showing weldment in CT specimen

5.3.1 Identification of Weld Interface and HAZ

HAZ in the weld is small and the formation of HAZ is due to increase in the size of 2 to 3 grains adjacent to fusion line and the microstructure is not too different from the base material. It causes complex stress-strain fields and a large degree of uncertainty on the mechanical/fracture behaviour. Due to its small dimension, it is not possible to characterize using standard mechanical tests. A close estimate of its size and mechanical behaviour is made using multiple micro-hardness measurements across the weldment. The Vicker's tester is often easier to use than other hardness testers since there is a less influence of indenter size on the estimation of mechanical strength. The indenter can be used for all materials irrespective of hardness profiles. Vickers hardness with a load of 100 g was obtained on CT specimen surface using ESE WAY model: EW-423 DAT micro-hardness tester. The presence of precipitates, grain boundaries and voids just below the indenter can cause variation in micro-hardness readings. To overcome this issue, three readings were taken along a straight line at each location, instead of a single reading, as per the pattern shown in Fig. 5.2. Minimum spacing of 50% higher than one average grain diameter (~85 μm) is maintained between measurement points to avoid the influence of plastic strain at neighboring indents. The hardness profile obtained across the weldment on specimen surface is shown in Fig. 5.3.

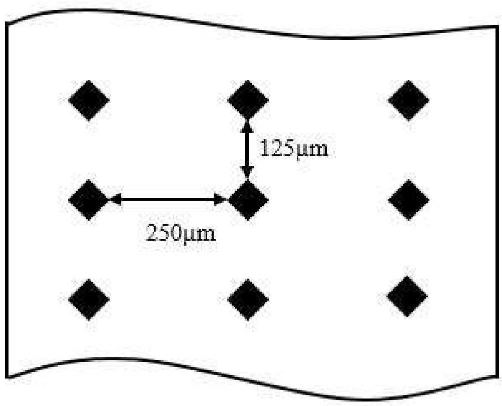

Fig. 5.2 Pattern adopted for hardness profile measurement

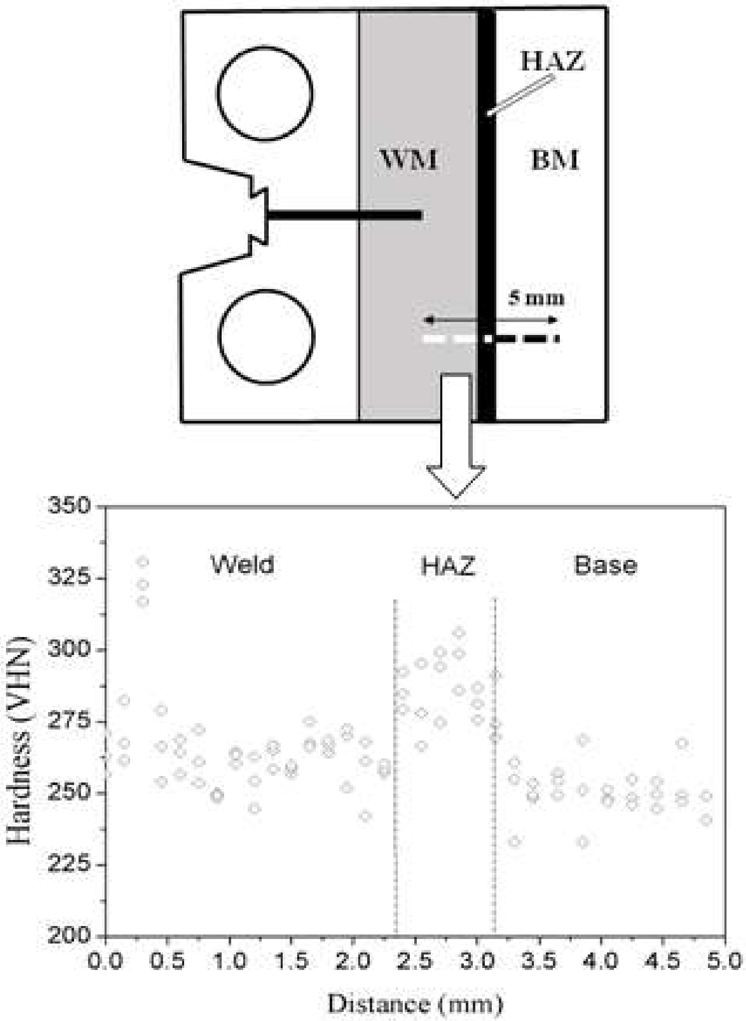

Fig. 5.3 Micro-hardness profile across the weldment

The average value of hardness for weld, HAZ and Base is 262±8.4, 284±12 and 250±8 respectively. The hardness of the HAZ region is higher than weld, and the weld is slightly higher than the base region. This is attributed to the repeated heating and cooling cycles in the HAZ region due to several weld passes. Further, the higher hardness of HAZ in spite of larger grain size is possibly due to the formation of fine precipitates during the heating and cooling cycles. The width of the HAZ is approximately 0.85mm. The yield stress (YS) and ultimate tensile strength (UTS) have been estimated from empirical correlation [77, 78] to use it as the material's data for FE analysis.

$$YS = \left(\frac{H}{3}\right)\left(\frac{1}{10}\right)^{n} \quad \text{(kgf/mm}^2\text{)} \tag{5.4}$$

$$UTS = \left(\frac{H}{2.9}\right)\left(\frac{n}{0.217}\right)^{n} \quad \text{(kgf/mm}^2\text{)} \tag{5.5}$$

where H is the Vickers hardness and n is the strain hardening coefficient of the material. The value for n = 0.32 at nominal (10^{-3} /s) strain rate has been used. The average value of YS and UTS estimated over HAZ region is 478 MPa and 1048 MPa respectively.

5.3.2 Derivation for Equivalent Young's Modulus

ASTM E1820 equations for fracture toughness evaluation are applicable only for homogeneous CT specimens and are extended to heterogeneous CT specimen with limited strength mismatch ratio. In this section, the necessary modifications on elastic solutions are introduced to estimate J_{el} for CT-W, CT-I and CT-B specimens. The effective height of CT specimen arm is smaller than initial crack depth, 25 mm (crack length to width (a/W)= 0.5) and it is limiting case of a double cantilever beam in opening mode. Thus, the shear deformation at crack tip region is suppressed. Further, the von-Mises contour plot from FE analysis on 316LN base-weld CT specimen as shown in Fig. 5.4 reveals that the stress level in arms of the specimen is only 8% of stress level surrounding the crack tip. Hence, in the present study, the Euler's elastic beam theory equations are applied to CT specimens to get equivalent Young's modulus considering the influence of strength mismatch ratio. The energy release rate in terms of instantaneous compliance (C_i) and instantaneous crack length (a_i) for a homogeneous specimen can be expressed as:

$$G = \frac{1}{2}P^2\frac{\delta C_i}{\delta a_i} = \frac{P^2 {a_i}^2}{EI} \tag{5.6}$$

For CT-W specimen configuration as shown in Fig. 2.10(b), the energy release rate is given by

$$G = \left[\frac{P^2 a_w^2}{E_w I} + \frac{P^2 \left(a_b + a_w\right)^2}{E_b I} - \frac{P^2 a_w^2}{E_b I}\right] \tag{5.7}$$

where E_b and E_w are Young's modulus of base and weld materials, a_b and a_w are crack depth in base and weld metal. For an equivalent homogeneous material, it is given by

$$G = \frac{P^2 {a_i}^2}{E_{eq} I} \tag{5.8}$$

Equating eqns. 5.7 and 5.8 we get

$$E_{eq} = {a_i}^2\left[\frac{a_w^2}{E_w} + \frac{(a_b + a_w)^2}{E_b} - \frac{a_w^2}{E_b}\right]^{-1} \tag{5.9}$$

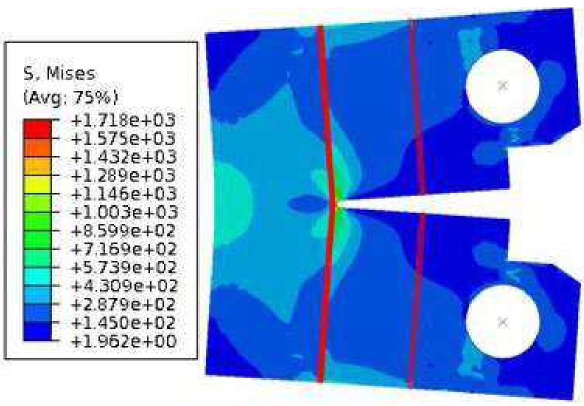

Fig. 5.4 von-Mises contour plot depicting stress distribution in the arm region of CT specimen

Similarly, the energy release rate for CT-I & CT-B (Fig. 2.11(c) & Fig. 2.11(d)) configurations based on equivalent Young's modulus is given by

$$E_{eq} = a_i^2 \left[\frac{a_{b2}^2}{E_b} + \frac{(a_{b2} + a_w)^2}{E_w} - \frac{a_{b2}^2}{E_w} + \frac{(a_b + a_w + a_{b2})^2}{E_b} - \frac{(a_{b2} + a_w)^2}{E_b} \right]^{-1} \tag{5.10}$$

5.3.3 Experimental Determination of J-Δa curve

Load vs load line displacement and load vs crack extension plot for all three specimens, viz., CT-W, CT-I and CT-B are shown in Fig. 5.5. For CT-W, the initial crack tip (a_0 = 25.85 mm) and its extension (Δa = 3.15 mm) are within the weld metal, and equivalent Young's modulus eqn. 5.6 is adopted to calculate J-Δa curve. Similarly, for CT-I specimen, the initial crack tip (a_0 = 27.45 mm) was kept near to the weld interface, and it has been extended to the base material region (Δa = 3.4mm). For CT-B specimen, the initial crack tip (a_0 = 29.94 mm) was kept beyond weld interface and its extension is in the base material (Δa = 3.82 mm), and the equivalent Young's modulus eqn. 5.7 is used in calculating J-Δa curve.

During fracture testing, the fatigue crack tip in sample undergoes crack blunting and leaves an imprint of the featureless region, i.e., stretch zone, before crack initiation, the width of which is referred to as SZW. During the blunting process, the DCPD values in Chapter 3. The procedure established in [33,79] for generating experimental J vs Δa curve is as follows: (i) J_{szw} in the blunting region is estimated by using the blunting line equation up to a crack length equal to the measured SZW. (ii) The nominal J value was calculated according to the basic procedure of ASTM E 1820. (iii) For all the data points corresponding to $J \leq J_{SZW}$, the crack lengths are estimated from the blunting equation. (iv) For all the points for which $J \geq J_{SZW}$, crack lengths are calculated from DCPD readings by linear interpolation between crack length = a_0 + SZW and final crack length, a_f.

The estimated J-Δa curves for CT-W, CT-I and CT-B specimens are shown in Fig. 5.6 (a, b & c). Beyond crack blunting, the tearing resistance multiplier (TR_M)

defined as ΔJ per 0.5 mm crack extension, estimated from *J*-R curve of CT-W, CT-I and CT-B specimens are 250, 135 and 128 N/mm respectively. The detailed description of tearing resistance across the weld metal has been given in a later section.

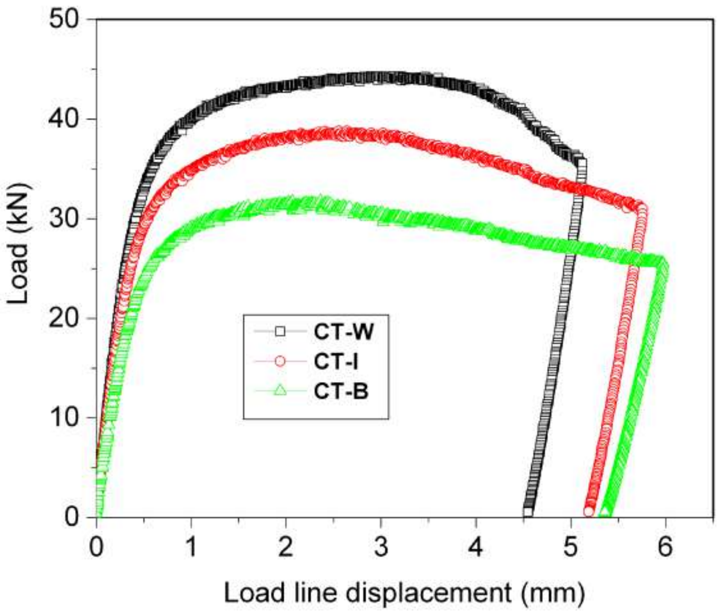

Fig. 5.5 Load vs LLD for CT-W, CT-I and CT-B specimens

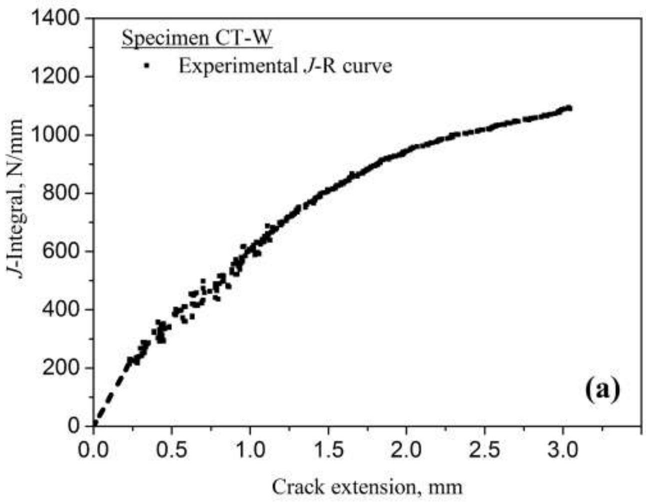

Fig. 5.6 *J*-integral vs crack extension (a) CT-W specimen

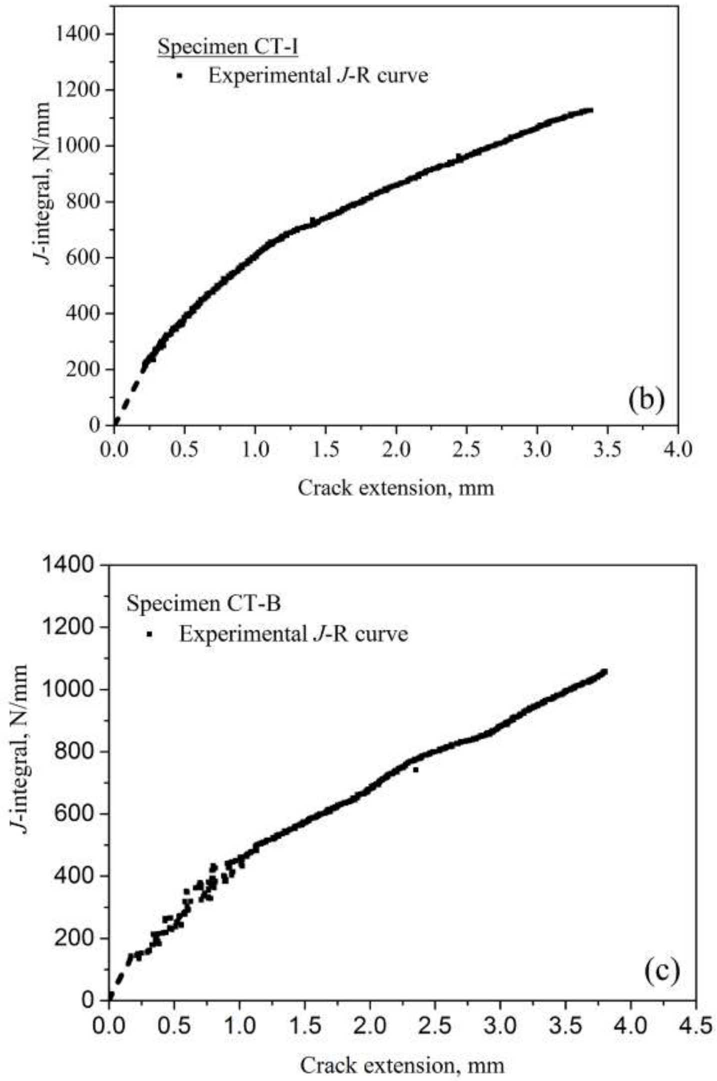

Fig. 5.6 *J*-integral vs crack extension (b) CT-I specimen (c) CT-B specimen

5.4 Elastic-plastic FEM simulation

5.4.1 J-integral for heterogeneous materials

J-integral for contour path, Γ (Fig. 5.7) enclosing the crack tip/singularity is path-independent for fracture analysis of homogeneous material. For defects in inhomogeneous material, i.e., the welded structure requires a correction term in *J*-integral to re-establish the path-independence. The contour Γ passing across strength interface boundaries includes an additional singularity of stresses and strains. Hence the J-integral for this Γ contour takes in to account the energy release rate associated with crack tip plus the energy absorbed due to the translation of interface boundary. The contour integral for the interface is calculated separately and added to crack tip J-integral. Analytically, the path independent J-integral with an interface is calculated as:

$$J = \int_{\Gamma} \left(wdy - T_i \frac{\partial u_i}{\partial x} ds \right) - \int_{pb} \left(wdy - T_i \frac{\partial u_i}{\partial x} ds \right) \tag{5.11}$$

Hereafter, it is referred to as *modified* J-integral. Kikuchi et al. [80] have carried out finite element analyses on welded CT specimens to quantify the effect of material inhomogeneities on J-integral. Kolednik et al. [81] have adopted FE analysis procedure to evaluate path-independent J-integral for bi-material interfaces. In the present study, FEM simulations have been carried out to calculate *modified* J-integral values for various crack depths across the weldment using CT-W, CT-I and CT-B specimen geometries.

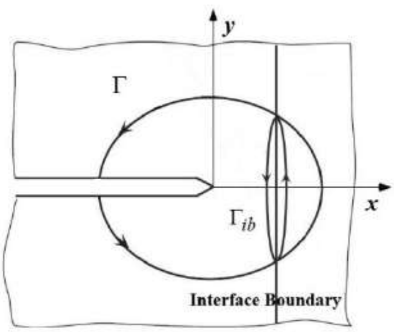

Fig. 5.7 J-Contour for interface boundaries

5.4.2 FEM Simulations

A large number of elastic-plastic 2D FEM simulations have been carried out with and without incorporating HAZ width (0.85 mm) within the weldment. The thickness of the weld across the CT specimen is nearly constant, as seen in photo images shown in Fig. 5.1. Plane strain element (CPE8) with reduced integration has been adopted. Seam crack with 1/√r singularity is assigned to the crack tip. The loading

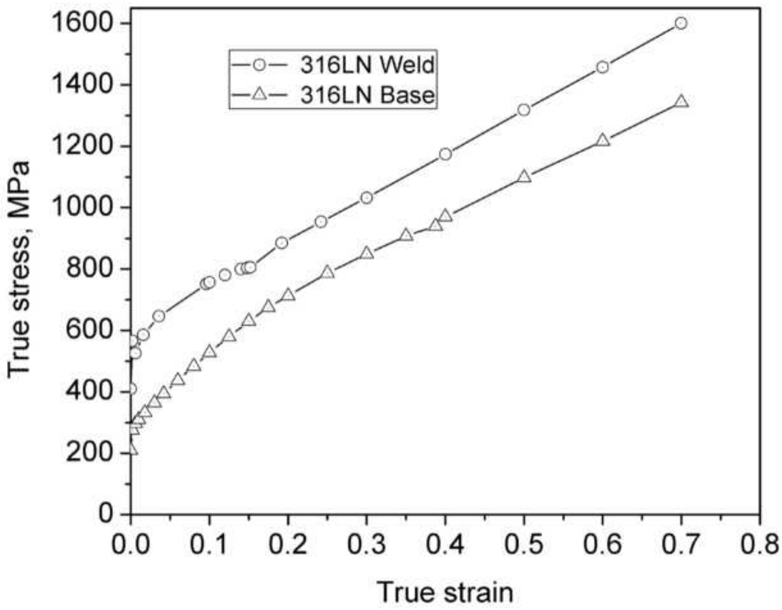

Fig. 5.8 316LN SS base and weld metal stress vs plastic strain data for FEM simulations

pins are modeled as rigid bodies similar to clevis and pin arrangement used in specimen testing. The specimen is loaded by applying displacement to the pins while all other motions of the pins are restrained. Simulations for CT geometry with various stationary crack depths covering the experimental crack extension in CT-W, CT-I and CT-B have been carried out as shown in Table 5.1. The lower and upper bound values of elastic modulus have been used for 316LN SS material. It is considered as 198 GPa and 210 GPa for the softer base and stronger weld metals respectively. The stress vs plastic strain data of 316LN SS base and weld metals used in the material model are shown in Fig. 5.8. For the HAZ region, bilinear stress vs strain data with the elastic constants same as that of weld has been used.

5.4.3 J-integrals with HAZ width as Interlayer

The deformation *J*-integral values for stationary cracks in all three specimens estimated against LLD with and without HAZ are shown in Fig. 5.9. It is observed that incorporating HAZ model in weldment has a negligible effect on *J*-integral values for CT-W and CT-I geometries. However, there is a remarkable decrease in *J*-integral when HAZ model is incorporated while the initial crack tip is in the base material (CT-B). Hence simulations are carried out with HAZ model in weldment for various crack depths, as mentioned in Table 5.1. The scheme of estimating critical LLD to evaluate *J*-integral from FE analysis for specimens with different crack lengths is illustrated in Fig.5.10. The experimental data shows crack length as a function of LLD from a typical experiment with a starting crack length say, a_1. The FEM based J for different non-growing cracks of incrementally increasing lengths, $a_2 \ldots . a_n$ (an interval of 0.5 mm has been chosen) are estimated at critical LLDs that correspond to $a_2 \ldots . a_n$ in the experimental plot. The values of J thus estimated is shown as a function of crack increment in Fig. 5.13 along with the experimental J-Δa curves for CT-I, CT-W and CT-B. The J values have been obtained for all crack depths, as given in Table 5.1.

Table 5.1 Details of crack lengths in FEM simulations for CT-W, CT-I and CT-B specimens.

Specimens	Optically observed experimental crack extension (mm)	FEM simulations for various stationary crack depths (mm)
CT-W	25.85to 29	26.3, 26.8, 27.3, 27.8, and 28.3
CT-I	27.45 to 30.85	27.9, 28.4, 28.9, 29.9 and 30.3
CT-B	29.94 to 33.76	30.3, 30.8, 31.3, 31.8, 32.3, 32.8 and 33.3

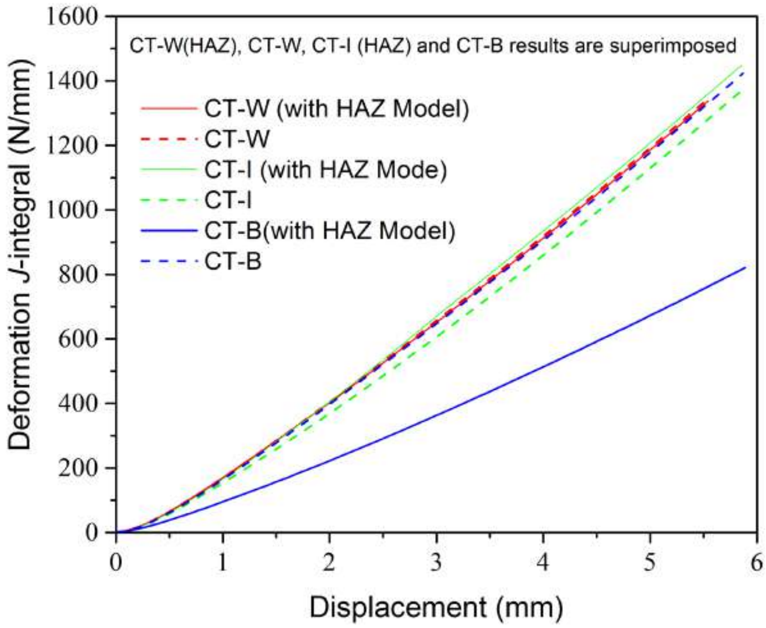

Fig. 5.9 Deformation J-integral vs LLD for crack (a_0) in CT-W, CT-I and CT-B specimens.

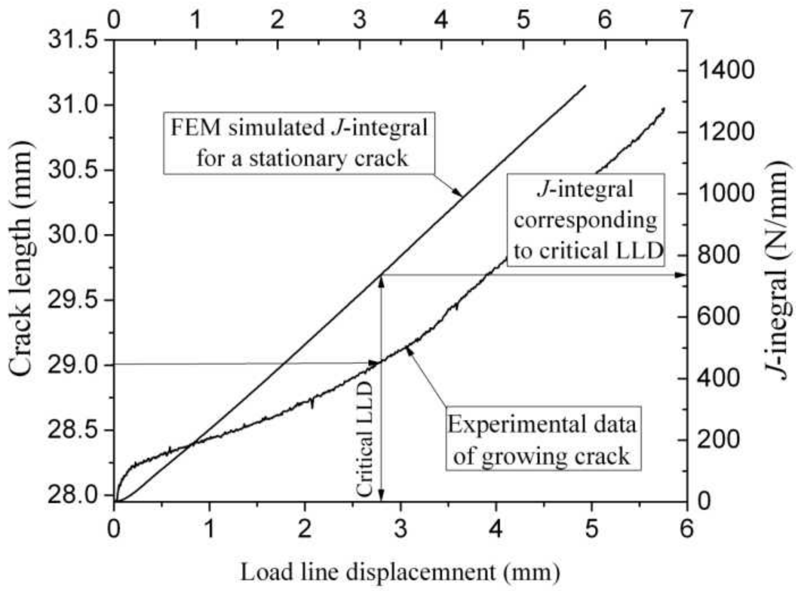

Fig. 5.10 Typical experimental J and crack length vs LLD plot to estimate the critical value of LLD (CT-I)

5.4.4 Evaluation of Modified J-integral

The crack tip *J*-integral and interface *J*-integral for CT-I and CT-B specimens have been evaluated from FEM simulations. Crack tip singularity1/√r is assigned to all nodes along the interfaces. The path independent near-tip *J*-integral (J_{tip}), is obtained for contour Γ_{tip}, which is a few elements away from the crack tip and is crossing the interface, as shown in Fig. 5.11. The von-Mises contour plots with weld and HAZ region (highlighted) is shown in Fig. 5.12 (a, b & c) depicting the extent

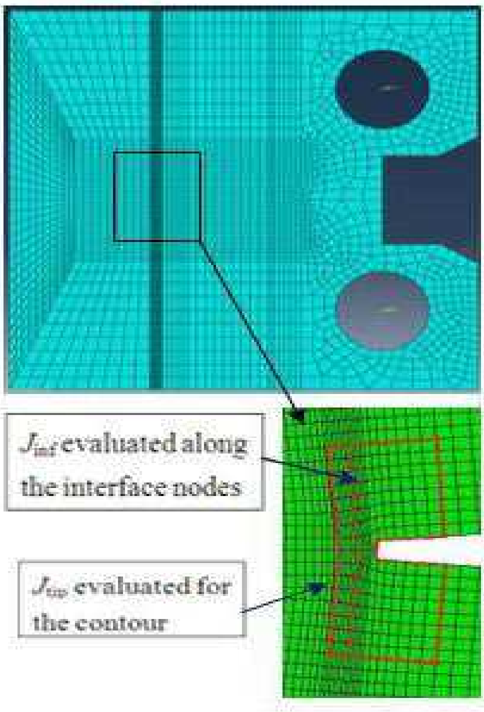

Fig. 5.11 Scheme of extraction of modified J-integrals for CT-I and CT-B specimens

of plasticity along the interface region. Due to interface plastic energy dissipation, crack tip near interface loses proportional loading, and the J-integrals are not path independent [80-82]. The path independent nature of J_{tip} is regained by adding the interface nodal J-integral (J_{inf}) values evaluated along the interface boundary.

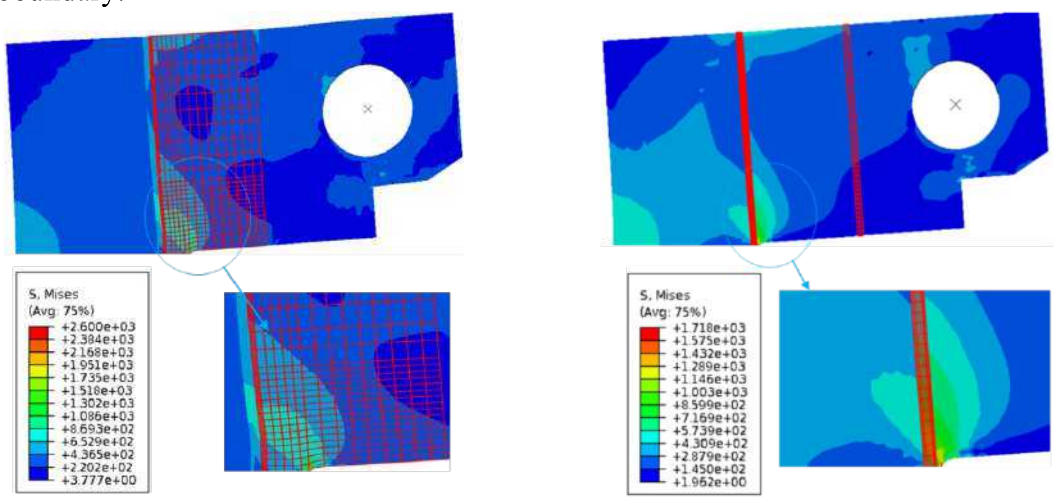

(a) **(b)**

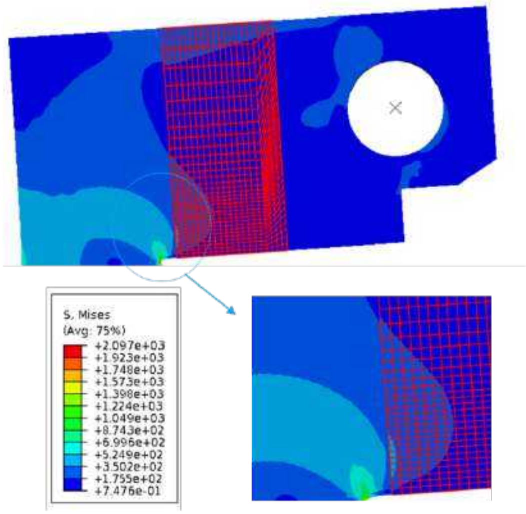

(c)

Fig. 5.12 von-Mises stress contour of the crack tip in (a) CT-W (b) CT-I (c) CT-B

The *J*-integral values corresponding to the critical value of LLD evaluated as per the scheme depicted in Fig. 5.10 for various crack depths are shown in Fig. 5.13 (a, b & c), and the data is presented in Fig. 5.12.

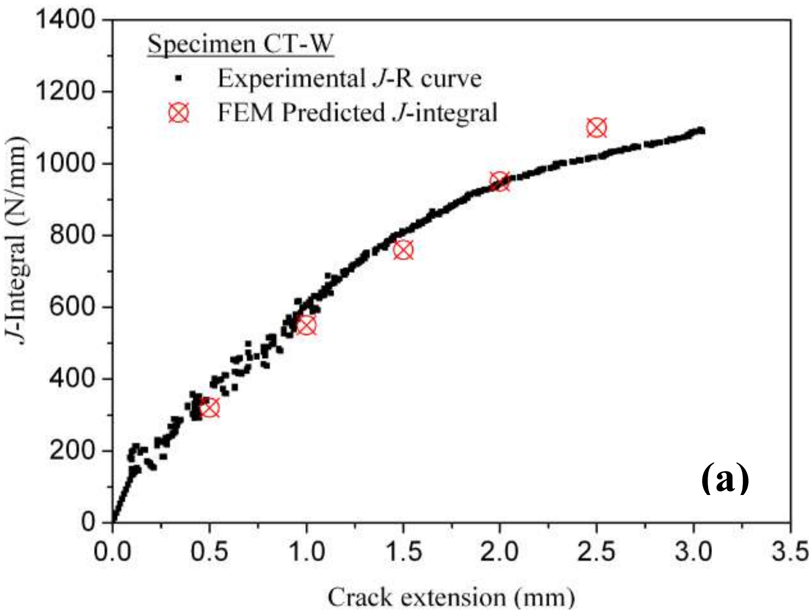

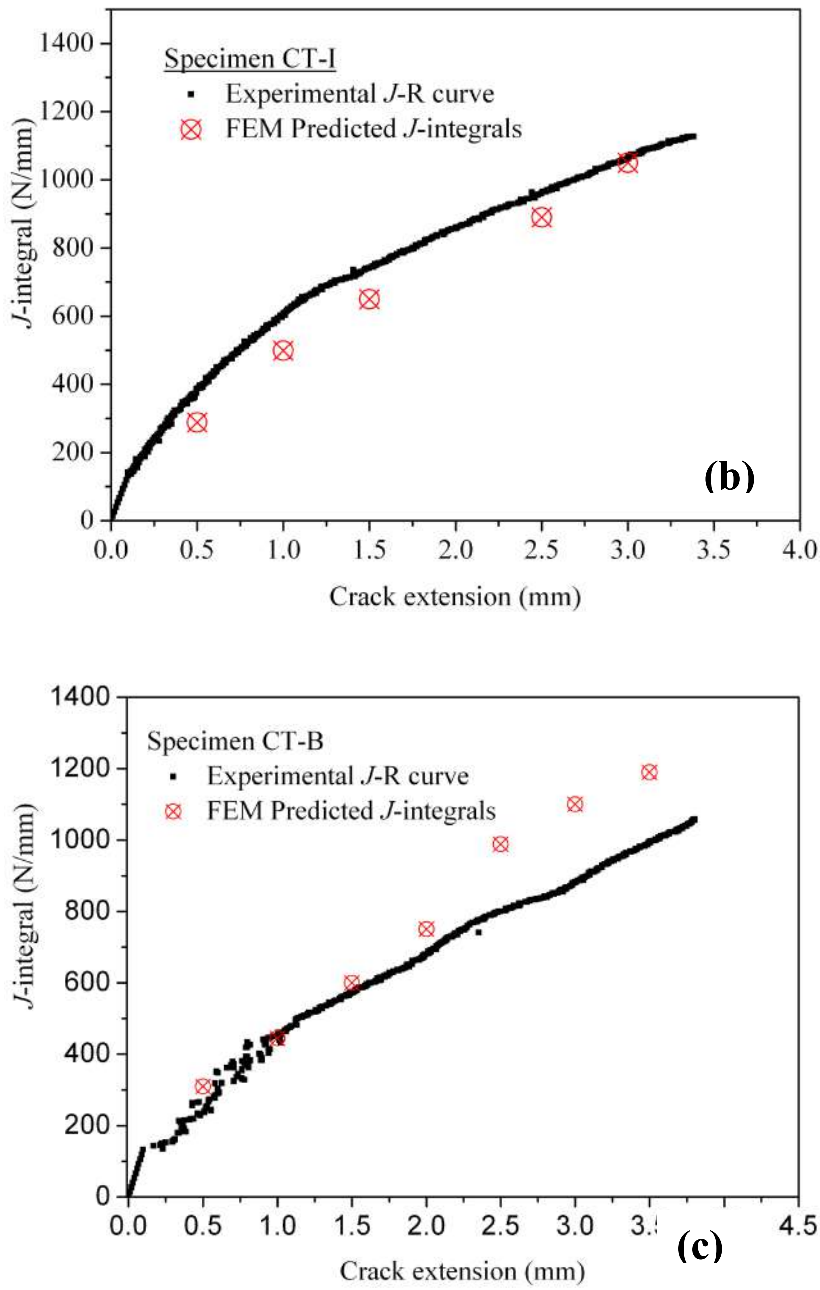

Fig. 5.13 *J*-integral vs crack extension for (a) CT-W specimen (b) CT-I specimen (c) CT-B specimen

5.5 Discussion on Fracture Behaviour of Similar Weld Joint

The FEM predicted *J*-integral values for CT-W, CT-I and up to 2 mm crack growth in CT-B specimens are in close agreement with experimental values (maximum variation is + 8% for CT-W and -17% for CT-I). In the case of CT-B, beyond 2 mm crack growth, the predicted *J*-integrals are much higher than experimental values. The reasons for these variations could be (i) the FEM predictions are based on stationary cracks; (ii) elastic unloading at the crack tip is not accounted in *J*-integral estimation and (iii) in case of CT-B specimen, crack extension beyond 2 mm, *J*-integral value influenced by excessive compressive stress field due to softer base material in the ligament region. The effect of transverse weld/base/HAZ material strength mismatch on crack tip deformation *J*-integral is captured with elastic-plastic FEM analyses. The TR_M across the 316LN SS weldment is illustrated in Fig. 5.14 and Table 5.2. The variation of TR_M across the weldment shows that the crack approaching the HAZ to base material region gets restrained due to inhomogeneity and leading to increased crack resistance. While the crack is in the transition from HAZ to base material region, there is a reduction in crack resistance and beyond this, in the base material; it is a steady state crack growth. A steep gradient in crack resistance is observed due to variation in metallurgical/mechanical properties of various regions like HAZ, fusion zones and weld. The influence of elastic inhomogeneity on a propagating crack in a weldment could be accounted through proposed equivalent Young's modulus approach. The *modified* *J*-integral values obtained from FEM simulation for various stationary crack depths are found to be in good agreement with experimental results. This shows that the proposed equivalent Young's modulus equations along with plastic "η" factor adopted in ASTM E1820 meant for homogeneous materials, are sufficient to account for the inhomogeneity in the material to estimate the *J*-R curve for a transverse weldment. A varying and fluctuating gradient in tearing resistance is found across the 316LN SS weldment. The tearing resistance decreases with crack growth, as seen in the flattening of J-Δa curves. This is because the plastic zone spreads ahead of the crack.

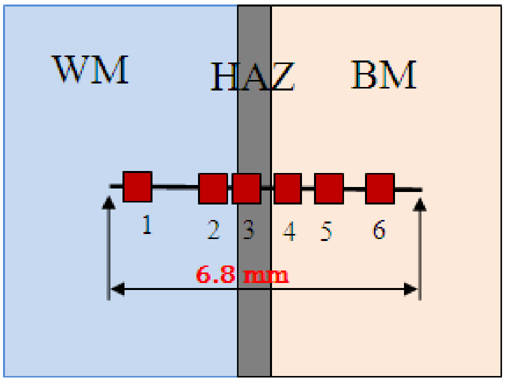

Fig. 5.14 Location of TR_M across the weldment over 6.8 mm crack extension (read in conjunction with Table 5.2)

Table 5.2 Description of crack growth resistance perpendicular to the weldment.

J-R curve (speci-men ID)	crack location in	Crack extension (Δa = 0.5 mm)	Crack approa-ching	Experimental Tearing resistance multiplier (TR_M)	Location in Fig. 5.12	Description of crack extension zone
Fig. 5.6(a) (CT-W)	WM	26.5 to 27	WM	250	1	within WM
	WM	28 to 28.5	HAZ	70	2	WM-HAZ
Fig. 5.6(b) (CT-I)	close to HAZ	28.5 to 29	HAZ	138	3	HAZ-BM
	close to HAZ	30 to 30.5	BM	100	4	HAZ-BM
Fig. 5.6(c) (CT-B)	BM	30.8 to 31.3	BM	125	5	Within BM
	BM	32.8 to 33.3	BM	80	6	Within BM

5.6 Dissimilar Metal Weld joint of P91-316LN SS

5.6.1Mechanical Behavior Characterization of DMW joint

5.6.1 (a) Tensile and Notch Deformation Behavior of Various Regions in Weldment

The engineering stress-strain curves obtained using small tensile specimens (Fig. 2.14(a)) for HAZ, butter and weld regions are shown in Fig. 5.15(a), along with the yield and ultimate strength values. The large difference in ultimate tensile strength of the IN 182 butter and weld could be due to the difference in orientation of dendritic grains with respect to the loading direction. For weld metal specimen, the grains are oriented along weld bead and for butter layer; the grains are oriented across the weld bead. The reduced strength of P91-HAZ is attributed to the migration of carbon into the fusion interface between P91 and the butter layer since the 0.8 mm thick specimen is extracted close to this region [83, 84].

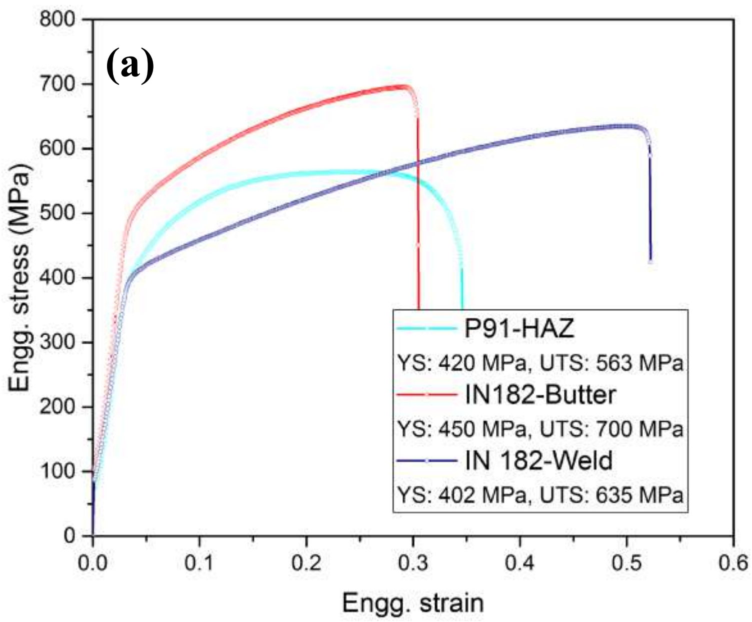

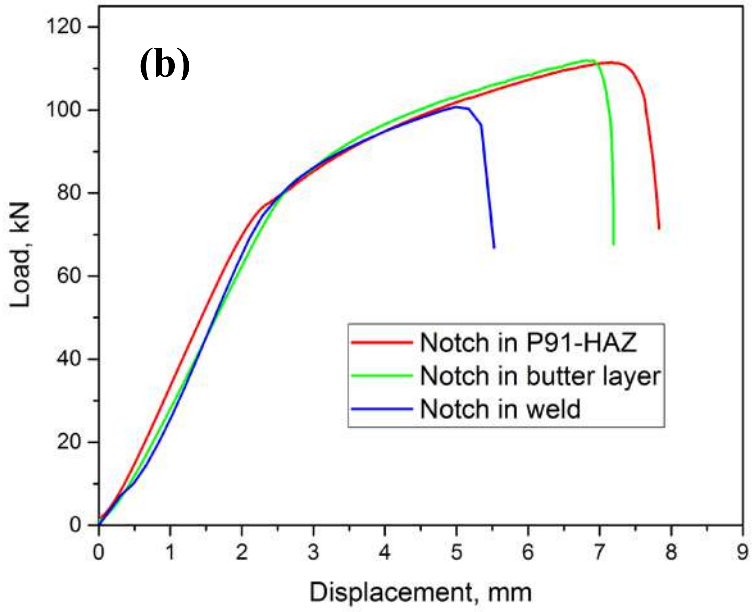

Fig. 5.15 (a) Engineering stress-strain curve of smooth tensile specimens
(b) Load vs Displacement response of notch tensile specimens

Notch strength represents the ability of the material to absorb energy in the presence of a flaw. In general, introducing a notch leads to weakening in strong and brittle materials, and strengthening effect in soft ductile materials [85]. The strengthening occurs due to suppression of shear failure by enhanced stress triaxiality. The notch specimens with notch tip in various regions viz. HAZ, buttering and weld (Fig. 2.14(b)) were tested under quasi-static loading condition at ambient temperature. The load vs displacement responses for these specimens is shown in Fig. 5.15(b). The increase in strength of 6 mm thick notched specimen extracted from low strength P91-HAZ region could be due to large plastic deformation of this soft region. The reduced ductility observed in IN 182 weld region could be due to strain induced during welding. *5.6.1(b) Hardness Profile across Weld J*oint

Figure 5.16 shows the Vicker's micro-hardness variation across DMW joint. The hardness profile was obtained along a line as highlighted. A non-uniform hardness profile was observed across the joint, and a softer zone is identified in

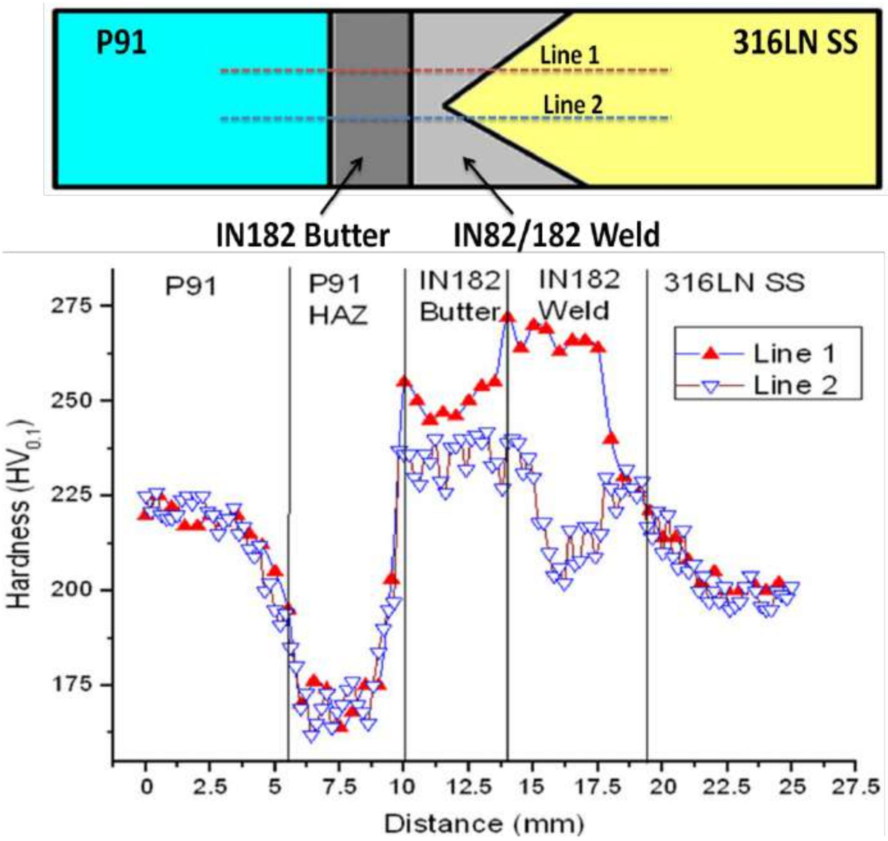

Fig. 5.16 Micro hardness profile across the DMW joint

P91-HAZ. The hardness ranges for the P91 and 316LN SS base metals are 215–230 Hv and 190–230 Hv respectively. The highest hardness of about 260 Hv is found at the interface between P91 and Inconel182 buttering. This could be due to the presence of carbon enriched hard zone formed during carbon migration [83, 84]. The hardness remains nearly the same for both butter and weld regions. The lowest hardness of about 170–180 Hv is observed nearly 4-5 mm from the interface between P91 and IN 182 buttering.

5.6.2 Fracture Behavior Characterization of DMW Joint

Two sets of CT specimens with initial notch in HAZ, butter layer, weld viz. CT-HAZ, CT-BL and CT-DMW and as per the sketch shown in Fig. 2.11 were extracted from weld pad. The side-grooved specimens were tested as per ASTM E1820. The load vs COD plot and *J*-R curves are shown in Fig. 5.17 (a & b). The *J*-R curves for HAZ and butter layers obtained from both sets of specimens (set-1 and set-2) are closely repeatable but for weld, it is not comparable. Further, in spite of side grooves, the fracture morphology of all tested specimens have shown that the crack front has deviated into weld-butter interface layer. This could be due to mutually perpendicular IN 182 dendritic grains undergoing severe plastic deformation and damage in the vicinity of butter weld interface regions.

The notch specimen with 6 mm thick, 60° notch angle and 0.125 mm root radius from various locations of the DMW joint viz., in P91-HAZ, IN 182 butter and IN182 weld imposes a triaxiality state of stress and steep stress gradient. Hence the notch strength evaluated from these specimens could qualitatively represent the relative toughness of all three regions in DMW joint. The notch strength of various regions of DMW joint which fairly represents the initiation toughness of the materials matches with the *J*-R curves. The notch strength is in decreasing order: HAZ, butter layer and weld. The *J*-R curves also follow the same trend, especially in the second set of CT specimens.

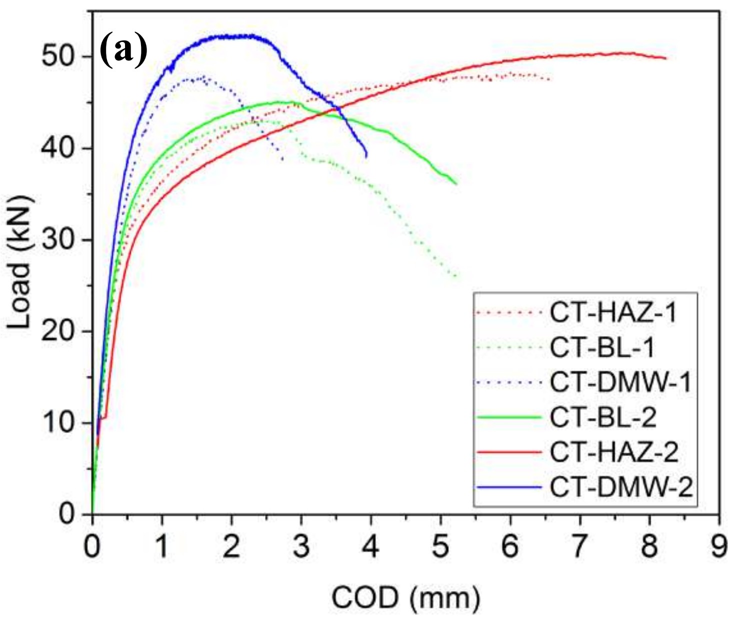

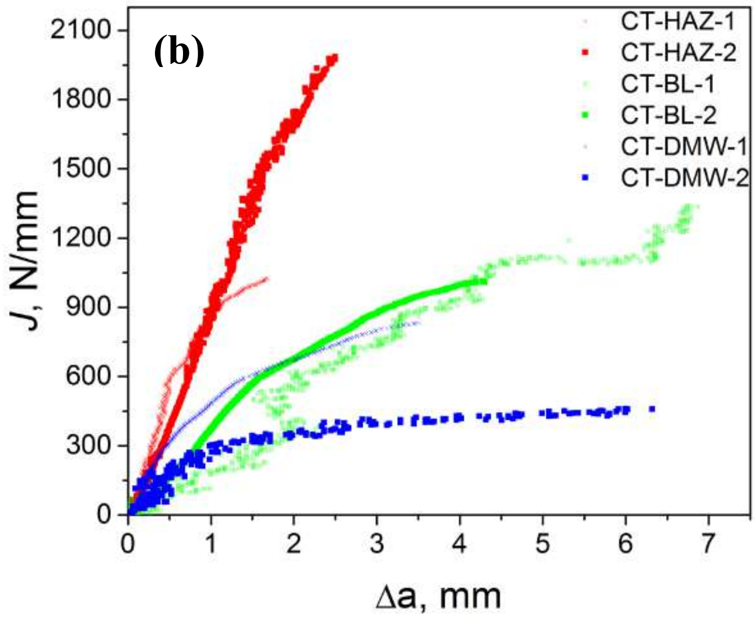

Fig. 5.17 Fracture test results of DMW CT specimens (a) Load vs COD plot (b) *J*-R curve

5.6.3 FEM Simulations

Since the crack plane for all the specimens deviated from the principal plane to the loading direction, FEM simulations have been carried out to verify the applicability

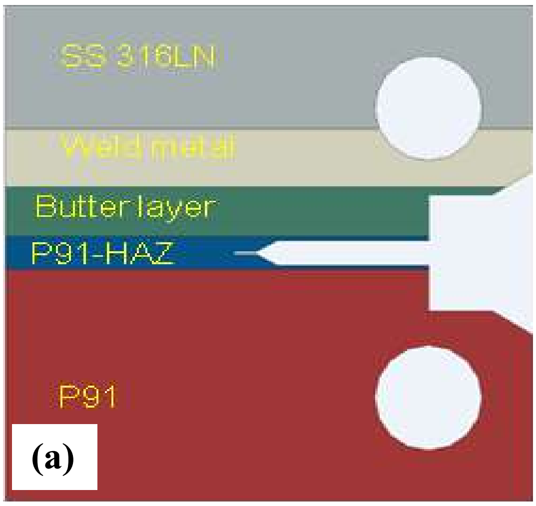

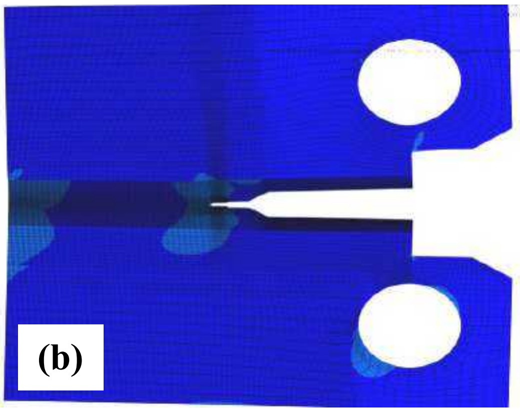

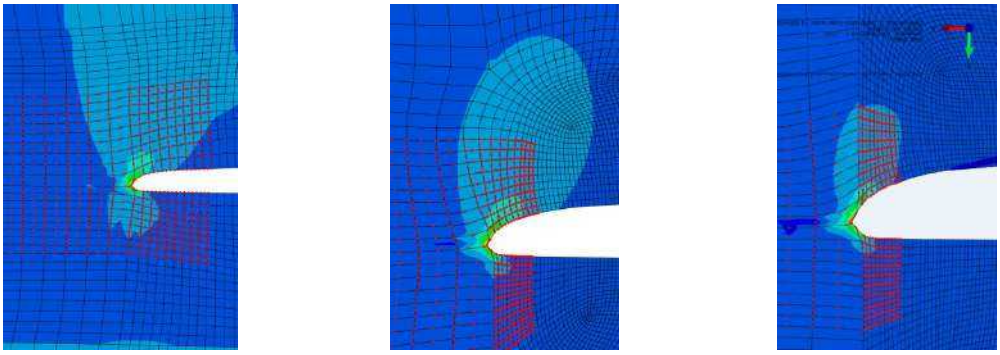

(C) CT-HAZ CT-BL CT-DMW

Fig. 5.18 FE analysis for DMW CT specimen (a) FEM material model (b) FEM mesh model (c) von-Misessress field for P91-HAZ, butter layer and weld for LLD = 2 mm of CT specimen

of ASTM procedure to assess the *J*-R curves for DMW joint CT specimens. Plane 2D model was constructed as per the sketch shown in Fig. 5.18 (a & b) with different material properties for the different regions assigned to each part. The stress-strain data for P91-HAZ, IN 182 butter and weld from small specimen tensile tests were used for elastic-plastic FE analysis. The von-Mises stress field P91-HAZ, butter layer and weld with a stationary crack tip in CT specimen is shown in Fig. 5.20(c). For the same applied 2 mm load line displacement to all the specimens, the crack opening displacement found to be higher for the crack in weld (CT-DMW) than the crack in butter and HAZ. This is due to low yield strength of the weld and the easy spread of plastic zone on one side of the specimen, i.e. towards the weld-butter interface. The preliminary naked eye observation on fracture morphology too agrees with crack front deviating into the weld-butter interface.

5.7 Results and Discussion on Dissimilar Welds

The tensile and notch deformation behavior and *J*-R curves for P91-HAZ, IN182 butter layer and weld have been assessed. The *J*-R curves evaluated as per ASTM E1820 are correlated with von-Mises stress fields of CT specimen with stationary crack. It is observed that the plastic zone spreads towards weld-butter layer interface from the principal plane normal to loading direction due to adjacent material's strength mismatch and interfaces. Adopting the ASTM expressions for *J*-R curve determination does not truly represent the fracture behavior of each zones of DMW joint. It is proposed to adopt the *modified* *J*-integral approach established in the earlier part of this chapter to evaluate numerical elastic-plastic *J*-integral. Further, a detailed analysis of fracture morphology and correlation with inverse polar figures will help to assess the fracture behavior of each zone in the DMW joint more precisely.

5.8 Conclusion

The following important conclusions have been drawn based on experimental and numerical analysis of similar (316LN SS) and dissimilar (316LN SS-P91) welds:

(1) The influence of elastic inhomogeneity on a propagating crack in a weldment (strength mismatch zones) has been accounted through proposed equivalent Young's modulus approach for CT specimen.

(2) The experimental *J*-R curves estimated based on equivalent Young's modulus modification in elastic *J*-integral and as per the ASTM E1820 procedure are in

agreement with the *modified* J-integral values obtained from numerical simulations for 316LN SS.

(3) The fracture morphology of tested DMW CT specimen and von-Mises stress fields from FE analysis on CT specimen with stationary crack has shown that the crack front deviates from the principal crack plane. This is due to adjacent material strength mismatch and interfaces.

Chapter 6: Verification of Proposed Methodology for Fracture Prediction in 316LN SS Pipes

6.1 Introduction

In this chapter, an attempt has been made to demonstrate the ability of the coupled experimental-numerical procedure validated at specimen level (CT) to predict fracture behavior of 316LN SS straight pipe. In spite of having well-established procedures [32] for assessment of fracture behavior from laboratory scale specimens like CT and three point bend specimens, the applicability of these data for integrity assessment of piping components still remains a challenge due to limited crack growth data. This has been addressed by many researchers for the piping components [85-89]. Experimental methods to evaluate the *J*-R curve for straight pipes have been established by Zahoor and Kanninen [85]. For 316L pipes, the fracture resistance has been evaluated by Forster et al. [86], the differences between *J*-R curves obtained from pipes and CT specimens have been reported. Similar observations were also made for circumferentially through-wall cracked pipes by Moulin and Delliou [87] for 316L and Chattopadhyay et al. [88] for SA333 Gr.6 carbon steel. This observation also holds good for 304LN SS, and it is related to the differences in crack tip constraints for the CT and piping components as reported by Singh et al. [89]. The influence of crack tip constraint on material fracture toughness at specimen level has been discussed by Tarafder et al. [90], and the comparison of fracture toughness from laboratory specimens with the fracture resistance of components for SA 333 Grade 6 carbon steel has been discussed by Pavankumar et al. [91]. The present study is on 316LN SS pipes and pipe welds, which is essential for integrity assessment of PFBR piping components. Further, the fracture transferability problem is prominent due to the following reasons:

(1) most of the piping components used in sodium cooled fast breeder reactor are thinner than the minimum thickness required to evaluate the fracture resistance from standard specimens,

(2) limited crack extension data (1.5-3 mm) is available from fracture tests on laboratory specimens, whereas the crack growth analysis requires large extensions (40-50 mm) for components and

(3) scatter in fracture test data of welded specimens.

Hence, to ensure the integrity of 316LN SS piping and fracture transferability, detailed experimental-numerical fracture analyses of various components, e.g. straight pipes, elbows and branch tees are required along with data from conventional laboratory specimens. Towards this, experimental and numerical studies have been conducted to establish the fracture parameters that are transferable from specimens to components. Experiments were carried out to investigate the fracture behavior of through-wall cracked 316LN SS base and welded straight pipes. The *J*-R curves evaluated from pipes have been compared with those from laboratory CT specimens. Further, the FEM predictions for crack growth in the pipe are compared with experimental results.

6.2 Fracture test on pipes

The fracture tests are carried out under displacement control and the details have been discussed in section 2.5. Typical load vs displacement and load vs crack growth data for base and weld specimens with nominal circumferential crack angle (2θ) are shown in Fig. 6.1(a-d) and 6.2(a-d). From the recorded images and the grids marked along the crack growth direction, the crack extension has been estimated with the accuracy of measurement is ±0.05 mm. The periodic unloading is carried out to estimate the compliance at various crack depths. The incremental area estimate is used to calculate the plastic area required for evaluating the *J*-R curve.

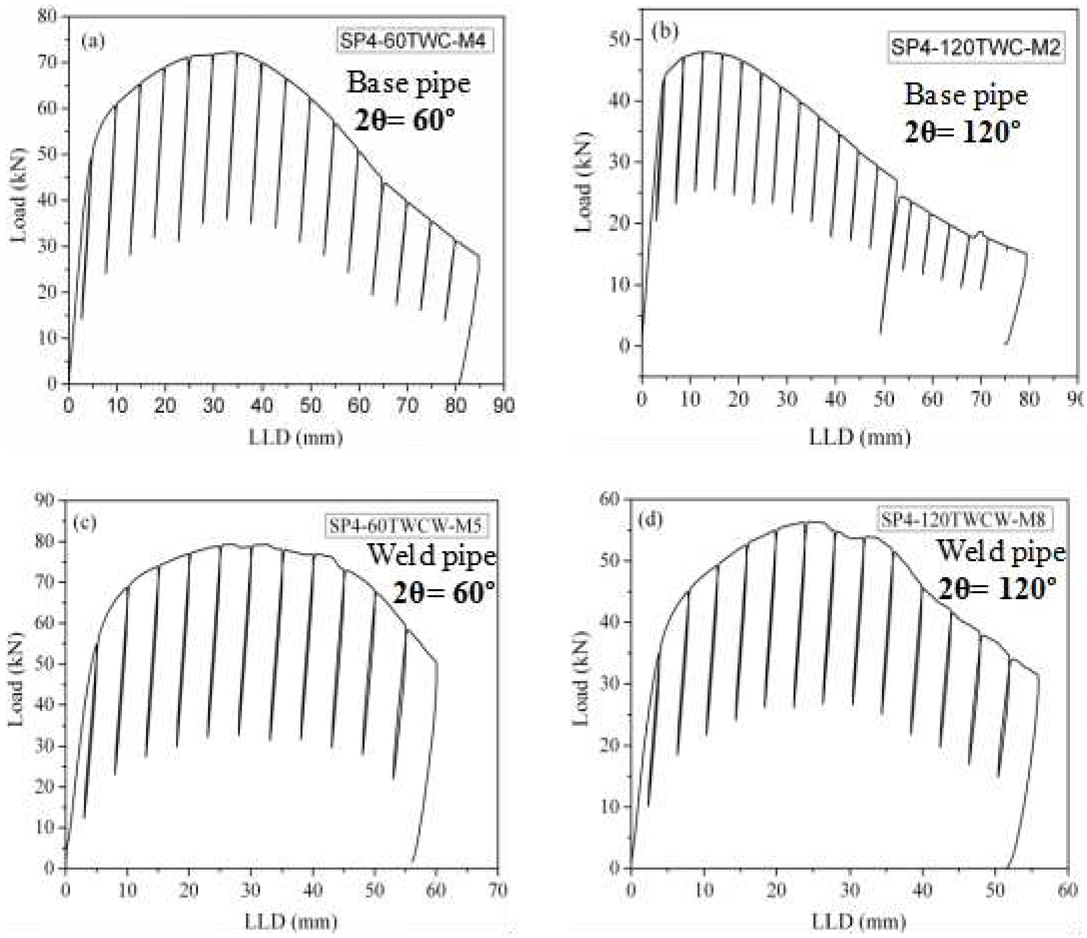

Fig. 6.1 Load vs displacement record of base pipe: **(a)** for crack angle 2θ= 60°, and **(b)** for crack angle 2θ= 120° and Load vs displacement record of weld pipe: **(c)** for crack angle 2θ= 60°, **(d)** for crack angle 2θ= 120°

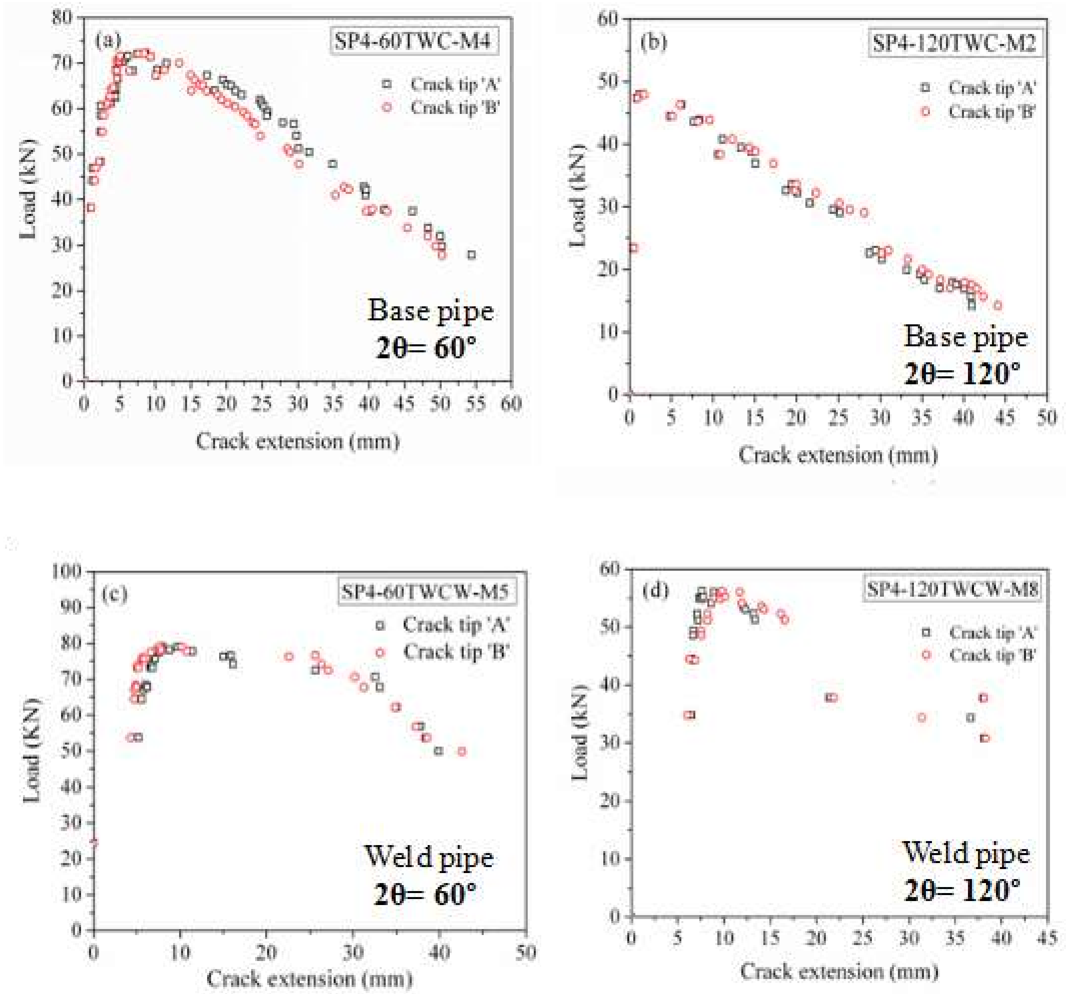

Fig. 6.2 Load vs crack extension record of base pipe: **(a)** for crack angle 2θ= 60°, and **(b)** for crack angle 2θ= 120° and Load vs displacement record of weld pipe: **(c)** for crack angle 2θ= 60°, **(d)** for crack angle 2θ= 120°

Fig. 6.3 Photograph of crack growth of crack tip-A of fracture experiment on Specimen number (a) SP4-60TWC-M4, (b) SP4-120TWC-M2 (c) SP4-60TWCW-M5 and (d) SP4-120TWCW-M8

6.3 Determination of Fracture Resistance Curve and Tearing Modulus

The load-displacement and load-crack extension data are used to generate *J*-R curve for pipe based on the method proposed by Zahoor and Kanninen [85]. The *J*-integral for through-wall cracked pipe under four-point bending is given by the following expressions.

$$J = J_{\mathrm{el}} + J_{\mathrm{pl}} \tag{6.1}$$

The elastic solution for through-wall cracked pipe subjected to four-point bending is given by Zahoor and Kanninen [85] as follows:

$$J_{\mathrm{el}} = K^2 / E' \tag{6.2}$$

$$K = \sigma.(F_G)\sqrt{(\pi a)}, \tag{6.3}$$

where

$(F_G)^2 = (0.7631 - 1.7602x + 1.3511x^2 - 0.3822x^3)/(1-x)^3$,

x - is the ratio of cracked area to the cross-sectional area of the pipe, a is half of the circumferential crack length, and σ is the tensile bending stress in the outer fibre

$$J_{\text{pl}} = \beta \int_0^{\delta} P d\delta + 2 \int_{\theta_0}^{\theta} \gamma . J_{\text{pl}} \, \mathrm{d}\theta, \tag{6.4}$$

where δ varies from 0 to final δ and θ varies from θ_0 to final θ, $2P$= total bending load, δ - load line displacement, 2θ - total crack angle

$$\beta = -h^{'}(2\theta)/\,\mathrm{Rt}\, h(2\theta), \tag{6.5}$$

$$\gamma = h^{''}(2\theta)/h^{'}(2\theta), \tag{6.6}$$

$$h(2\theta) = [\cos(\theta/2) - \tfrac{1}{2}\sin(\theta)], \tag{6.7}$$

$$h^{'}(2\theta) = \mathrm{d}h(2\theta)/2\mathrm{d}\theta \tag{6.8}$$

where R is radius and t thickness of the pipe. The second term in Eq. (6.4) represents the correction due to crack growth. This term vanishes when the plastic J is computed at the point of crack initiation. For stable crack growth, the first term in Eq. (6.4) is calculated using the area under the load versus LLD record to obtain an approximate value of J_{pl}.

6.4 X-FEM Simulation of Crack Growth

Crack growth simulations have been carried out using X-FEM on through wall cracked pipes (OD 88.9 and 5.49 mm thickness) subjected to four-point bending. The crack initiation and evolution parameters are essential inputs to the material model to carry out the X-FEM simulations of crack growth. In the present study, maximum principal stress-based crack initiation and energy-based growth criteria have been adopted. Based on coupled experimental – finite element analyses, crack initiation stress and crack evolution energy for 316LN SS has been established as 1500 MPa and 760 N/mm respectively for plane strain condition (discussed in Chapter-3). However, the crack tip constraint level for pipe under study is much lower than plane strain condition. Hence, the instability strain (uniform strain) over a characteristic distance (2 grain diameter) is a critical condition for crack initiation in 316LN SS material under multiaxial stress-state. Hence the true stress (800 MPa) corresponding to uniform strain in the uniaxial tensile test has been considered appropriate. The half-symmetrical pipe model with through-wall crack sizes, 2θ° = 67 and 97° has been prepared. The specimen has been modelled using C3D8R type hexahedral elements. The details of boundary conditions, mesh model and crack extension are shown in Fig. 6.4. Boundary conditions corresponding to hinge and roller supports are applied to the surface nodes. Symmetric boundary condition is imposed on the pipe surface to arrest translation and rotation of the nodes. Displacement is applied to the analytically rigid loading fixtures at a reference point. Maximum principal stress (σ_{max} = 800 MPa) and crack evolution energy (760 N/mm) have been used as the crack initiation and growth criteria.

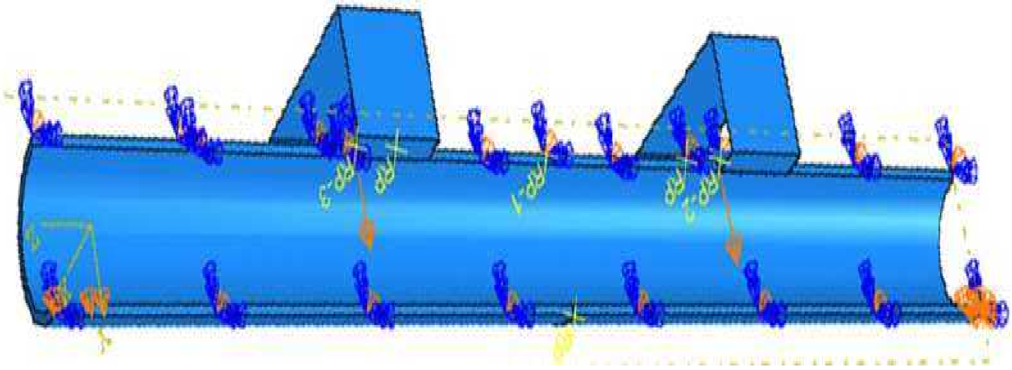

Fig. 6.4(a) Boundary conditions applied to the model

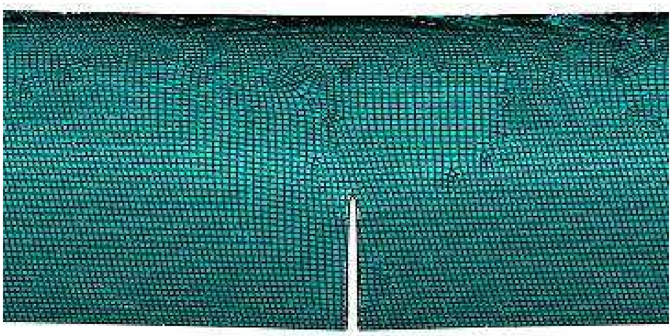

Fig. 6.4(b) Typical mesh adopted for simulation

6.5 Results and Discussion

6.5.1 J-R curves

The *J*-R curves obtained from CT specimen and pipe tests are shown in Fig. 6.5. Exponential function as given below, is found to give the best of *J*-R curves data for both the pipes and CT specimens.

$$J = \alpha(1 - e^{-\beta \Delta a})^{\gamma} \tag{6.9}$$

where α, β, γ are the fitting constants and Δa is the crack extension in mm.

The tearing modulus is evaluated as per the procedure proposed by Paris et al. [92].

$$T = \frac{E}{\sigma_f^{\,2}} \frac{dJ}{da} \tag{6.10}$$

In the above equation, E is Young's modulus in N/mm^2, σ_f is the flow stress in N/mm^2, J is the J-resistance in kJ/mm^2, da is the change in crack extension $d(\Delta a)$ in mm.

The J-R curves for CT specimens are obtained for crack extensions of Δa = 3.927 mm and 4.547 mm for base and weld specimens respectively which are small compared to the crack growth in the case of base and weld pipes. The CT specimen J-R curves have been extrapolated for effective comparison with the component J-R curves. Beyond the maximum J- value from the experiment, the J-R curve has been analytically extrapolated in a tangentially linear manner up to a J- value equal to twice the measured maximum J- value on J- vs tearing modulus plane [93]. For base-CT specimen, the equations for the extended J-T curve and corresponding J-R curve are:

$$J = 2343.77 - 3.06T \tag{6.11}$$

$$J = 2343.77 - 601.75 * e^{\left(\frac{3.93 - \Delta a}{3.65}\right)} \tag{6.12}$$

For weld-CT specimen, the equations are:

$$J = 1294.87 - 3.2T \tag{6.13}$$

$$J = 1294.87 - 129.78 * e^{\left(\frac{4.55 - \Delta a}{3.81}\right)} \tag{6.14}$$

The fitting constants for pipe and CT specimens are given in Table 6.1.

Table 6.1 Values of fitting constants

Specimen ID	α	β	γ
SP4-90TWC-M1	4041	0.015	0.265
SP4-120-TWC-M2	2708	0.043	0.454
SP4-150TWC-M3	2603	0.031	0.317
SP4-60-TWC-M4	3709	0.066	0.469
SP4-60TWCW-M5	10213	0.005	0.398
SP4-90TWCW-M6	6672	0.018	0.476
SP4-120TWCW-M8	3891	0.086	0.633
CT specimen (Base)	2411	0.228	0.692
CT specimen (Weld)	1299	0.437	0.738

Figures 6.5(a-b) and 6.6(a-b) shows the *J*-R, and *J*-T curves for the base, and weld specimens with through wall circumferential crack of various sizes. Due to insufficient synchronized crack length data for weld pipe of 150° crack angle, it has not been analyzed. With an increase in initial crack size, the pipe *J*-R curve is found to shift downwards. The fracture resistance of the pipes is found to be decreasing with the increase in initial crack size (angle). The effect of initial crack angle on the *J*-R curve in the case of weld pipe is negligible, especially in the initial regime of crack growth (up to 15 mm). In the weld pipes, the crack has deviated into interface/base material region which could be due to extensive plastic deformation in the interface region caused by strength mismatch.

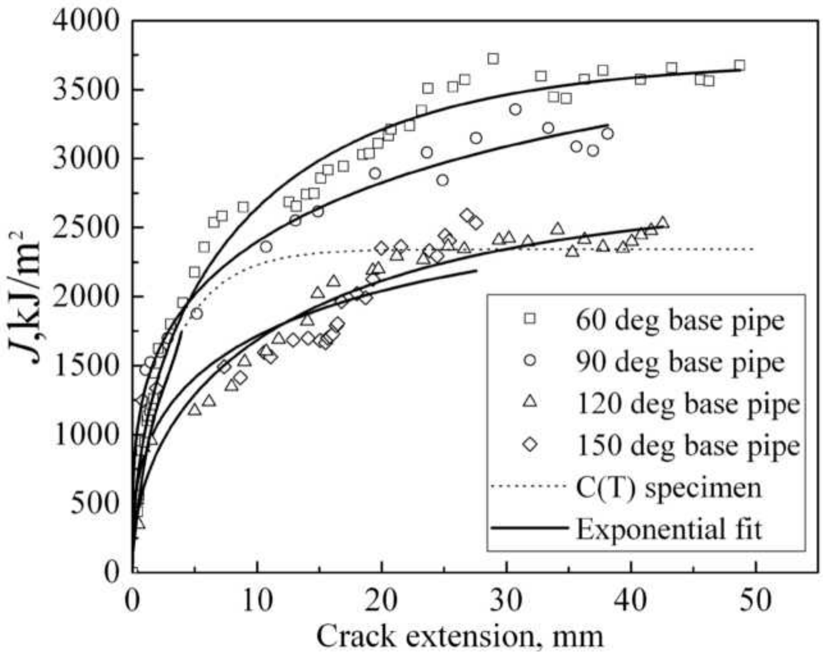

(a)

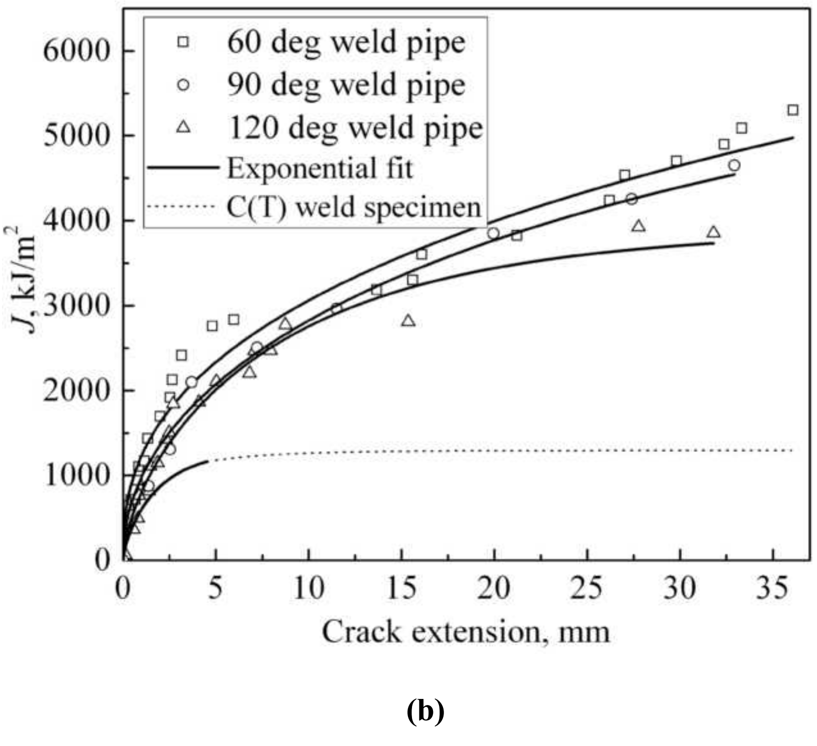

(b)

Fig. 6.5 *J*-R curves (a) base pipes (b) weld pipes

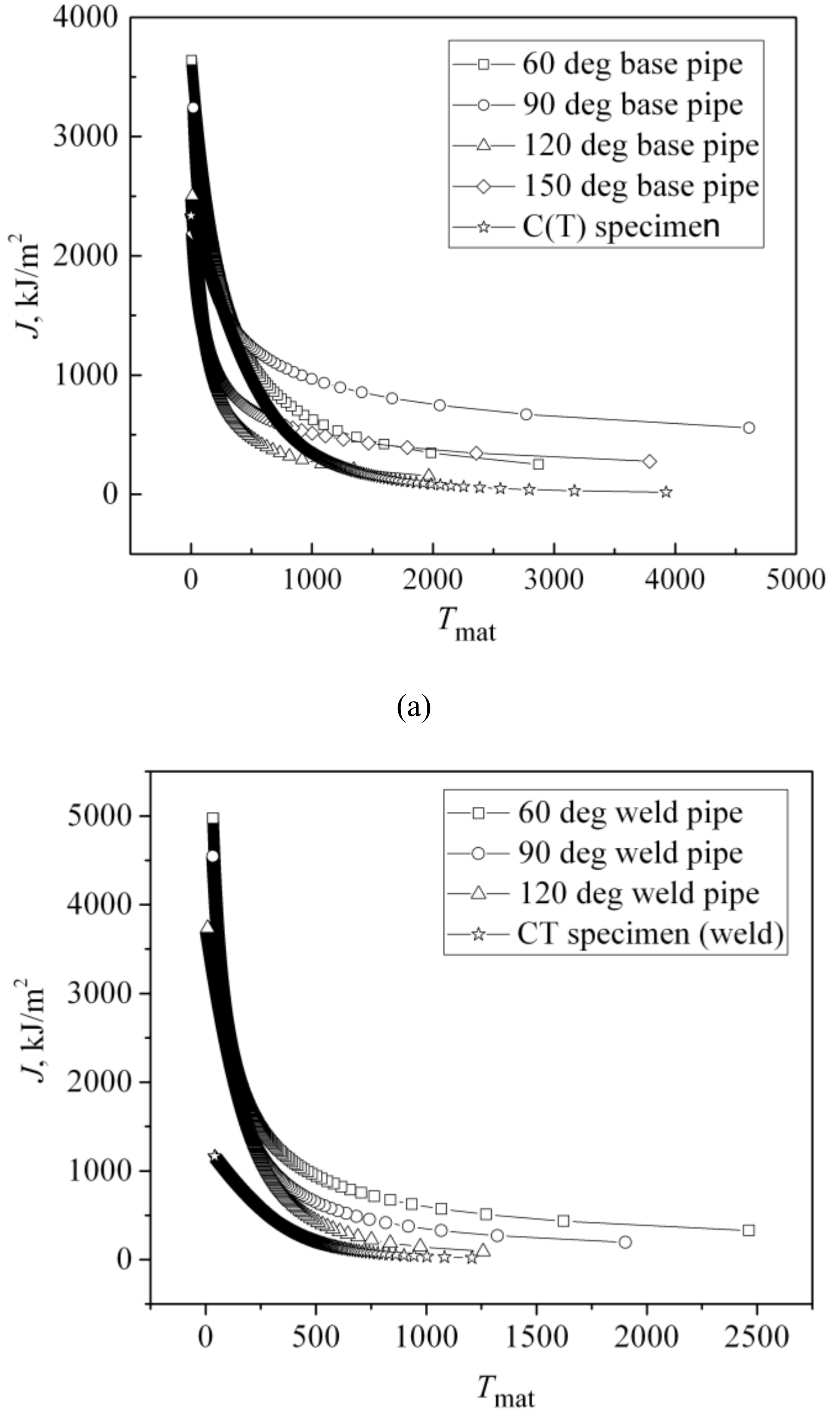

(a)

(b)

Fig. 6.6 *J*-T curves (a) base pipes (b) weld pipes

6.5.2 Limit Load analysis

The experimental maximum moment of the pipe is compared with the analytical estimate. This will help to identify the dominant failure mode, i.e., plastic collapse or ductile tearing. The plastic collapse moment (M_L) is calculated as follows [85]:

$$M_L = 4R_m^2 t\sigma_f[\cos(\theta/2) - 0.5\sin(\theta)] \quad 6.15)$$

where, R_m is the mean radius of the pipe cross-section, t, wall thickness, σ_f is flow stress $\sigma_f = (\sigma_y + \sigma_u)/2$ and θ, the semi-crack angle.

Moulin and Delliou [87] modified the equation (6.15) to account for the crack propagation at the maximum moment and proposed the following modified equation.

$$M_c = 0.854 \times R_m^2 t\sigma_f[\cos(\theta/2) - 0.5\ \sin(\theta)] \quad (6.16)$$

The above equation is obtained by modifying the flow stress term to $\sigma_f = (\sigma_y + \sigma_u)/2.4$ instead of $\sigma_f = (\sigma_y + \sigma_u)/2$ in eq. (6.15) and is empirically found to be valid for pipes with a crack angle greater than 30°; below which the pipes undergo ovalization and fail by buckling. Equations 6.15 and 6.16 are adopted to estimate the M_c values for 88.9 mm OD pipes used in the present study. The estimated values and percentage difference with respect to experiment [($M_{c,experiment}$ -$M_{c,estimated}$) X 100/$M_{c,experiment}$ values] are shown in Table 6.2. The positive difference indicates that the analytical estimate for small diameter pipe is conservative. The equation 6.15 is able to provide close and conservative prediction for base pipes, reasonable and non-conservative prediction for weld pipes. Eqn. 6.16 is able to provide a conservative prediction for base and weld pipes. The limit load estimation is found to be much higher than the maximum load obtained from experiments. These values are also included in Table 6.2 to show that the failure load (limit load) estimation based on analytical expression overestimates the actual structural bearing strength, i.e., maximum experimental load and the crack initiation precedes the analytical limit load.

6.5.3 X-FEM Predictions

In order to assess the suitability of the method and the crack initiation and growth criteria adopted in the present study, the load-displacement response for the pipe of 60 and 90° crack angle is obtained from X-FEM simulations and compared with those from experiments. The X-FEM predicted load vs displacements are in close agreement with experimental results for 60 and 90° crack angles, as shown in Fig. 6.7. The stress triaxiality ahead of growing crack in 60 and 90° crack angle pipes is varied between 0.27-0.6 (shown in Fig. 6.8) which is lower than the crack growing in CT specimen (average φ is 1.6 as shown in Fig. 3.4). Therefore, the maximum principal stress and crack evolution energy parameters, i.e., 800 MPa based on uniform strain and 760 N/mm are found suitable for crack growth simulations of 316LN SS components under low stress triaxiality. Crack growth simulations using maximum principal stress and evolution energy parameters as obtained from specimen level analysis is able to provide fracture prediction for components under low stress triaxiality situations.

Table 6.2 Experimental and Analytical Limit Moments

Specimen ID	Crack Location	Expt. (M_{max}) expt./ $4R_m^2 t\sigma_f$	Predicted moment using Eqn.(6.15) / $4R_m^2 t\sigma_f$, where $\sigma_f = \frac{\sigma_y + \sigma_u}{2}$ (% diff.)	Eqn. (6.16)/ $4R_m^2 t\sigma_f$, where $\sigma_f = \frac{\sigma_y + \sigma_u}{2.4}$ (% diff.)	Expt. Crack initiation load (kN)	Expt. Max. load (kN)	Anal. limit load (kN)
SP4-90TWC-M1	Base	0.594	0.537 (+9.67)	0.46 (+23.22)	61.8	62.05	80.61
SP4-120TWC-M2	Base	0.460	0.411 (+10.63)	0.35 (+24.03)	45	48.00	73.44
SP4-150TWC-M3	Base	0.310	0.277 (+10.71)	0.24 (+24.10)	52	32.38	64.79
SP4-60TWC-M4	Base	0.692	0.672 (+2.93)	0.57 (+17.49)	68.4	72.25	87.72
SP4-60TWCW-M5	Weld	0.574	0.633 (-10.29)	0.54 (+6.25)	53.7	79.26	123.7
SP4-90TWCW-M6	Weld	0.423	0.486 (-15.03)	0.41 (+2.23)	41	58.35	112.3
SP4-150TWCW-M7	Weld	0.253	0.27 (-6.61)	0.23 (+9.38)	26	34.98	92.79
SP4-120TWCW-M8	Weld	0.408	0.407 (+0.29)	0.35 (+15.24)	43	56.37	105.6

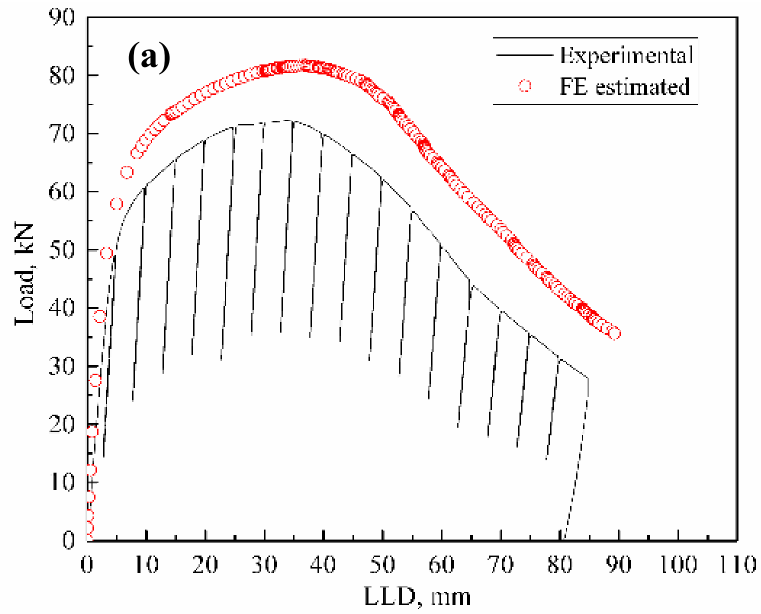

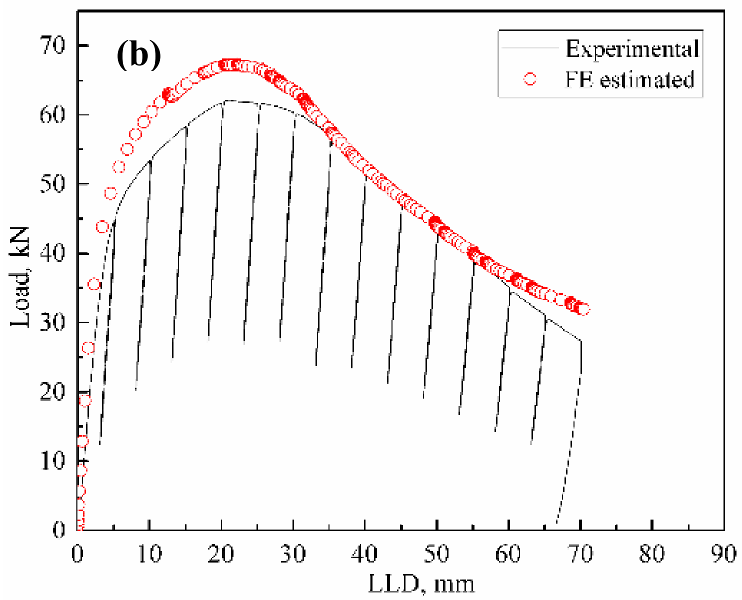

Fig. 6.7 X-FEM predicted load vs displacement curve for (a) 60° crack angle and (b) 90° crack angle

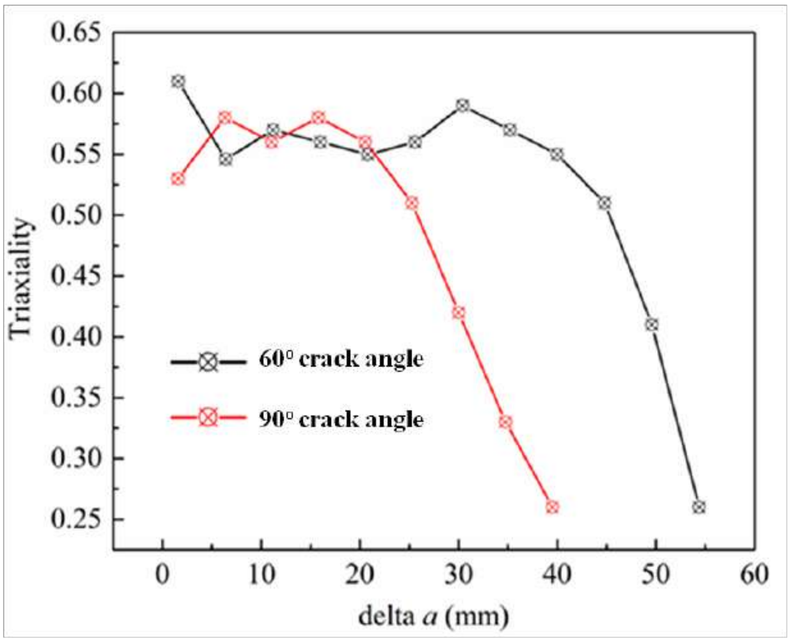

Fig. 6.8 Stress triaxiality ahead growing crack in 60 and 90° crack angle pipes

6.6 Summary

Fracture experiments on 316LN SS base and weld pipes have been conducted to generate *J*-R curves, and this has been compared with specimen level *J*-R curves. There is a significant difference in *J*-R curves obtained from pipe and CT specimen. Hence, the specimen level data is not suitable for fracture assessment of 316LN SS components due to various reasons, as discussed earlier in this chapter and previous chapters. As an attempt to validate the fracture criteria and material specific fracture parameters established at specimen level, crack growth predictions for 316LN SS base pipes have been carried out using X-FEM. The predictions are found to be closely agreed with experimental data.

6.7 Conclusion

The following important conclusions may be drawn based on experimental and numerical fracture analysis on pipes and CT specimens.

1) The experimental *J*-R curve for 316LN SS base and weld pipes with through-wall crack has been established. The comparison of *J*-R curves between pipe and pipe welds with CT specimens indicate that the CT specimen data is not suitable for fracture assessment of components.
2) The predictive ability of fracture parameters validated at specimen level (CT) has been demonstrated for crack growth prediction in 316LN SS straight pipes.
3) The limit load analyses reveal that the crack initiation and propagation are observed prior to attaining the maximum bending moment.

Name: S Athimoolakrishnan, Enrolment Number: ENGG02201504008

Thesis Title: Investigation on Ductile Fracture of Structural Steels and Welds: Numerical Analysis and Experimental Assessment

Thesis Highlights

- The work towards prediction of fracture in 316LN SS and P91 base materials, 316LN SS weld and dissimilar metal weld joint between 316LN SS and P91 using combination of experimental data, numerical methods and analytical procedure have been investigated.
- The experimentally validated material fracture parameters and FEM predictive procedures developed in the present investigation have been demonstrated for fracture predictions under intermediate stress triaxiality in P91 steel and in small diameter 316LN SS straight pipes.
- The proposed local damage approach based on uniform strain and grain diameter is able to predict the crack initiation parameters viz., SZW_i, J_i and $CTOD_i$ under monotonic loading condition.
- The damage parameter and saturated *far field* J-integral for a growing crack have been evaluated and calibrated with experimental results.
- The Rice-Tracy damage parameter evaluated from coupled experimental-numerical analysis for crack initiation in P91 steel was able to predict the crack initiation load for a range of stress triaxiality conditions.
- A modified elastic component, J_{el} based on instantaneous equivalent Young's modulus has been introduced to evaluate J-R curve across the 316LN SS weldment.
- The experimental J-R curves estimated as per the ASTM E1820 procedure are in agreement with the proposed *modified* J-integral values obtained from numerical simulations.
- The experimental J-R curve for 316LN SS base and weld pipes with through-wall crack have been established.
- The comparison of J-R curves between pipe and pipe welds with CT specimens indicate that the CT specimen data is insufficient for fracture assessment of the components.
- The X-FEM crack growth simulations results are in close agreement with experimental result of base pipes.

Name: S Athimoolakrishnan, Enrolment Number: ENGG02201504008

Thesis Title: Investigation on Ductile Fracture of Structural Steels and Welds: Numerical Analysis and Experimental Assessment

Thesis Highlights

- The work towards prediction of fracture in 316LN SS and P91 base materials, 316LN SS weld and dissimilar metal weld joint between 316LN SS and P91 using combination of experimental data, numerical methods and analytical procedure have been investigated.
- The experimentally validated material fracture parameters and FEM predictive procedures developed in the present investigation have been demonstrated for fracture predictions under intermediate stress triaxiality in P91 steel and in small diameter 316LN SS straight pipes.
- The proposed local damage approach based on uniform strain and grain diameter is able to predict the crack initiation parameters viz., SZW_i, J_i and $CTOD_i$ under monotonic loading condition.
- The damage parameter and saturated *far field* *J*-integral for a growing crack have been evaluated and calibrated with experimental results.
- The Rice-Tracy damage parameter evaluated from coupled experimental-numerical analysis for crack initiation in P91 steel was able to predict the crack initiation load for a range of stress triaxiality conditions.
- A modified elastic component, J_{el} based on instantaneous equivalent Young's modulus has been introduced to evaluate *J*-R curve across the 316LN SS weldment.
- The experimental *J*-R curves estimated as per the ASTM E1820 procedure are in agreement with the proposed *modified* *J*-integral values obtained from numerical simulations.
- The experimental *J*-R curve for 316LN SS base and weld pipes with through-wall crack have been established.
- The comparison of *J*-R curves between pipe and pipe welds with CT specimens indicate that the CT specimen data is insufficient for fracture assessment of the components.
- The X-FEM crack growth simulations results are in close agreement with experimental result of base pipes.